Experimental study and numerical simulations of the spectral properties of XUV lasers pumped by collisional excitation

Limin Meng

UNIVERSITÉ PARIS-SUD

École Doctorale Ondes et Matière

THÈSE DE DOCTORAT

Spécialité Lasers et Matière

Présentée pour obtenir le grade de

DOCTEUR EN SCIENCES DE L'UNIVERSITÉ PARIS-SUD

Limin MENG

Etude expérimentale et simulations numériques des propriétés spectrales de lasers X pompés par excitation collisionnelle.

Experimental study and numerical simulations of the spectral properties of XUV lasers pumped by collisional excitation.

Soutenue le 20 Décembre 2012

M Jean LAROUR,	Rapporteur
M Roland STAMM	Rapporteur
M Djamel BENREDJEM	Examinateur
M Olivier GUILBAUD	Examinateur
Mme Sylvie JACQUEMOT	Examinatrice
Mme Annie KLISNICK	Directrice de thèse

Acknowledgements

My Ph.D was prepared at ISMO of University Paris-11 Sud, CNRS, between October 2009 and December 2012. I would like to thank the Director, Professor Philippe Bréchignac, and the leader of Equipe B, Dr. Danielle Dowek, for giving me this opportunity and for their support.

My deepest gratitude goes first and foremost to Dr. Annie Klisnick, my supervisor, for her constant encouragement and guidance. She walked with me through all the 3 years of my Ph.D and the writing of this thesis. Without her assistant and illuminating instruction, this thesis could not have reached its present form. I learnt a lot from her in the experiments and the research methods of science, which will be useful for all the future. She also gave me many advice and help in my life in France and in my learning of French. Moreover, her kind family, Mr Patrice and their children were help for me a lot in my life.

I would like to express my heartfelt gratitude to all my collaborators in my work, they are Jorge Rocca, Mario Marconi, Lukasz Urbanski et al. at Colorado State University; Olivier Guilbaud, Kevin Cassou, Sophie Kazamias, Moana Pittmann, Julien Demailly, Sameh Daboussi from LASERIX team; Serena Bastiani, Anne-Claire Bourgaux at LULI; Fabien Tissandier, Philippe Zeitoun et al at LOA; Michaela Kozlova et al. at PALS; Denis Joyeux, Sébastien de Rossi at LCFIO. Thanks a lot for all your help in my experiment. And also, thanks to Olivier Guilbaud at LPGP, Annette Calisti et al at PIIM and M Berrill at CSU, thank you very much for the assistance in theoretical work. Without your help, it is impossible to complete my PhD work.

I would like to thank all the members of the Jury, M Roland Stamm, M Djamel Benredjem, M Olivier Guilbaud, Mme Sylvie Jacquemot, they gave me valuable advices to consummate my thesis.

I woud like to thank the secretary, Mme Martineau, Mme Salou (ISMO) and Mme Basset (EDOM) et al for their kind assistance. Thanks a lot for help me in the inscription and the other day life of foreigner students.

My thanks would go to all my colleagues work in LIXAM and ISMO, Thanks to Andréa, who worked with me at the end of my thesis. She gave me many useful advices and contributed to several figures in the manuscript. Thanks also go to Osman Atabek, Eric

Charron, the colleagues Raiju, Sonia, Kevin, Amine, Martine, Jacques, Marc, Olivier, and my officemate Jean-Yves, thanks a lot for taking me a lot of happy time in my PhD life.

I would like to give my thanks to the embassy professors who are in charge of the Chinese students in France, Mme Zhu Xiaoyu, M Zhang Xiaotao, Mme Qiang Yaping and Zhao Jingmei et al. They gave me a lot of help and supports in my life.

I would like to thank my colleagues in the Union of Chinese Students in France, Xiao Yimin, Liu Xiangye, Li Xuwen, Chen Yuanyuan, Dang Wenjun, Lv Zhihan, Liu Juanjuan, Xu qiongfei, Hu Xuan, Zhang Chun, Hu Haofeng, Jiang Lijun, Zang Tong, Cai Yin et al; and Gao Sheng, Yan Cong, Wei Ailun, Zhang yue, Zhang qian, Mou Rong, Zhang Xiaomo, Liu Xinyu, Jia Zixian, Xu Xiaozhou, Bai Yandong, Tang Yingcen, Chen Zhesheng, Li Zhenzhen, Liu Dongya, Fuwenhao, Sang Rui, Zhang Yang, Chen Yonggui, Lei Hongxi, Chen Zhuowei, Wang Ke and Hu Yuhan, Du Jiawen et al. I am very glad to know you all in France during my Ph.D time, We worked together to organize students activities, help each other. We are friend forever.

I would like thank my best friends, Wang Jijin, Li Dikai, Shu Tan, Chen Peng, Huang Jin, Zhu Yueqiu, Zhang Linlin, Feng Teng, Lu Lili, Jia Juanjuan, Tang Qingshan, Hu Yong, Liu Bo, He Jibo with his familly, Ding Peixuan, Ji Botao, Qu Huanhuan, Hai Xiaodong, Li Yingyi, Cui Huan, Liu Jiagui, Xu Chenghai, Yao Liwen, Li Lu, Xiao Ji, Xu Xiao, Xiang Yang, Shen Ke, Lin Guoping, Luo Zhengjie, Zhang Lu, Meng Sha, Yu jie, Shi Lingyan, Xu Ying, Dou Zhiwei, Xie Ning, Li Chengjun, Li Sha, Wang Bo, Wang Fangyu, Momo, Qu Long, Zhao Lisha, Luan Qiaochu, Li Ronghua ...et al. I can not write all your names, but I will not forgot every happy time of us. Thank you for spending 3 years of life with me in France.

Finally, I would like to thank my family, not only for the PhD time but for all my life, they gave me strong support, help me to go through all my students times. Especially my Grandfather, M Meng Xianbin, a retired soldier, who takes care and supports me all the time. Without my family, I can not get such an honor.

CONTENT

Introduction

The demonstration of seeded XUV lasers, generated by either transient collisional excitation in solid target plasmas or optical-field-ionization in gaseous targets has opened new prospects for the utilization of high-brightness plasma-based coherent XUV sources for various applications. The use of high-order harmonic generation (HHG) pulses as a seed has led to a dramatic enhancement of the spatial coherence over those exhibited in amplified spontaneous emission (ASE) operation. The degree of temporal coherence is an important parameter that also needs to be characterized for applications. The coherence time is linked to the spectral width $\Delta\nu$ of the laser line through $\tau_c \sim 1/\Delta\nu$. As a result the spectral width also determines the ultimate minimum pulse duration that can be achieved. The shortest pulse duration measured to date for a seeded XUV laser is ~ 1.1 ps in a Ne-like Ti plasma [1]. In order to make further progress towards shorter pulse XUV lasers it is important to obtain experimental information about the spectral characteristics of these sources. This is a challenging measurement because the narrow linewidth of XUV laser lines (typically $\Delta\lambda/\lambda \sim 10^{-5}$) typically lies beyond the resolution limit of existing spectrometers in this spectral range.

Over the last ~10 years, ASE XUV lasers pumped by collisional excitation of Ni-like and Ne-like ions have been generated worldwide in plasmas created both by fast electrical discharge, or by various types of high-power lasers. This leads to a variety of XUV laser sources with distinct output properties: capillary-discharge, quasi-steady state (QSS), transient, or optical-field ionization (OFI) XUV lasers. Although the same pumping mechanism, essentially collisional excitation by free electrons, is common to all these XUV laser systems, the plasma parameters (electron density N_e, electron temperature T_e and ion temperature T_i) in the amplification zone are markedly distinct. As a result, the relative contributions of the spectral broadening processes (Doppler, collisions) that affect the lasing line are also significantly different.

The motivation of our work is to thus better characterize the spectral properties of existing plasma-based XUV lasers.

In chapter 1, we first introduce XUV laser generation in hot and dense plasmas, and compare this source to two other high-brightness XUV sources. We describe in detail the collisional excitation pumping and discuss the four different regimes that were demonstrated

experimentally: Quasi-Steady State (QSS), Optical Field Ionization (OFI), capillary-discharge and transient. We explain how the XUV laser is amplified in the plasma and we recall the main features of laser-generated plasmas. Finally we present the main bases of the formalism and processes involved in the spectral and coherence properties of the XUV lasers. We discuss in detail the different mechanisms involved in the formation of the spectral profile of the XUV laser line, including the plasma broadening effects affecting the emitting ion and the modification of the profile following amplification. We also discuss the relationship between the linewidth and the minimum pulse duration for several types of profile.

In chapter 2, we present the results of our simulation work on the spectral shape and width of the amplified laser line. Our calculations are based on a 1D-radiative transfer code, which includes the effect of saturation for a general Voigt-type profile. The profile before amplification is taken from detailed calculations performed by colleagues from PIIM (University of Aix-Marseille) using the PPP code. We discuss the behaviour of the XUV laser spectral profile for different plasma parameter situations and the Fourier-transform limit duration that can be reached in each case.

In chapter 3, we present the instruments that we have used for our experimental work, namely a wavefront division interferometer and a high-resolution X-ray Streak camera. We describe the method that we used to process the interferograms and to measure the temporal coherence and the spectral width of the XUV lasers discussed in chapter 4.

In chapter 4, we present our experimental results. We have measured the temporal coherence of three different types of XUV lasers pumped by collisional excitation, having each a specific spectral behaviour due to different plasma conditions in the gain zone. The results of these experiments are analysed and discussed separately. The last experiment was devoted to a study of the temporal behaviour of a transient XUV laser as a function of the pump parameters. At the end of this chapter, we compare all these XUV lasers studied during the thesis work, also including the OFI XUV laser which was studied previously with the same interferometer.

The conclusion summarizes the results and gives perspectives for the future.

1. Y. Wang, M. Berrill, F. Pedaci, M. M. Shakya, S. Gilbertson, Zenghu Chang, E. Granados, B. M. Luther, M. A. Larotonda, and J. J. Rocca, “Measurement of 1-ps soft-x-ray laser pulses from an injection-seeded plasma amplifier”, PHYSICAL REVIEW A **79**, 023810 (2009).

Chapter 1: XUV lasers generated in hot dense plasmas

1.1 Introduction

There have been spectacular advances in the field of high-brightness coherent sources in the XUV spectral range over the last 10 years. This range covers electromagnetic radiation with wavelength typically ranging between 2 nm and 50 nm, as shown in Figure 1-1.

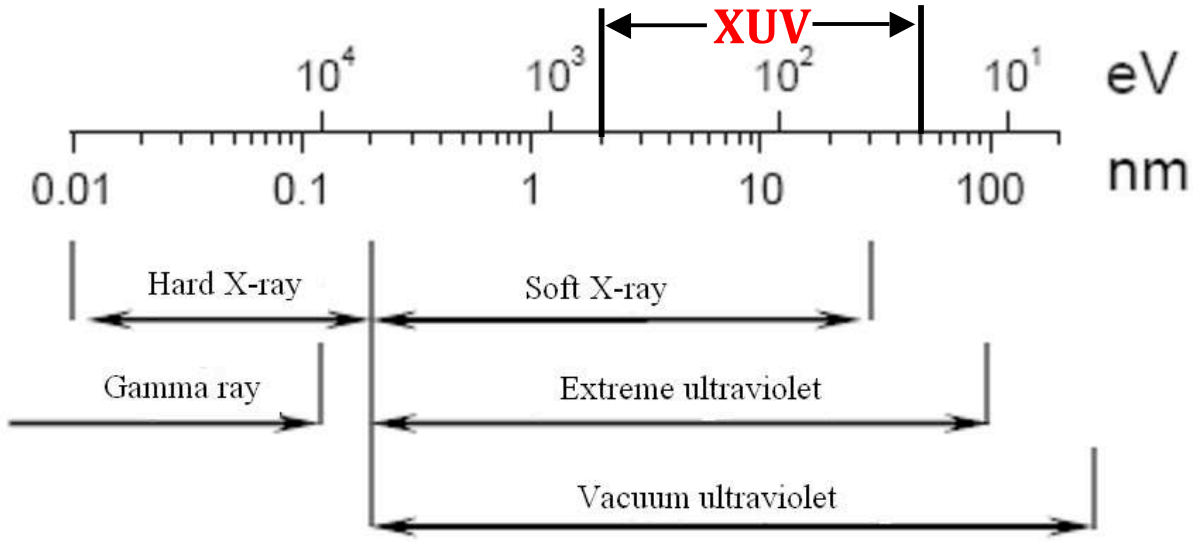

Figure 1-1. Electromagnetic spectrum in the short wavelength domain. The XUV range is outlined.

Three main types of techniques were used to generate coherent XUV sources with unprecedented characteristics in terms of peak spectral brightness, pulse duration, etc, thus opening new fields of applications. In this thesis we have focused on one of them, XUV lasers generated from hot and dense plasmas, which will be introduced in detail in this chapter. The two other sources that we will briefly introduce are: high-order harmonics generation (HHG) from femtoscond laser and XUV free-electron lasers (XUV-FEL) from accelerators. These two sources have specific characteristics, which are complementary from plasma-based XUV lasers, but they share also some common properties.

1.1.1 High-order harmonic XUV radiation

High-order harmonic generation from a high-intensity, femtosecond laser is a phenomenon that has both microscopic and macroscopic aspects. The creation of harmonic radiation by dipolar interaction between a rare gas and a femtosecond laser pulse is linearly polarized at the atomic scale. The quantum models can explain this process and predict the amplitude and the phase of the polarization created. During the interaction of an intense infrared laser field ($I \sim 10^{14}$ W/cm²) with the gas atoms, there is a partial ionization of the atoms by tunnelling processes [1]. The electrons produced by this ionization are accelerated in the laser field, and

then they recombine with their parent ion. It is during this recombination that the harmonic frequencies of the fundamental pump laser frequency are emitted, up to orders that can be very high (~100), thus reaching the XUV spectral range [2]. For reasons of symmetry, only odd orders harmonics are generated [3]. The spectrum is thus a comb of odd harmonic lines with intensity almost constant over a large range, followed by a rapid decrease [4]. These sources deliver a train of ultrashort pulses with duration ~100 attoseconds, a timescale which was never reached by any other source. This is an advantage for applications that require high temporal resolution to probe phenomena such as very short movement of electrons in atoms or molecules. In addition, the harmonic beam has good optical qualities, such as high spatial coherence. As we will see, this was used to improve the coherence properties of XUV lasers, by using HHG radiation as a seed of plasma amplifiers [5-7]. Seeding of XUV laser plasmas with HHG radiation is also a way to increase the energy of HHG pulses, which are currently limited to ~1μJ in the 30-40 nm range, and down to ~10 nJ below 20 nm [8].

1.1.2 XUV free-electron lasers

Synchrotron radiation is emitted when a charged particle is subject to acceleration. This effect was used since the 1970s to devolop synchrotron radiation facilities where the source covers a spectral range from infrared to X-ray. By the 1990s, the third generation synchrotrons began to appear, as the ESRF (European Synchrotron Radiation Facility) in Grenoble, or SOLEIL in France. The peak power of the sources of this generation is about 10^4 - 10^5 Watts and pulse duration is of the order of ~100 picoseconds.

The X-ray Free Electron Lasers (XFELs) represent the fourth generation synchrotrons. They produce radiation pulses at intensities several orders of magnitude higher than those of the third generation machines. The source principle of this generation is to combine the synchrotron radiation with the characteristics of source pumped by laser. The idea is to replace the amplifying medium by a relativistic electron beam produced by a particle accelerator. Indeed, relativistic electron bunches are injected into an undulator where there is a spatially periodic magnetic field. Periodically deflected electrons emit synchrotron radiation of short wavelength. The electrons with lower speed absorb emitted photons and are accelerated before emitting photons at shorter wavelengths. The beam is then amplified by a single pass through undulator structure effect by SASE (Self Amplification of Spontaneous Emission). The wavelength of the X-FEL varies continuously with the magnetic field of the inverter and the kinetic energy of electrons, resulting at the end in a tunable coherent source.

The pulse duration, which depends on the pulse duration of the bunch of particles is very short, of the order of 100fs. In addition, the beam has good optical properties: low divergence, linear polarization and high spatial coherence. The temporal coherence is however limited.

The unprecedented, ultra-high peak brightness reached by XFELs opens new possibilities of exploration in innovative fields such as Warm Dense Matter [9], of flash-imaging of complex molecules. [10]. In the XUV range the first demonstration of free-electron lasing was achieved at the FLASH facility in Germany [11]. More recently lasing was extended to the soft X-ray range at the LCLS facility in the US [12] A number of facilities are currently under contruction or planned in several countries. However, the high cost and limited access to such facilities are real limitations to its useness. Thus smaller-scale sources, like plasma-based XUV lasers, which can be implemented at the laboratory or university scale, even with more modest performances, are still worth being developed.

1.2 Pumping schemes for XUV lasers

The emission of XUV laser relies on on the creation of a population inversion between two atomic levels separated by an appropriate energy. Because of this population inversion, radiation at the wavelength of the corresponding transition will be amplified by stimulated emission of radiation. It was in the early 70s that the first observation of population inversions in the XUV domain was reported [13]. Mainly two different pumping schemes were then actively investigated: the recombination pumping and the collisional excitation pumping.

Recombination pumping can be induced by the rapid cooling of a plasma which is initially ionized and heated by a relatively short (ps to ns) laser pulse [14, 15]. Recombination pumping was also observed in a plasma directly ionized by the electromagnetic laser field (Optical Field Ionization: OFI) [16]. Recombination pumping demand less driver laser energy than the collisional excitation pumping that will be presented in detail below. It can in principle be extended to wavelengths below 1 nm, thus at shorter wavelength than with the collisional excitation pumping whose limit is about 3 nm. However until now only modest amplification has been achieved with recombination.

The first unambiguous demonstration of XUV laser emission was reported in 1985 [17], in a selenium plasma pumped by a kJ-class laser at Livermore Lab (US). Enormous progress has been made since then in terms of wavelengths and output characteristics, through a better control of the pumping schemes and of the creation of the amplifying medium. This progress

has also benefitted from the spectacular development of the high-power lasers used as a pump, especially through the advent of the CPA (Chirped Pulse Amplification) technique in the late 80s [18]. As we will explain below, the use of picosecond pulses delivered by high-power, CPA lasers, has led to a substantial reduction of the pump laser energy required to generate XUV lasers, lowering from several kilojoules to a few joules. At the same time the repetition rate was significantly increased, typically up to 10Hz instead of a few shots per hour.

As we will see, all the operational XUV laser rely on the same pumping mechanism, namely collisional excitation of highly charged ions, but different techniques of plasma creation were used. This leads to a variety of XUV laser sources, with different characteristics in terms of lasing wavelength, output energy or pulse duration. As mentioned above, significant improvements have been achieved recently, especially in terms of spatial coherence of the beam, through the amplification of high order harmonics in the gain medium of XUV laser [5, 6].

Finally XUV laser applications are developed in parallel with progress of sources. First encouraging experiments demonstrate the importance of these sources for studies for various applications such as dense plasma probing [19, 20], high-resolution microscopy [21], nano-patterning [22], and in various fields such as warm-dense matter physics [23], physical chemistry [24], laboratory astrophysics [25] or condensed matter physics [26].

1.2.1 Collisional excitation pumping of Ne-like and Ni-like ions

In this pumping mode, collisions of free electrons with multicharged ions in their ground state are the direct cause of population inversions. Indeed, the upper level of the laser transition is populated by collisional excitation from the ground state of the lasing ion, while the lower level is rapidly depopulated by radiative decay to the ground state, as shown by the diagrams presented in Figure 1-2.

The spontaneous radiative decay of the upper level to the ground state is prohibited by selection rule. In order to populate efficiently the upper level of the lasing ions, the average energy of the free electrons must be equal to or greater than the energy difference between the upper level and the ground state. As a result, the plasma electron temperature must be high, namely a few hundreds of electron volts. On the other hand for the collisional excitation to be probable, the electron density must be high, typically of few 10^{20} cm^{-3}. Finally the ion species

which are the most appropriate for this pumping scheme are those which have a closed-shell configuration in the ground state, in particular neon-like and nickel-like ions. This is because they have a high ionization energy. They are thus more difficult to ionize and they can be produced in the plasma with a larger abundance.

Figure 1-2 shows the different transitions on which population inversions can be achieved by collisional excitation pumping. These transitions are between excited states with the same prinipal quantum number ($\Delta n = 0$): 3p - 3s for Ne-like ions and 4d - 4p for Ni-like ions. In both ions the component with upper state J=0 to lower state J=1 gives the largest population inversion. This is because the largest excitation rate from the ground state level (J=0) is the monopole excitation rate [27].

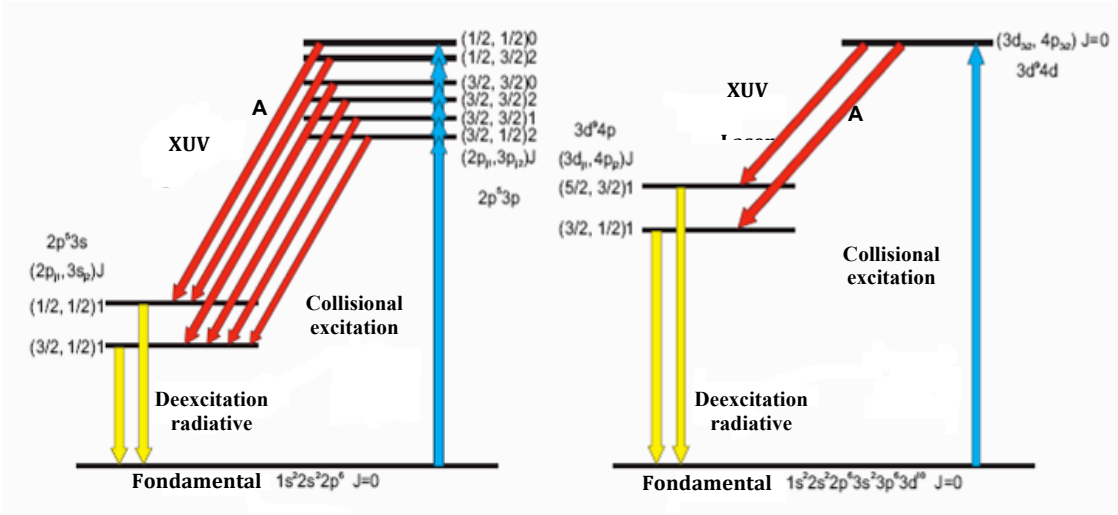

Figure 1-2: Diagram of pumping by collisional excitation. Left) neon like ion, the transition A is the most intense among the six possible transitions. Right) nicklellike ion. Transition A is more intense for atoms of high atomic number [28].

Collisional excitation pumping was demonstrated in many elements in the Ni-like and Ne-like isoelectronic series. The wavelength of the lasing transitions decreases when the atomic number of the lasing element increases. Ni-like ions are more favourable than Ne-like ions to reach lasing wavelength below 15 nm, because the ratio between the laser transition energy and the excitation energy is higher [28].The shortest wavelength at which (weak) lasing was observed is $\lambda = 3.5$ nm in Ni-like gold [29].

Collisional excitation pumping in plasmas was achieved in essentially four different configurations, and by different techniques illustrated in Figure 1-3. These different techniques have led to 4 types of XUV lasers with different output characteristics, referred to as: (a) QSS (quasi-steady state), (b) OFI, (c) capillary discharge, (d) transient. We will now

introduce each of them and show that the plasma parameters in the gain zone are different in each case, which is of particular interest for the study of the spectral behaviour of the lasing lines.

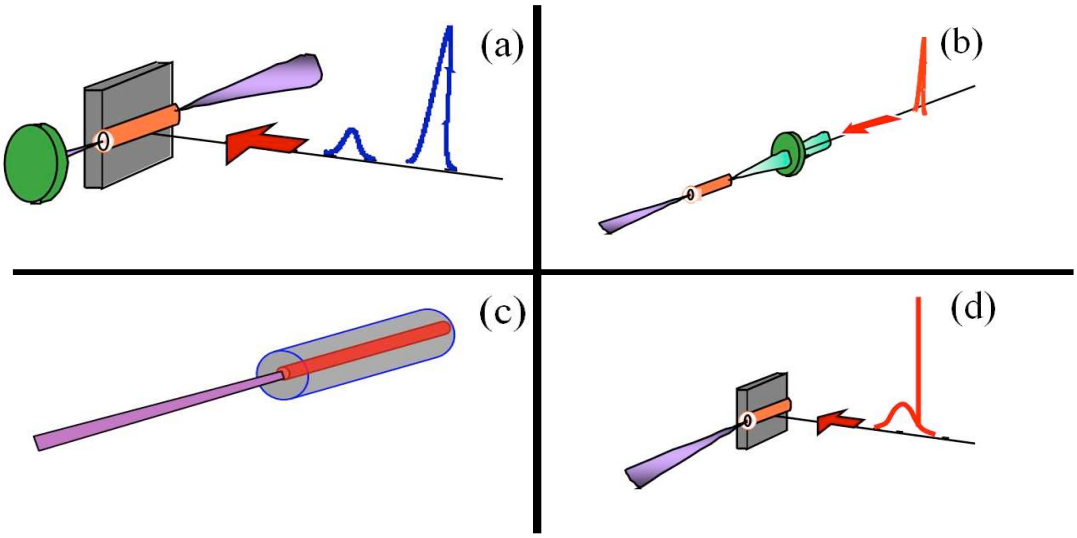

Figure 1-3. Schematic representation of 4 types of collisional XUV lasers: (a) quasi-steady state XUV laser; (b) OFI XUV laser; (c) capillary discharge XUV laser; (d) transient XUV laser

1.2.2 Quasi-steady state pumping

The generation of collisional excitation pumping XUV lasers in the quasi-steady state (QSS) regime requires a pump laser energy of typically a few hundred joules to 1 kilojoule, with a pulse duration of the order of 0.5 to 1 ns [30, 31]. It was thus studied in high-energy lasers installations. The main pulse is preceded by a low energy prepulse to reduce the effect of refraction, which will be discussed below. Since the gain coefficient achieved is relatively low, saturation of amplification is reached by operating in a half-cavity configuration, in which the XUV beam go through the gain medium twice (see Fig. 1-3 (a)).

An example of QSS XUV laser operation is currently the PALS XUV laser (Prague, Czech Republic), where one of the experiment described in this manuscript was carried out. This is a neon-like zinc laser emitting at 21.2 nm. The XUV laser beam produced with half-cavity delivers 4 to 10mJ per pulse depending on the delay between the prepulse and the main laser pulse [32]. The duration of the XUV pulse is about 150 ps. These features make this laser the most energetic XUV laser in the world. It is commonly used as a source for scientific studies [33].

In Ne-like Zn XUV laser, the plasma parameters in the gain region are typically [34]: N_e~2-5×$10^{20}$$cm^{-3}$, kT_e~ 150-200eV, kT_i~ 200-300eV.

Despite the fact that the quasi-steady state XUV lasers are currently the most energetic coherent XUV sources, the large pump energy required restricts them to large-scale facilities with low repetition rate of 1-2 shots per hour. It was thus necessary to develop sources with more compact and economical installations as we shall see below.

1.2.3 Optical-Field Ionization pumping

The interaction of a high-intensity femtosecond laser pulse with noble gas atoms can also lead to the generation of a source different from the high order harmonics described in the introduction of this chapter: OFI (Optical Field Ionization) XUV laser. The mechanisms of creation of population inversions are the same as those used in the QSS XUV lasers, ie electron-ion collisions. The femtosecond laser pulse, with few hundred millijoules of energy, is focused into a jet of gas, as shown in Fig. 1-3 (b). The intensity of the pump laser should be of the order of 10^{17}W/cm ², and its polarization must be circular [35, 36]. Noble gas atoms are ionized by the tunnel effect as a result of the intense laser field, which distorts the Coulomb potential barrier. The laser intensity controls the highest ionization stage that can be reached. Here it is chosen to produce a large abundance of neon-like, nickel like, or palladium like ions.

The first observation of lasing with the OFI technique was reported by Lemoff et al. [37] in Pd-like Xe. The technique was extended to Ni-like Kr by the group of S. Sebban at LOA (Palaiseau) in 2000 [38]. The first spectacular demonstration of seeding with HHG was achieved by the same group in 2004 [5]. The optical quality of the beam, in particular its spatial coherence, was remarkably improved [39].

The typical duration of the XUV laser pulse was estimated as ~5 ps [7]. The output energy of the OFI-pumped XUV lasers is relatively low, of the order of 1 μJ or less. However recent experiments performed in Taiwan have shown that this energy can be increased by operating at a higher gas density with a preformed plasma waveguide [40]. However one of the main drawback of OFI-pumped XUV lasers is the limited number of available lasing wavelengths.

In Ni-like Kr XUV laser, the plasma parameters in the gain region are typically:

N_e~10^{18} cm^{-3}[41], kTe~ 450$_e$V [38], kT_i~ 6eV[42].

1.2.4 Capillary-discharge pumping

It was proposed in the 1980s to generate a capillary-discharge XUV laser, where plasma creation is based on electric shock. The first demonstration of lasing at 46.9 nm in Ne-like Ar was reported by the team of J.J.Rocca at Colorado State University in 1994 [43]. This XUV laser source has been then optimized by the same team and it is now a reliable source used for many applications [44].

To generate this XUV laser emission, a pulse of electric current (duration ~20ns, peak intensity ~few kA) ionizes the gas and creates a plasma along a tube of a few millimeters in diameter and ~30 centimeters in length, filled with argon gas. The Lorentz forces, which result from the interaction of the current with the magnetic field, lead to a strong radial compression of the plasma column. As a result the temperature and the electron density increase and the plasma is ionized. When the compression is maximum, population inversions in Ne-like Ar are produced and XUV laser emission is observed at the output of the plasma column (see Fig. 1-3 (c)).

The gain coefficient is relatively low but saturation of amplification can be reached due to the great length of the plasma amplifier. The energy of the XUV pulse can be as high as 1 mJ, for a duration of the order of 1 ns. Despite the fact that capillary-discharge XUV lasers are available only at the single wavelength of 46.9 nm, and that their pulse duration are relatively long, they have a high pulse energy and they can be operated at a high repetition rate of 7 Hz [45]. They are thus good candidates for applications such as interference lithography [22].

In Ne-like Ar XUV laser, the plasma parameters in the gain region are typically [46]: N_e~$1.8*10^{18}$ cm^{-3}, kT_e~ 100eV, kT_i~ 100eV.

1.2.5 Transient pumping

Transient pumping was proposed by Afanasiev and Shlyaptsev in 1989 [47], and has led to remarkable progress in the development of XUV lasers. The expansion of this method in many laboratories worldwide has been favored because of the parallel development of High-power CPA lasers.

Transient pumping involves using two laser pulses separated by a delay of a few hundred picoseconds (see Fig. 1-3 (d)). The first pulse, called "long pulse" with a few hundred picoseconds duration, is focussed on a solid target to create plasma with a good degree of ionization. The second pulse, called "short pulse" with a duration of a few picoseconds, heats the free electrons abruptly, allowing for an efficient pumping of the lasing ions by collisional excitation. The heating time of the electrons by the short pulse is much shorter than the ionization time of the plasma, so that the electrons reach high temperatures of several hundred electron volts, without destroying the lasing ions by further ionization.

Very high gains of several 10 cm^{-1} can be achieved with the transient pumping, so that saturation of amplification can be reached even with targets only a few millimeters long [48]. Because of the short gain lifetime of a few picoseconds, it is necessary to apply a traveling wave pumping, ie the energy wavefront of the main short pulse should be tilted by 45° [49].

Further improvement of the pumping efficiency and reduction of the pump energy was obtained by irradiating the preformed plasma with the second picosecond pulse under a small grazing angle (typically 15-20°), in the so-called GRazing Incidence Pumping (GRIP) geometry [50]. This geometry, which inherently provides traveling wave pumping, increases the path length of the pump laser rays in the gain region of the plasma, thereby increasing the fraction of the pump energy absorbed in that region. Under grazing incidence, the pump beam is refracted in the plasma density gradient, like a usual mirage effect. The density of the turning point N_{e0}, which is also the density at which laser absorption is maximized, is entirely defined by the grazing (GRIP) angle θ and by the wavelength λ_p of the pump laser, following the relation: $\sin\theta \approx \sqrt{N_{e0}/N_{cp}}$, where N_{cp} is the critical density corresponding to the pump laser wavelength. The GRIP angle is thus chosen so that N_{e0} and the electron density of maximum gain coincide.

Thanks to the GRIP geometry, the pump energy required to generate transient XUV lasers was further reduced compared to normal incidence pumping. As a result, GRIP transient XUV lasers were generated using Ti-Sa CPA laser drivers, instead of Nd-glass lasers, leading to a significant increase in the repetition rate, up to 10 Hz [51]. New developments of this pumping scheme, involving the optimization of the irradiation geometry [52] or the use of prepulses [53], have been achieved worldwide over the last ~5 years. They have led to stable and well characterized saturated XUV lasers being now operational at various wavelengths ranging from 32.6 nm (Ne-like Ti [54]) to 8.8 nm (Ni-like La [55]), with less than 10-J of

pump laser energy. The duration of gain lifetime as well as that of the XUV laser pulse are significantly shorter than what is obtained in the QSS regime, namely a few picoseconds. This aspect will be investigated and discussed in chapter 4. The output energy of transient XUV lasers is or the order of a few μJ.

The transient collisional pumping offers several advantages: it can generate XUV sources with a pump energy of only a few joules, which allows for compact installations called "table-top", making them good candidate for XUV applications. Several XUV lasers facilities are available or under construction in the world. One of the most advanced among them is the installation LASERIX University Paris Sud (France), which is based on a laser driver which delivers pulse 500ps-2J to 1ps-2J at a repetition rate of 10 Hz.

Seeding transient XUV laser amplifiers with high-order harmonic radiation was demonstrated in 2006 by the group Prof. Rocca at CSU in Ne-like Ti plasma at 32.6 nm [56], and more recently in Ni-like Ag (λ= 13.9 nm) and Ni-like Cd (λ = 13.2 nm) [6]. The optical quality of the amplified harmonic beam was observed to be substantially improved [57]. Finally, during this thesis we have been involved in the characterization of the temporal coherence and spectral width of a seeded transient XUV laser emitted at 18.9 nm in Ni-like Mo. The results will be presented and discussed in chapter 4.

In Ni-like Mo XUV laser, the plasma parameters in the gain region are typically: $N_e \sim 10^{20} cm^{-3}$ [58-60], $kT_e \sim$ 250-500eV [58, 61, 62], $kT_i \sim$ 47eV[58].

1.3 Amplification of XUV lasers in plasmas

In a conventional laser, the active (inverted) medium is placed in a resonant mirror cavity in which radiation will oscillate and intensity will grow. This solution is not applicable to XUV lasers for mainly two reasons: (i) highly reflective mirrors at normal incidence are not available in the XUV spectral domain; (ii) the lifetime of population inversions is of the same order of, or even shorter than the transit time of the photons in a single pass. Thus XUV lasers are usually operated in single-pass, Amplification of Spontaneous Emission (ASE) mode. In this ASE mode, spontaneous emission at the lasing wavelength induces stimulated emission, which is preferably amplified (in both directions) along the length of the active medium. In order to maximize the extraction of energy a large gain-length product is required, possibly reaching saturation of amplification (g.L ~ 15-20).

Hence in order to generate a saturated XUV laser, both the gain coefficient and the amplifying length must be large enough, so that the gain-length product is of the order of 15 or larger. In laser-produced plasmas, we will see that the refraction of the XUV radiation in the strong density gradient can prevent an efficient propagation and amplification. We will first recall the main temporal and spatial features of laser-produced plasmas.

1.3.1 Structure of laser-generated plasmas

When a high-power laser beam interacts with a solid target, a plasma can be created if the laser intensity is greater than approximately 10^8W/cm ². In this case the first free electrons are created by multiphoton absorption from the first moments of interaction (less than a few picoseconds). They are then accelerated by the electric field of the laser wave and collide with the electrons of the atoms linked to the target. These create new electrons and leads to the formation of the plasma that expands rapidly in the opposite direction of propagation of the laser beam. In reaction to the relaxation effect of the plasma a shock wave takes birth propagating towards the interior of the target (the principle of rocket effect). Plasma is macroscopically characterized by two important parameters, temperature and density, which evolve rapidly in both time and space.

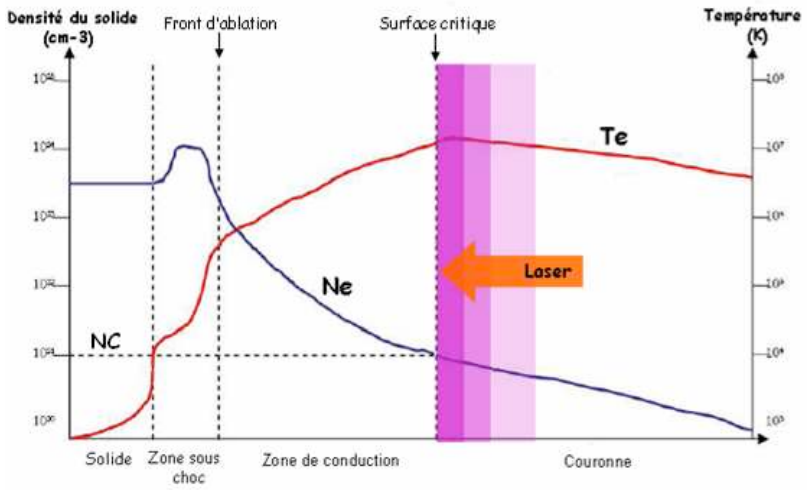

Figure 1-4: Structure of a plasma created by a nanosecond laser pulse. The laser wave is reflected at the critical surface. Te is the electron temperature, Ne is the electron density, and Nc is the critical density [63].

Figure 1-4 shows a schematic evolution of the electron temperature and density as a function of the distance to the target surface, at a given time during the laser pulse irradiation. The laser beam penetrates from the right and is absorbed and reflected at the critical density. Critical density is an important quantity for the laser-plasma interaction. The critical density is due to the fact that the free electrons which are accelerated by the laser field come into collective oscillation at a particular frequency ω_{pe} that resonates with the oscillation frequency

ω of the laser field. This plasma frequency ω_{pe} is obtained from the dispersion equation of the electromagnetic wave and is given by the following expression:

$$\omega_p = \sqrt{\frac{N_e \times e^2}{m_e \times \varepsilon_0}} \qquad (1\text{-}1)$$

where N_e denotes the electron density of the plasma, e is the electron charge, m_e is the electron mass, and ε_0 the vacuum permittivity.

For the laser with frequency ω, the refractive index of the plasma depends on the electron density through the relation:

$$n^2 = 1 - \frac{\omega_p^2}{\omega^2} \qquad (1\text{-}2)$$

The critical density corresponds to the density at which the free electrons oscillate at the frequency of the laser, when the refractive index becomes zero, and the incident laser wave is strongly absorbed and reflected. The critical density can be expressed as follows:

$$n_{cr} = \frac{4\pi^2 c^2 m \varepsilon_0}{\lambda^2 e^2} \qquad (1\text{-}3)$$

where λ is the wavelength of the incident laser.

For the Ti:Sa pump laser (λ = 0.8 μm) used to generate GRIP transient XUV lasers, the critical density is thus of $N_c = 1.56 \times 10^{21}$ cm^{-3}.

The subcritical region ($N_e < N_c$), commonly called corona, is a region characterized by low density and high temperature (typically of the order of few 100 eV to keV). In this zone, the energy of the laser pulse is absorbed by two main processes: inverse bremsstrahlung (IB) absorption [64, 65], and resonant absorption, which occurs at the critical density. The former process is collisional absorption. The electrons oscillate in the laser field, making random collisions with ions, and absorbing photons in this process. The same process will occur with the wave after reflection at the critical surface. The IB absorption coefficient is inversely proportional to the electron temperature and increases with the intensity of the laser pulse. It is therefore necessary that the laser intensity is a compromise in order to create plasma hot enough while having a high absorption coefficient, its value at around 10^{14} W / cm².

Finally a portion of the laser energy deposited into the absorption zone is used for heating the electrons in the corona, where the temperature remains virtually constant, while the other part of the energy is transferred by conduction to the remainder of the plasma. In the

conduction zone, or overcritical region (N_e>N_c), the energy transferred to the target by thermal conduction and by electronic radiative transfer contributes to further ablate the target and to maintain the flow of plasma (ablation front). The expansion of the heated plasma created by reaction force tends to compress the material upstream of the front ablation (zone under shock).

As we have explained above, the population inversions created by collisional excitation pumping require a high electron density (~10^{20} cm^{-3}) and a high electron temperature (few 100 eV). They are thus created in the corona, just below the critical density, at the time when the temperature of the plasma is maximum, ie ~ the peak of the pump laser pulse. In the region below N_c there are strong electron density gradients, which affect the propagation and the amplification of the XUV radiation in the direction perpendicular to the gradient direction (ie parallel to the target surface), as we will see in the paragraph below.

1.3.2 Refraction of XUV laser beam

As the laser-produced plasma expands from the target surface into vacuum where the interaction takes place, the density of the plasma decreases very rapidly. In particular the gradient of electron density is very steep in the region close to the critical density N_c and then relaxes at larger distance from the target surface. Because of this density gradient, to which corresponds a variation of the plasma refractive index, the XUV beam propagating along the plasma in the direction parallel to the target surface undergoes refraction, as shown in Figure 1-5. If this effect is too strong, the beam can be bent away from the amplification zone, reducing the effective amplification length of the beam [66].

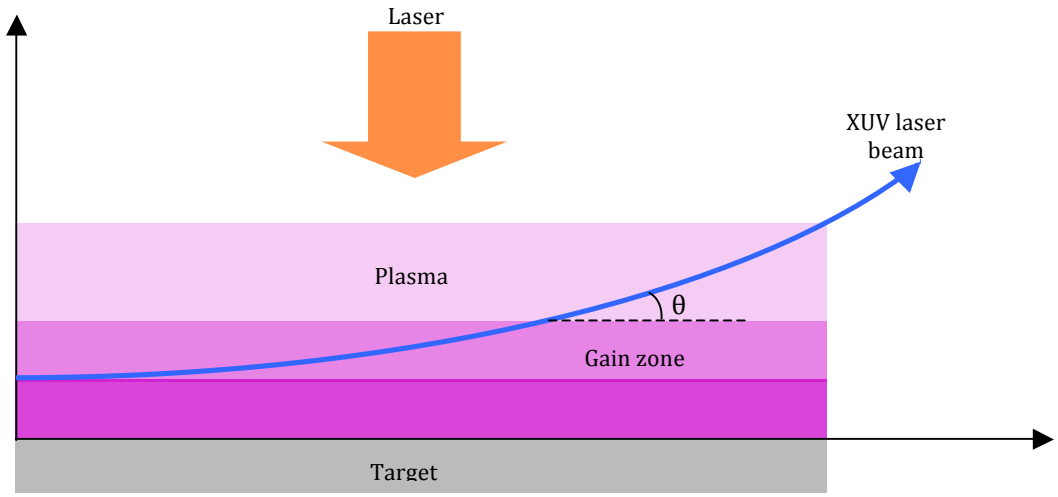

Figure 1-5: Refraction and propagation of a laser beam in a high density gradient XUV plasma.

Using equation (1-2) which assumes that the free electrons of the plasma have the dominant contribution, the refractive index n of the plasma is written:

$$n(x,y,z) = \sqrt{1 - \frac{N_e(x,y,z)}{N_c}} \qquad (1\text{-}4)$$

where $N_e(x, y, z)$ is the distribution of the electron density, and N_c is the critical density defined in (1-3).

Taking into account the fact that the critical density is greater than the electron density by several orders of magnitude, equation (1-4) can be rewritten as follows:

$$n(x,y,z) \cong 1 - \frac{N_e(x,y,z)}{2N_c} \qquad (1\text{-}5)$$

The change in the refractive index causes a slight deflection of the XUV beam, so the path of beam propagating in a medium of index variable is described by the following Eikonal equation:

$$\frac{d}{ds}(n\frac{dr}{ds}) = \nabla n(x,y,z) \qquad (1\text{-}6)$$

where $ds = \sqrt{dx^2 + dy^2 + dz^2}$ is the differential displacement along the beam trajectory and r represents the given position of the beam.

In the first QSS XUV lasers, refraction was a severe limitation that prevented to reach saturation. This problem was then addressed by using a low energy prepulse before the main heating pulse that helped to smooth the density gradient in the gain zone [31]. However refraction of the XUV laser cannot be eliminated completely and this leads to a small deflection of 2-10 milliradians of the beam at the output of the amplifying plasma.

1.3.3 Amplification in the small-signal gain regime

In this part we will recall the main equations that are used to calculate the intensity $I_\nu(L)$ of the XUV laser beam at the output of the amplifying plasma of length L. Here we assume that the XUV laser is operated in the so-called small-signal gain regime, ie well below saturation.

This means that the population inversion is not affected in a significant way by stimulated emission from the upper level.

This calculation is valid for an elementary volume dV of cylindrical length dl of homogeneous and stationary plasma, that is to say for which the variations in the density and temperature are considered negligible. In particular, we neglect the effects of refraction mentioned above. In the volume dV the plasma is characterized by its emissivity j(ν) and the gain coefficient g(ν), which correspond to a transition between two atomic levels with populations of upper and lower level N_2 and N_1 respectively. The equation of radiative transfer can be written:

$$\frac{dI(\nu)}{dl} = j(\nu) + g(\nu)I(\nu) \qquad (1\text{-}7)$$

where $I(\nu)$ is the radiation intensity in W.cm^{-2}.

The emissivity j (ν) is the spectral energy density radiated by spontaneous emission per unit volume and per unit time and is given by:

$$j(\nu) = \frac{N_2 h\nu A_{21}(\nu)}{4\pi} \qquad (1\text{-}8)$$

where $A_{21}(\nu)$ is the Einstein coefficient which represent the probability of spontaneous emission in the frequency interval [ν, ν+dν]. It is written as the product of the total probability of spontaneous emission A_{21} between two levels and the normalized function of spontaneous emission spectral profile Φ(ν):

$$A_{21}(\nu) = A_{21}\Phi(\nu) \qquad (1\text{-}9)$$

with $\Phi(\nu)$ satisfies:

$$\int_{-\infty}^{+\infty} \Phi(\nu) d\nu = 1 \qquad (1\text{-}10)$$

The gain g(ν) due to the difference of the population of the two levels is positive when $N_2 > N_1$ (population inversion). For radiation with a frequency in the range [ν, ν+dν] it is expressed by:

$$g(\nu) = \left(N_2 - \frac{g_2}{g_1} N_1 \right) \frac{c^2}{8\pi\nu_0^2} A_{21}(\nu) \qquad (1\text{-}11)$$

where g_1 and g_2 are the statistical weights of levels 1 and 2.

In equation (1-7), integrating along a length L of plasma, we obtain the analytical expression of the intensity $I(\nu)$:

$$I(\nu,L)=\frac{j(\nu)}{g(\nu)}\left(e^{g(\nu)L}-1\right) \qquad (1\text{-}12)$$

The quantities $j(\nu)$ and $g(\nu)$ depend on the profile of the line. We assume that the profile is the same for the two quantities. On the other hand, since the spectral width of the considered transition is very small compared to the frequency of the radiation, we can replace ν by the central frequency ν_0, which gives:

$$\frac{j(\nu)}{g(\nu)}\approx\frac{j_0}{g_0} \qquad (1\text{-}13)$$

where j_0 and g_0 are respectively the emissivity and the gain at the centre of the line. Equation (1-10) is then written:

$$I(\nu,L)=\frac{j_0}{g_0}\left(e^{g(\nu)L}-1\right) \qquad (1\text{-}14)$$

The spectrometers used to observe the XUV laser lines does not have sufficient resolution to resolve spectral profile of the line, thus what is measured is the spectrally integrated intensity

$$I=\int_0^{+\infty} I_\nu d\nu \qquad (1\text{-}15)$$

For a gain-length product typically greater than 3, and a Gaussian profile of the line, G. J. Linford [67] proposed an analytical expression that describes the behaviour of the integrated intensity as a function of the length of the amplifying medium

$$I=\frac{\sqrt{\pi}}{2\sqrt{\ln 2}}\Delta\nu\frac{j_0}{g_0}\frac{\left(e^{g_0L}-1\right)^{\frac{3}{2}}}{\sqrt{g_0Le^{g_0L}}} \qquad (1\text{-}16)$$

where Δν is the spectral full-width at half maximum.

According to equations (1-12) and (1-16) the intensity grows exponentially as a function of the gain-length product. But the intensity does not increase indefinitely with the length, and from a certain value it enters a saturation regime.

1.3.4 Amplification in the saturation regime

Saturation can be considered as the maximum of energy stored in the population inversion that can be extracted from the medium by stimulated emission. In other words, when stimulated transitions between the upper and lower become significant, it tends to decrease the laser gain which goes to zero. In the saturation regime the intensity stops growing exponentially and enters a linear phase as a function of the length. The amplified radiation is intense enough to significantly reduce the population of the upper level of the laser transition N_2, which has no time to recover by collisional excitation pumping. The saturation intensity I_{sat} is defined as the intensity for which the gain is reduced by half. It is expressed as:

$$I_{sat} = \frac{h\nu_0}{\sigma\tau} \tag{1-17}$$

Where $h\nu_0$ is the XUV laser photon energy, τ is the recovery time of the gain, which depends only on the rate of depopulation of the upper level of the transition, and σ is the cross section for stimulated emission, which is independent on populations.

$$\sigma(\nu) = \frac{h\nu_0}{c} B_{21}\Phi(\nu), \text{ with } B_{21} = \frac{c^3}{8\pi\nu_0^3} A_{21} \tag{1-18}$$

When populations reach equilibrium very quickly (steady-state), we can write for the saturated gain:

$$g(\nu) = \frac{g_0(\nu)}{1 + \frac{I}{I_{sat}}} \tag{1-19}$$

In the strongly saturated regime, where the gain $g(\nu) \to 0$, we can write from (1-14):

$$I(\nu, L) \approx j(\nu) \times L \tag{1-20}$$

1.4 Coherence of XUV lasers

Lasers beams are generally characterized by their optical properties such as their divergence, their wavefront or their coherence. The study of these points requires to define the spatio-temporal variation of the phase and amplitude of the electromagnetic field from one

point to another. In the present thesis we will focus more specifically on the temporal coherence properties of XUV lasers.

In the electromagnetic field as being constituted by superposing in time and space of elementary fields, coherence is defined as the correlation between these elementary fields at different points separated in time and in space.

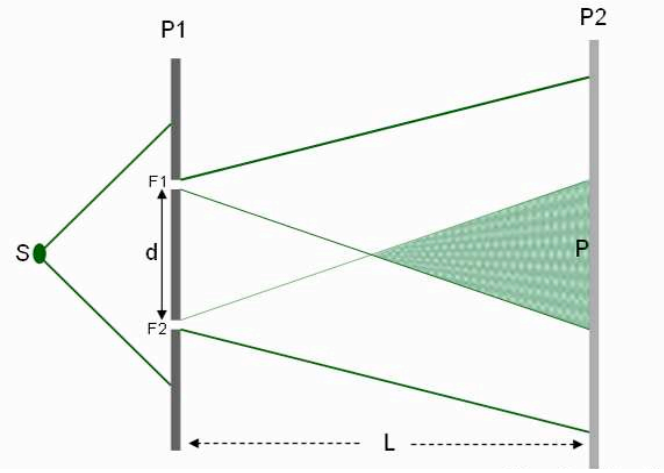

Figure 1-6: Observation of interference fringes with Young slits

Take the well-known Young's slits experiment represented in Figure 1-6. In the plane of observation P2, the intensity is not the sum of the intensity transmitted by each slit, but is inferred from the interference fringes which are formed in according to the coherence of the source S. Indeed in the case of Young's slits, the two secondary beams from the slits F1 and F2 have different amplitudes and phases arriving at the point P because they do not travel the same distance ($F_1P \neq F_2P$). Therefore the fringes formed in P can be brilliant (I_p max) or dark (I_p minimum). The path difference between the two beams can be expressed as a function of the wavelength λ by the following expressions:

$$\Delta\lambda = n\lambda \qquad I_p \text{ maximum}$$
$$\Delta\lambda = (n+1/2)\lambda \qquad I_p \text{ minimum} \qquad (1\text{-}21)$$

where I_P is the intensity at point P and n is an integer.

The visibility (or contrast) of the interference fringes, measured experimentally is defined by:

$$V = \frac{I_{max} - I_{min}}{I_{max} + I_{min}} \qquad (1\text{-}22)$$

where I_{max} and I_{min} are the maximum and minimum intensity in interference fringes. V then determines the degree of coherence of the source and varies between 0 (incoherent radiation) and 1 (full coherence).

To study more deeply the concept of coherence and show the relationship between visibility V of the observed fringes and the degree of coherence of the source, it is necessary to use a formal description of the correlation fields for example dealing with the Young's slits experiment using a complex representation of the fields.

In general, the (complex) quasi-monochromatic electromagnetic field is given by

$$E(r,t) = \varepsilon(r,t) \times \exp(-i\omega t) \tag{1-23}$$

where $\varepsilon(r,t)$ is a complex amplitude slowly variable and ω is the angular frequency of the wave. The intensity of a quasi-monochromatic source is then given by:

$$I(r,t) = \frac{c\varepsilon_0}{2}\left|E(r,t)\right|^2 \tag{1-24}$$

where ε_0 is the permittivity of free space.

For the Young slit case (Figure 1-6), the total field amplitude at the point P is given by:

$$E(P,t) = E_{F_1}(P,t) + E_{F_2}(P,t) \approx E(F_1, t-t_1) + E(F_2, t-t_2) \tag{1-25}$$

With $t_1 = \frac{r_1}{c}$ and $t_2 = \frac{r_2}{c}$, r_1 and r_2 are respectively the transit times and distances between P and the points F_1 and F_2.

The intensity at P is given by:

$$I(P,t) = E^*(P,t)E(P,t) \tag{1-26}$$

where E* is the complex conjugate of E.

Because of the fluctuations of the intensity of the emitting source, mainly caused by the random processes of spontaneous emission, it is necessary to take an average over the observation time [68]

$$\langle I(P,t)\rangle = \lim_{T\to\infty} \frac{1}{2T}\int_{-T}^{T} I(P,t)dt \tag{1-27}$$

Using expressions (1-25) and (1-26), and considering that the fields are stationary, we can write:

$$\langle I(P,t)\rangle \propto \mathrm{Re}\left\langle E^*(r_1,t+\tau)\times E(r_2,t)\right\rangle \tag{1-28}$$

with $\tau = t_1 - t_2$

We define the complex coherence function: $\Gamma(F_1,F_2,\tau)$:

$$\Gamma(F_1,F_2,\tau) = \left\langle E^*(F_1,t+\tau)\times E(F_2,t)\right\rangle \tag{1-29}$$

After normalization, we also define the complex degree of coherence $\gamma_{12}(\tau)$:

$$\gamma_{12}(\tau) = \frac{\Gamma(F_1,F_2,\tau)}{\sqrt{\Gamma(F_1,F_1,0)\Gamma(F_2,F_2,0)}} \tag{1-30}$$

The visibility or contrast of the fringes can then be expressed as:

$$V = \frac{I_{\max} - I_{\min}}{I_{\max} + I_{\min}} = \frac{2\sqrt{I_{F_1}\times I_{F_2}}}{I_{F_1}\times I_{F_2}} \times \left|\gamma_{12}(\tau)\right| \tag{1-31}$$

To summarize, the coherence function $\Gamma(F_1,F_2,\tau)$ characterizes the degree of correlation in F_1 and F_2 fields at τ time later. The relation (1-31) between V and $\gamma_{12}(\tau)$ makes it possible to directly infere the degree of coherence from the knowledge of the fringe visibility, and vice versa.

We distinguish two types of coherence: temporal (or longitudinal) coherence and spatial (or transverse) coherence. As illustrated in Figure 1-7, the temporal coherence concerns the correlation of the fields at a given point at two different times separated by a time τ. The spatial coherence concerns the correlation of the fields, at the same time, between two points F_1 and F_2 transversely positioned as in the Young's slits experiment.

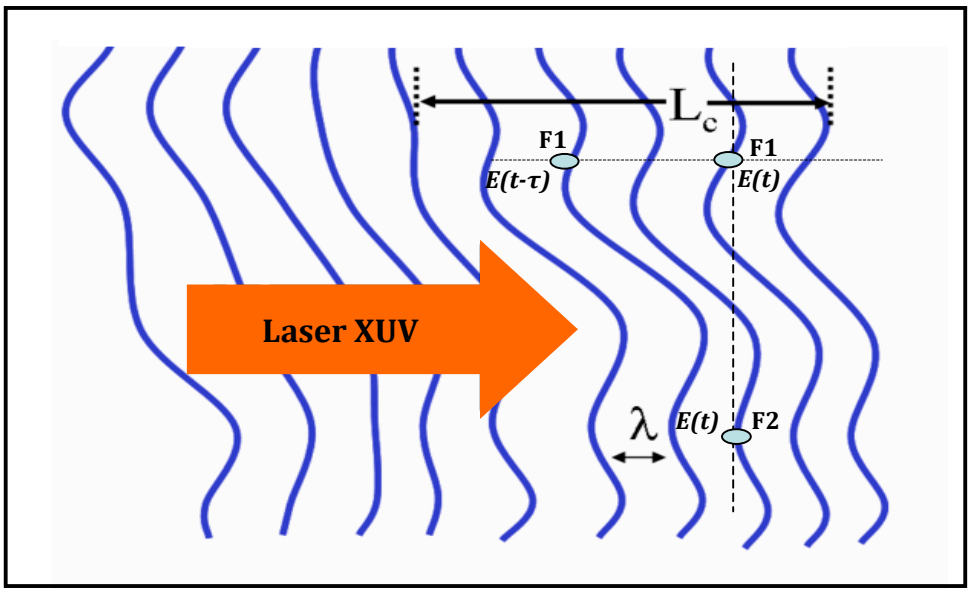

Figure 1-7: Propagation of the wave front of an electromagnetic wave passing through the two points F_1 and F_2 at the same time t.

1.4.1 Temporal coherence

Figure 1-7 illustrates the propagation of the wave front of an electromagnetic wave passing through the point F_1 at two different times, respectively, t and t+τ. Temporal coherence is defined as the correlation between the amplitude of the field at time t and t+τ.

In this case, the coherence function $\Gamma_{11}(\tau)$ is given by:

$$\Gamma_{11}(\tau) = \Gamma(F_1,F_1,\tau) = \left\langle E^*(F_1,t+\tau) \times E(F_1,t) \right\rangle \qquad (1\text{-}32)$$

The degree of coherence is then:

$$\gamma_{11}(\tau) = \frac{\Gamma_{11}(\tau)}{\left\langle I(F_1 = F_2),t \right\rangle} \qquad (1\text{-}33)$$

This quantity can be measured using an interferometer, but requires that the source is monochromatic for the superposition of waves gives rise to an interference phenomenon. In particular, we will highlight the characteristic time τ_c, called coherence time, which is the maximum delay allowed between two wavefronts so that they can produce interference. The longitudinal coherence length is then $l_{ct} = c\tau_c$.

The theorem of Wiener-Khinchin [69], states that the Fourier transform of the coherence function $\Gamma_{11}(\tau)$, corresponds to the power spectral density of the radiation $\rho(\nu)$. It reads:

$$\Gamma_{11}(\tau) = \int_{-\infty}^{+\infty} \rho(\nu) e^{-2\pi i \nu \tau} d\nu \qquad (1\text{-}34)$$

The temporal coherence is thus directly related to the spectral width of the radiation. If we are able to measure experimentally the coherence time, it allows to deduce the spectral width $\Delta\nu$ of the source given by:

$$\Delta\nu = \frac{\kappa}{\pi \cdot \tau_c} \tag{1-35}$$

where κ is a numerical factor, which depends on the actual spectral profile $\rho(\nu)$.

The Wiener-Khintchin theorem as well as relations (1-22) and (1-23) are the core of the interferometric measurements that will be described in chapter 4. As we will see, XUV lasers are characterized by a very good temporal coherence, with a coherence length of the order of several 100µm to 1 mm. Correspondingly, the spectral width is extremely narrow, with a typical bandwidth $\Delta\nu/\nu \sim 10^{-5}$.

1.4.2 Spatial coherence

As already mentioned above, spatial (or transverse) coherence is defined as the correlation between fields at two different points at the same time, such as two spatially separated F_1 and F_2 shown in Figure 1-7.

Back to the Young's slits experiment and using (1-29), we can define the coherence function as follows:

$$\Gamma(F_1, F_2, 0) = \left\langle E^*(F_1, t) \times E(F_2, t) \right\rangle \tag{1-36}$$

A high spatial coherence therefore results in a high degree of correlation between the amplitudes of the fields at the same time. This then results in a high fringe visibility. In the case of an incoherent source observed at a great distance, the spatial coherence function can be calculated by the Van Cittert-Zernicke theorem [70].

Two parameters strongly influence the spatial coherence of a beam: the first is the transverse size of the source (which may vary from one shot to another, especially in the case of XUV lasers); the second is the angle wherein the beam is seen for a given position. The spatial coherence length l_{cs} of a Gaussian beam can be approximated by the expression [34]:

$$l_{cs} = \frac{\lambda L}{a} \tag{1-37}$$

where a is the transverse dimension of the source, and L is the distance between the source and the measuring position.

The spatial coherence of XUV laser beams has been measured by several groups, for all the different types of collisional XUV lasers described in this chapter (see section 1-2). Except for the capillary-discharge XUV laser for which the spatial coherence was reported to be almost complete for the longest plasma lengths [71], the beams of the other types of collisional XUV lasers (OFI, QSS, transient) exhibit a limited spatial coherence. Typically the coherence length is of ~100μm at a distance of 1 meter from the source [72-74].

Several methods were proposed to improve the spatial coherence of XUV laser beams. Until now, the most promising one is the injection of coherent high-order harmonic radiation.

1.4.3 Improved spatial coherence by amplification of harmonics

The technique of seeding the XUV laser plasma with a coherent high-order harmonic pulse is directly analogous to the concept of "oscillator-amplifier". The harmonic pulse acts as the oscillator, and it is injected and amplified in the amplifier plasma column.

Following the limited success of the first attempt at the Rutherford Laboratory in 1995 [76], the first experimental demonstration of strong seeding amplification was achieved at LOA in 2004 [5]. The 25th harmonic of a femtosecond Ti-Sa laser pulse was focused at the entrance plane of an OFI-pumped Kr plasma. A strong amplification of the harmonic signal was observed at the wavelength of the Ni-like Kr 4d-4p line (λ = 32.8 nm). The amplified HHG beam exhibit a smoother spatial intensity distribution and the spatial coherence is observed to be significantly improved [39].

In 2006, the technique of seeding with HHG radiation was extended to a transient pumping XUV laser by Rocca and coll. [57]. The 25th harmonic of a Ti:Sa laser pulse was again used, but seeded in a Ne-like Ti plasma pumped in the transient regime. Amplification of the harmonic pulse was observed at 32.6 nm, the wavelength of the 3p-3d J=0-1 lasing line in Ne-like Ti. More recently seeding was also obtained at shorter wavelength by the same group in Ni-like Mo, Ag [76]. The spatial coherence of the seeded amplified beam for both wavelengths was observed to be almost complete. Finally the shortest wavelength at which seeding with HHG radiation has been achieved until now is 13.2 nm (4d-4p J=0-1, Ni-like Cd) [6].

1.5 Spectral properties of XUV laser

In the last section of this chapter we will discuss the main physical processes involved in the spectral properties of the XUV laser lines.

We first recall the main broadening processes that contribute to the intrinsic (ie. optically-thin) line. Then we will briefly recall how the line is narrowed through amplification.

The intrinsic line profile of the XUV laser line (or of any spectral line) is controlled by different hydrodynamic parameters that characterize the plasma (Te, Ti, Ne ...). As we will see below, both homogeneous broadening (collisional) and inhomogeneous (Doppler) broadenings can contribute to the profile, leading in general to the so-called Voigt profile V(ν), given by the convolution of both effects:

$$V(\nu) = \int_{-\infty}^{+\infty} \phi_H(\nu' - \nu) \times \Phi_{inhom}(\nu') d\nu' \qquad (1\text{-}38)$$

1.5.1 Homogeneous broadening

A number of processes can cause homogeneous broadening of the spectral line profile, as the radiative decay (spontaneous emission) or the effect of elastic or inelastic electron collisions. The effect of electron collisions is usually described in the impact approximation, where the duration of the collision is short compared the transition lifetime.

In this case, the spectral profile of the line of interest is the same for all emitting ions and it can be found that it leads to a Lorentz function type [77]:

$$\phi_H(\nu) = \frac{2}{\pi \times \Delta\nu_H} \frac{1}{1 + \frac{4(\nu - \nu_0)^2}{\Delta\nu_H^2}} \qquad (1\text{-}39)$$

Where ν_0 is the center frequency of the line and $\Delta\nu_H$ is the full-width at half maximum.

In general the linewidth $\Delta\nu_H$ is expressed in terms of the sum of the rates of radiative and collisional decay of the upper level i and lower level j of the transition:

$$\Delta\nu_H = \sum_k (A_{ik} + A_{jk}) \qquad (1\text{-}40)$$

where the sum over k includes all levels connected to levels i and j by radiative or collisional deexcitation.

1.5.2 Inhomogeneous broadening

The inhomogeneous broadening of the spectral profile of the emission line is due to the existence of emitting ions at different center frequencies, caused by Doppler or Stark effects. The Stark effect is the perturbation of the emitter energy levels due to the average microfield from the neighboring ions. This effect is negligible in the case of collisional XUV lasers because it becomes significant only at very high density (typically greater than 10^{21} cm^{-3}).

The Doppler effect is due to the thermal motion of the ions that changes their apparent emission frequency in the laboratory frame. If the velocity distribution is Maxwellian, this leads to a Gaussian spectral profile given by the following equation:

$$\phi_D(\nu) = \frac{2\sqrt{\ln 2}}{\sqrt{\pi \times \Delta\nu_D}} \exp\left(\frac{-4\ln 2(\nu - \nu_0)^2}{(\Delta\nu_D)^2}\right) \quad (1\text{-}41)$$

The FWHM Doppler width $\Delta\nu_D$ is given by:

$$\Delta\nu_D = 2\sqrt{\ln 2}\nu_0\sqrt{\frac{2kT_i}{mc^2}} \quad (1\text{-}42)$$

where m is the mass of the ion emitter and k is the Boltzmann constant. It is the plasma ion temperature T_i that determines the width $\Delta\nu_D$. Numerically $\Delta\nu_D$ can be written as follows:

$$\Delta\nu_D \approx 7.715 \times 10^{-5}\nu_0\left(\frac{T_i}{m}\right)^{\frac{1}{2}} \quad (1\text{-}43)$$

where T_i is expressed in eV, and m in atomic mass unit (amu).

1.5.3 Effect of amplification and saturation on the spectral profile

The intrinsic profile of the lasing line is then modified while radiation propagates along the plasma and is amplified. At the output of the lasing medium the XUV laser line is narrowed, as illustrated in Figure 1-8. The relation between the amplified and the intrinsic linewidths is in general complex, but can be evaluated in a simple case, below saturation, using the solution of the 1D-radiative transfer equation described in section 1.3. This aspect will be discussed in more details in chapter 2, where we will present the results of numerical simulations that we have performed, taking into account saturation effects.

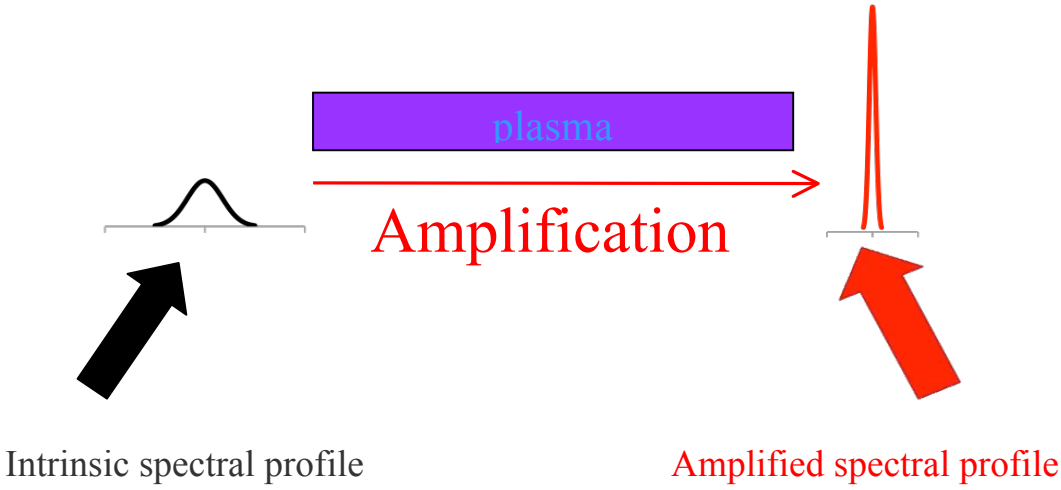

Figure.1-8: Narrowing of the XUV laser spectral profile in the plasma amplifier

The FWHM spectral width $\Delta\nu_{ASE}$ of the amplified line is defined as:

$$I(\nu) = I\left(\nu_0 \pm \frac{\Delta\nu_{ASE}}{2}\right) = \frac{1}{2} I(\nu_0) \qquad (1\text{-}44)$$

By replacing the intensity I(ν) by its expression (1-12) and assuming a large (but non-saturated) gain-length G_0L, we find:

$$\Delta\nu_{ASE} = \frac{\Delta\nu_{sp}}{\sqrt{G_0 L}} \qquad (1\text{-}45)$$

Where $\Delta\nu_{sp}$ denotes the FWHM width of the intrinsic (spontaneous emission) line. So, below saturation the XUV laser line is narrowed by a factor that is inversely proportional to the square root of the gain-length product. When amplification enters the saturation regime the evolution of the spectral profile is modified in a way that depends on the nature of the intrinsic profile (i.e homogeneous, inhomogeneous or a combination of both). This aspect will be discussed in more detail in chapter 2, and illustrated by detailed numerical simulations based on a radiative transfer model developed in [77].

1.5.4 Relationship between linewidth and minimum pulse duration

In section 1.4 we have recalled that, following the Wiener-Khintchin theorem, the spectral profile of a source is linked to its autocorrelation function by a Fourier-transform, so that the coherence time and the frequency spectral width are Fourier transform pairs (see equations (1-34) and (1-35) above).

For a fully coherent pulse (γ_{11}=1), the spectral evolution of the field amplitude is given by the Fourier transform of the field amplitude in the spectral domain. Hence the FWHM duration of such a pulse is the minimum that can be reached, it is called the Fourier-transform limit τ_{FL}. The Fourier-transform limit τ_{FL} and the spectral linewidth $\Delta\nu$ are thus inversely related. The exact relationship depends on the shape of the spectral profile (or of the temporal profile). Here we derive this relation in two simple, usual cases:

a)、Exponential temporal pulse profile

Assuming an electromagnetic field with an amplitude varying in time as:

$t<0$ $\quad E(t) = 0$

$t\geq 0$ $\quad E(t) = E_0 \exp(i\omega_0 t)\exp[-(\ln 2)\frac{t}{\tau}]$ (1-46)

The intensity of this field is then:

$$I(t) = |E(t)|^2 = E(t) \times E^*(t) = |E_0|^2 \exp[-2(\ln 2)\frac{t}{\tau}] \quad (1\text{-}47)$$

The FWHM temporal duration of the pulse intensity is thus $\tau/2$.

The field amplitude in the spectral domain is the Fourier transform of the amplitude in the time domain:

$$E(\omega) = FT[E(t)] = \frac{1}{\sqrt{2\pi}} \int_0^\infty E(t)\exp(-i\omega t)dt \quad (1\text{-}48)$$

From [1-28] we thus find:

$$E(\omega) = \frac{E_0}{\sqrt{2\pi}} \frac{1}{\frac{(\ln 2)}{\tau} + i(\omega - \omega_0)} \quad (1\text{-}49)$$

The corresponding intensity in the frequency domain is then:

$$I(\omega) = |E(\omega)|^2 = E(\omega) \times E^*(\omega) = \frac{|E_0|^2}{2\pi} \frac{1}{[\frac{(\ln 2)}{\tau}]^2 + (\omega - \omega_0)^2} \qquad (1\text{-}50)$$

The spectral intensity profile is a Lorentzian with a FWHM width Δω given by:

$$\Delta\omega = \frac{2 \cdot Ln2}{\tau} \qquad (1\text{-}51)$$

b)、Gaussian temporal pulse profile

We now assume that the temporal profile of the field amplitude is Gaussian, with a FWHM 2τ:

$$E(t) = E_0 \exp(i\omega_0 t) \exp[-(\ln 2)\frac{t^2}{\tau^2}] \qquad (1\text{-}52)$$

The corresponding field intensity can be written as

$$I(t) = |E(t)|^2 = E(t) \times E^*(t) = E_0^2 \exp[-2(\ln 2)\frac{t^2}{\tau^2}] \qquad (1\text{-}53)$$

where the FWHM duration of the intensity pulse is $\sqrt{2}\tau$.

In the spectral domain the field amplitude is

$$E(\omega) = FT[E(t)] = \frac{1}{\sqrt{2\pi}} \int_{-\infty}^{\infty} E(t) \exp(-i\omega t) dt \qquad (1\text{-}54)$$

$$E(\omega) = \frac{E_0 \tau}{\sqrt{2(\ln 2)}} \exp[-\frac{\tau^2}{4(\ln 2)}(\omega - \omega_0)^2] \qquad (1\text{-}55)$$

where the FWHM spectral width is 4*(ln2)/ τ.

The corresponding field intensity is

$$I(\omega) = |E(\omega)|^2 = E(\omega) \times E^*(\omega) = \frac{E_0^2 \cdot \tau^2}{2(\ln 2)} \exp[-\frac{\tau^2}{2(\ln 2)}(\omega - \omega_0)^2] \qquad (1\text{-}56)$$

The spectral intensity profile is a Gaussian with a FWHM width Δω given by:

$$\Delta\omega = \frac{2 \cdot \sqrt{2} \cdot Ln2}{\tau} \qquad (1\text{-}57)$$

The results above are summarized in Table 1.

	Exponential/Lorentzian	Gaussian/Gaussian
E(t)	τ	2τ
$I(t)=\|E(t)\|^2$	$\tau/2$	$\sqrt{2}\tau$
$E(\omega)=FT[E(t)]$	$2(\log 2)/\tau$	$4(\log 2)/\tau$
$I(\omega)=\|E(\omega)\|^2$	$2(\log 2)/\tau$	$2\sqrt{2}(\log 2)/\tau$

Table 1-1. Temporal and spectral widths (FWHM) of the pulse for two types of temporal profiles

In our experiments we measure the characteristics of the intensity pulse, not the amplitude. We can thus express the relationship between the Fourier-limit pulse duration τ_{FL} and the spectral linewidth $\Delta\nu$ as follows:

Exponential/ Lorentzian:

$$\tau_{FL} = \frac{Ln2}{2\pi\cdot\Delta\nu}$$

$$\text{or } \Delta\nu_{1/2}\cdot\tau_{FL} = \frac{Ln2}{2\pi} = 0.11 \qquad (1\text{-}58)$$

Gaussian/Gaussian:

$$\tau_{FL} = \frac{2Ln2}{\pi\cdot\Delta\nu}$$

$$\text{or} \quad \Delta\nu_{1/2}\cdot\tau_{FL} = \frac{2Ln2}{\pi} = 0.44 \qquad (1\text{-}59)$$

The relations (1-58) and (1-59) will be used in chapter 2 and 4 when discussing the shortest duration that could be reached for XUV lasers.

References

1. M. V Ammosov, N. B Delone, and V P. Krainov, "Tunnel ionization of complex atoms and atomic ions in an electromagnetic field," Soy. Phys. JETP, 64, 1191-1196 (1986);

2. Anne L'Huillier and Ph. Balcou, "High-Order Harmonic Generation in Rare Gases with a 1-ps 1053-nm Laser", Phys.Rev. Lett, Vol 70, p. 774 (1993).

3. A. L'Huillier, L. A. Lompré, G. Mainfray and C. Manus, *"High order harmonic generation in rare gases, Atoms in Intense Laser Fields",*Boston Academic Press (1992);

4. M. Schnürer, Z. Cheng, M. Hentschel, G. Tempea, P. Kálmán, T. Brabec, and F. Krausz, "Absorption-Limited Generation of Coherent Ultrashort Soft-X-Ray Pulses" , Phys. Rev. Lett., Vol 83, p. 722, (1999);

5. Ph. Zeitoun, G. Faivre, S. Sebban, T. Mocek, A. Hallou, M. Fajardo, D. Aubert, Ph. Balcou, F. Burgy, D. Douillet, S. Kazamias, G. De Lachèze-Murel, T. Lefrou, S. Le Pape, P. Mercère, H. Merdji, A.S. Morlens, J.P. Rousseau, C. Valentin, "A high-intensity highly coherent soft X-ray femtosecond laser seeded by a high harmonic beam", Nature, Vol 431, p. 426, (2004);

6. F. Pedaci, Y.Wang, M.Berrill, B.Luther, E.Granados and J.J.Rocca, "Highly coherent injection-seeded 13.2 nm tabletop soft x-ray laser", Opt. Lett., Vol 33, p. 491(2008) ;

7. J. P. Goddet, "Etude et développements des sources xuv par injection d'harmoniques" Thèse de doctorat de l'école Polytechnique (2009);

8. Midorikawa, K., Nabekawa, Y., and Suda, A., "XUV multiphoton processes with intense high-order harmonics", Progr. Quant. Electron., 32 (2), 43–88 (2008) ;

9. Toleikis, S., Bornath, T., Döppner, T., Düsterer, S., Fäustlin, R.R., Förster, E., Fortmann, C., Glenzer, S.H., Göde, S., et al., "Probing near-solid density plasmas using soft x-ray scattering", J. Phys. B, 43(19), 194017 (2010) ;

10. Aquila, A., Hunter, M.S., Doak, R.B., Kirian, R. , Fromme, P., White, T. a Andreasson, J., Arnlund, D., Bajt, S., et al., "Time-resolved protein nanocrystallography using an X-ray free-electron laser", Opt. Expr., vol 20, p. 2706-16 (2012) ;

11. Ackermann, W. et al., "Operation of a free-electron laser from the extreme ultraviolet to the water window", Nat. Photon. 1, 336–342 (2007) ;

12. Emma, P., Akre, R., Arthur, J., Bionta, R., Bostedt, C., Bozek, J., Brachmann, A., Bucksbaum, P., Coffee, R., et al., "First lasing and operation of an ångstrom-wavelength free-electron laser", Nat. Photon. 4, 641-647 (2010) ;

13. P. Jaeglé, A. Carillon, P. Dhez, G. Jamelot, A. Sureau, M. Cukier, et al., "Experimental evidence for the possible existence of a stimulated emission in the extreme UV range", Phys. Lett. A, Vol 36, p.167, (1971);

14. L. I. Gudzenko and L. A. Shelepin, "Negative absorption in a nonequilibrium hydrogen plasma," Sov. Phys. JETP, 18, 998 (1964);

15. A. Klisnick, "Amplification de rayonnement X-UV: le schéma par recombinaison dans les ions lithiumoïdes des plasmas créés par laser", Thèse de doctorat de l'université Paris sud (1990);

16. Yutaka Nagata, Katsumi Midorikawa, Shoich Kubodera, Minoru Obara, Hideo Tashiro, and Koichi Toyoda, "Soft-X-Ray Amplification of the Lyman-a Transition by Optical-Field-Induced Ionization", Phys.Rev. Lett., Vol 71, p.3774, (1993) ;

17. D. L. Matthews, P. L. Hagelstein, M. D. Rosen, M. J. Eckart, N. M. Ceglio, A. U. Hazi, H. Medecki, B. J. MacGowan, J. E. Trebes, B. L. Whitten, E. M. Campbell, C. W. Hatcher, A. M. Hawryluk, R. L. Kauffman, L. D. Pleasance, G. Rambach, J. H. Scofield, G. Stone, and T.A.Weaver, "Demonstration of a Soft X-Ray Amplifier", Phys. Rev. Lett., Vol 54, p.110, (1985) ;

18. F Salin, "Etude et réalisation d'une chaine laser femtoseconde. Rôle des phénomènes solitons dans les lasers femtosecondes à dispersion controlée", Thèse de doctorat de l'Université Paris Sud (1987) ;

19. Tang, H., Guilbaud, O., Jamelot, G., Ros, D., Klisnick, A., Joyeux, D., Phalippou, D., et al., "Diagnostics of laser-induced plasma with soft X-ray (13.9 nm) bi-mirror interference microscopy", Appl. Phys. B, 78(7-8), 975–977 (2004);

20. Jorge Filevich, Michael Purvis, Jonathan Grava, Duncan P. Ryan, James Dunn, Stephen J. Moon, Vyacheslav N. Shlyaptsev, Jorge J. Rocca, "Bow shocks formed by plasma collisions in laser irradiated semi-cylindrical cavities", High Energy Density Physics, 5, 276–282 (2009);

21. Courtney A. Brewer, Fernando Brizuela, Przemyslaw Wachulak, Dale H. Martz, Weilun Chao, Erik H. Anderson, David T. Attwood, Alexander V. Vinogradov, Igor A. Artyukov, Alexander G. Ponomareko, Valeriy V. Kondratenko, Mario C. Marconi, Jorge J. Rocca, and Carmen S. Menoni, "Single-shot extreme ultraviolet laser imaging of nanostructures with wavelength resolution", Opt Lett., Vol 33, p. 518(2008);

22. Marconi, M. C., and Wachulak, P. W., "Extreme ultraviolet lithography with table top lasers", Progr. Quant. Electron., 34(4), 173–190. (2010);

23. G.J. Tallents, N. Booth, M.H. Edwards, L.M.R. Gartside, D.S. Whittaker, Z. Zhai, B. Rus, T. Mocek, M. Kozlova, J. Polan, P. Homer, "Measurements of opacity and temperature of warm dense matter heated by focused soft X-ray laser irradiation", High Energy Density Physics, 5, 110–113 (2009);

24. Shin, J.-W., Dong, F., Grisham, M. E., Rocca, J. J. and Bernstein, E. R., "Extreme ultraviolet photoionization of aldoses and ketoses", Chem. Phys. Lett., 506(4-6), 161–166 (2011);

25. Stehle, C., Kozlova, M., Larour, J., Nejdl, J., Champion, N., Barroso, P., Suzuki-Vidal, F., et al., Opt. Comm., "New probing techniques of radiative shocks", 285, 64–69 (2012) ;

26. K. Namikawa, M. Kishimoto, K. Nasu, E. Matsushita, R. Z. Tai, K. Sukegawa, H. Yamatani, H. Hasegawa, M. Nishikino, M. Tanaka, and K. Nagashima, "Direct Observation of the Critical Relaxation of Polarization Clusters in BaTiO3 Using a Pulsed X-Ray Laser Technique", Phys. Rev. Lett., Vol 103, p.197401, (2009)

27. G. J. Tallents, "The physics of soft x-ray lasers pumped by electron collisions in laser plasmas" J. Phys. D: Appl. Phys. Vol 36, p. R259, (2003) ;

28. H. Daido, S. Ninomiya, T. Imani, Y. Okaichi, M. Takagi, R. Kodama, H. Takabe, Y. Kato, F. Koike, J. Nilsen, and K. Murai , "Atomic Number Scaling of the Nickel-Like Soft X-Ray Lasers", J. Mod. Phys. B, vol 11, p. 945, (1997) ;

29. MacGowan B J, Da Silva L B, Fields D J, Keane C J, Koch J A, London R A, Mathews D L, Maxon S, Mrowka S, Osterheld A L, Scofield J H, Shimkaveg G, Trebes J E and Walling R S, "Short wavelength x ray laser research at the Lawrence Livermore National Laboratory",Phys. Fluids B, 4, 2326 (1992);

30. J. A. Koch, B. J. MacGowan, L. B. Da Silva, D. L. Matthews, J. H. Underwood, P. J. Batson, and S. Mrowka, "Observation of Gain-Narrowing and Saturation Behavior in Se X-Ray Laser Line Proliles", Phys. Rev. Lett., Vol 68, p.3291, (1992);

31. B. Rus, A. Carillon, P. Dhez, P. Jaegle, G. Jamelot, A. Klisnick, M. Nantel, and P. Zeitoun, "Efficient, high-brightness soft-x-ray laser at 21.2 nm", Phys. Rev. A, Vol 55, p. 3858, (1997) ;

32. T. Mocek, B. Rus, A. R. Präg, M. Kozlová, G. Jamelot, A. Carillon, and D. Ros, "Beam properties of a deeply saturated, half-cavity zinc soft-x-ray laser", J.O.S.A. B Optical Physics, Vol 20, p.1386-1391, (2003) ;

33. T. Mocek, B. Rus, M. Kozlová, J. Polan, P. Homer, K. Jakubczak, M. Stupka, D. Snopek, J. Nejdl, M.H. Edwards, D.S. Whittaker, G.J. Tallents, P. Mistry, G.J. Pert, N. Booth, Z. Zhai, M. Fajardo, P. Zeitoun, J. Chalupský, V. Hájková, and L. Juha, "Plasma-based X-ray laser at 21 nm for multidisciplinary applications", Eur. Phys. J. D, 54, 439 – 444 (2009);

34. B. Rus, "Pompage collisionnel du zinc néonoïde: laser X à 21.2 nm; Saturation, Polarisation, Cohérence des lasers X-UV", Thèse de Doctorat, Orsay (1995);

35. P. B. Corkum, N. H. Burnett, and F. Brunel, "Above-Threshold Ionization in the Long-Wavelength Limit", Phys. Rev. Lett., Vol 62, p.1259 (1989);

36. B. E. Lemoff, C. P. J. Barty, and S.E. Harris, "Femtosecond-pulse-driven, electron-excited XUV lasers in eight-times-ionized noble gases", Opt. Lett., Vol 19, p. 569 (1994);

37. B. E. Lemoff, G. Y. Yin, C. L. Gordon III, C. P. J. Barty, and S. E. Harris, "Demonstration of a 10-Hz Femtosecond-Pulse-Driven XUV Laser at 41.8 nm in Xe IX", Phys. Rev. Lett., Vol 74, p.1574, (1995) ;

38. S. Sebban, T. Mocek, D. Ros, L. Upcraft, Ph. Balcou, R. Haroutunian, G. Grillon, B. Rus, A. Klisnick, A. Carillon, G. Jamelot, C. Valentin, A. Rousse, J. P. Rousseau, L. Notebaert, M. Pittman, and D. Hulin, "Demonstration of a Ni-Like Kr Optical-Field-Ionization Collisional Soft X-Ray Laser at 32.8 nm", Phys. Rev. Lett., Vol 89, p. 253901 (2002) ;

39. J. Ph. Goddet, S. Sebban, J. Gautier, Ph. Zeitoun, C. Valentin, F. Tissandier, T. Marchenko, G. Lambert, M. Ribières, D. Douillet, T. Lefrou, G. Iaquaniello, F. Burgy, G.

Maynard, B. Cros, B. Robillard, T. Mocek, J. Nejdl, M. Kozlova and K. Jakubczak, "Aberration-free laser beam in the soft x-ray range", Opt. Lett., vol 34, p. 2438(2009);

40. Chen, B.K., Ho, Y.-C., Hung, T.-S., Chang, Y.-L., Chou, M.-C., Chen, S.-Y., Chu, H.-H., Huang, S.-L., Lin, P.-H., et al., "High-brightness optical-field-ionization collisional-excitation extreme-ultraviolet lasing pumped by a 100-TW laser system in an optically preformed plasma waveguide",Appl. Phys. B 106(4), 817-822 (2011);

41. T. Mocek, S. Sebban, I. Bettaibi, L. M. Upcraft, P. Balcou, P. Breger, P. Zeitoun, S. Le pape, D. Ros, A. Klisnick, A. Carillon, G. Jamelot, B. Rus, J. F. Wyart, "Characterization of collisionally pumped optical-field-ionization soft X-ray lasers", Appl. Phys. B 78, 939–944 (2004);

42. F. Tissandier, S. Sebban, M. Ribiere, J. Gautier, Ph. Zeitoun, G. Lambert, A. Barszczak Sardinha, J.-Ph. Goddet, F. Burgy, T. Lefrou, C. Valentin, and A. Rousse, O. Guilbaud and A. Klisnick, J. Nejdl and T. Mocek, G. Maynard, "Observation of spectral gain narrowing in a high-order harmonic seeded soft-x-ray amplifier", PHYSICAL REVIEW A 81, 063833 (2010);

43. J.J. Rocca, V. Shlyaptsev, F.G. Tomasel, O. D. Cortazar, D. Hartshorn, and J. L. A. Chilla, "Demonstration of a Discharge Pumped Table-Top Soft-X-Ray Laser", Phys. Rev. Lett, Vol 73, p. 2192 (1994) ;

44. Aleksandr V Vinogradov and J J Rocca, "Repetitively pulsed X-ray laser operating on the 3p -3s transition of the Ne-like argon in a capillary discharge" Quantum Electronics, 33 (1), p.7-17 (2003);

45. B. R. Benware, C. D. Macchietto, C. H. Moreno, and J. J. Rocca, "Demonstration of a high average power tabletop soft X-ray laser", Phys. Rev. Lett., vol 81, p. 5804, (1998);

46. L. Urbanski, M. C. Marconi, L. M. Meng, M. Berrill, O. Guilbaud, A. Klisnick, and J. J. Rocca, "Spectral linewidth of a Ne-like Ar capillary discharge soft-x-ray laser and its dependence on amplification beyond gain saturation", PHYSICAL REVIEW A 85, 033837 (2012)

47. Y. V. Afanas'ev and V. N. Shlyaptsev, "Formation of a population inversion of transitions in Ne-like ions in steady-state and transient plasmas" Sov. J. Quantum Electron, Vol 19, p.1606, (1989);

48. M. P. Kalachnikov, P. V. Nickles, M. Schnürer, W. Sandner, V. N. Shlyaptsev, C. Danson, D. Neely, E. Wolfrum, J. Zhang, A. Behjat, A. Demir, G. J. Tallents, P. J. Warwick, and C. L. S. Lewis, "Saturated operation of a transient collisional x-ray laser", Phys. Rev. A, Vol 57(6), p.4778-4783, (1998) ;

49. A. Klisnick, P. Zeitoun, D. Ros, A. Carillon, P. Fourcade, S. Hubert, G. Jamelot, C. L. S. Lewis, A. G. Mac Phee, R. M. N. Rourcke, R. Keenan, P. V. Nickles, K. Janulewicz, M. Kalashnikov, J. Warwick, J.-C. Chanteloup, A. Migus, E. Salmon, C. Sauteret, , and J. P. Zou., "Transient pumping of a Ni-like Ag x-ray laser with a subpicosecond pump pulse in a traveling-wave irradiation geometry", JOSA B, Vol 17, p.1093, (2000);

50. R. Keenan, J. Dunn, P. K. Patel, D. F. Price, R. F. Smith, and V. N. Shlyaptsev, "High-Repetition-Rate Grazing-Incidence Pumped X-Ray Laser Operating at 18.9 nm", Phys. Rev. Lett., vol 94, p. 103901(2005) ;

51. F. Lindau, O. Lundh, A. Persson, K. Cassou, S. Kazamias, D. Ros, F. Ple, G. Jamelot, A. Klisnick, S. de Rossi, D. Joyeux, B. Zielbauer, D. Ursescu, T. Kuhl and C.-G. Wahlstrom, "Quantitative study of 10 Hz operation of a soft x-ray laser — energy stability and target considerations", Opt. Express, vol 15, p. 9486(2007);

52. Zielbauer, B., Zimmer, D., Habib, J., Guilbaud, O., Kazamias, S., Pittman, M., & Ros, D., "Stable and fully controlled long-time operation of a soft X-ray laser for user application experiments", Appl. Phys. B, 100(4), 731–736 (2010);

53. Staub, F., Imesch, C., Bleiner, D. and Balmer, J. E., "Soft-X-ray lasing in nickel-like barium at 9.2 nm using the grazing-incidence scheme", Opt. Comm., 285, 2118–2121 (2012) ;

54. D. Alessi, B. M. Luther, Y. Wang, M. A. Larotonda, M. Berrill, and J. J. Rocca, "High repetition rate operation of saturated tabletop soft x-ray lasers in transitions of neon-like ions near 30 nm", Opt. Express, vol 13, p. 2093(2005);

55. Alessi, D., Wang, Y., Luther, B., Yin, L., Martz, D., Woolston, M., Liu, Y., Berrill, M., and Rocca, J., "Efficient Excitation of Gain-Saturated Sub-9-nm-Wavelength Tabletop Soft-X-Ray Lasers and Lasing Down to 7.36 nm", Phys. Rev. X 1(2), 021023 (2011);

56. Y. Wang, E. Granados, M. A. Larotonda, M. Berrill, B. M. Luther, D. Patel, C. S. Menoni, and J. J. Rocca "High-Brightness Injection-Seeded Soft-X-Ray-Laser Amplifier Using a Solid Target" Phys. Rev. Lett., vol 97, p. 123901 (2006) ;

57. M. Berrill, Mark Berrill, David Alessi, Yong Wang, Scott R. Domingue, Dale H. Martz, Brad M. Luther, Yanwei Liu and Jorge J. Rocca, "Improved beam characteristics of solid-target soft x-ray laser amplifiers by injection seeding with high harmonic pulses", Optics Letters, vol 35, p. 2317 (2010) ;

58. J. Nilsen, Y.Li, J. Dunn, T.W. Barbee, Jr., and A.L. Osterheld. "Modeling and demonstration of a saturated Ni-like Mo X-ray laser", 7th international Conference on X-ray lasers, Saint-Malo, France, (2000) ;

59. S J Wang, Q L Dong, J Zhao, L Zhang1 and J Zhang, "The lasing temporal characteristics of Ni-like Mo x-ray lasers at 18.9 nm driven by a grazing incidence pumping scheme", Journal of Physics: Conference Series 112, 042055 (2008);

60. S. Kazamias, K. Cassou, D. Ros, F. Plé, G. Jamelot, and A. Klisnick, and et al., "Characterization of a transient collisional Ni-like molybdenum soft-x-ray laser pumped in grazing incidence", PHYSICAL REVIEW A 77, 033812 (2008);

61. R. Keenan, J. Dunn, V. N. Shlyaptsev, R. F. Smith, P. K. Patel, D. F. Price, "Efficient Pumping Schemes for High Average Brightness Collisional X-ray Lasers", SPIE, San Diego, (2003);

62. Y. ochi, T. Kawachi, N. hasegawa, A. sasaki, K. nagashima, K. sukegawa, M. kishimoto, M. tanaka, M. nishikino, M. kado, "Measurement of temporal durations of transient collisional excitation X-ray lasers", Appl. Phys. B 78, 961–963 (2004);

63. J. Habib, " Etude et développement d'un laser XUV à haute cadence pour la station LASERIX. Application à la radiobiologie ", Thèse de doctorat, Orsay, (2009);

64. John Dawson and Carl Oberman, "HighFrequency Conductivity and the Emission and Absorption Coefficients of a Fully Ionized Plasma", Phys. Fluids, 5,517, (1962);

65. Tudor Wyatt Johnston and John M. Dawson, "Correct values for highfrequency power absorption by inverse bremsstrahlung in plasmas", Phys. Fluids, 16, 722, (1973);

66. Le Pape, S. and Zeitoun, P., "Modeling of the influence of the driving laser wavelength on the beam quality of transiently pumped X-ray lasers", Opt Comm, 219(1-6), 323–333(2003);

67. Gary J. Linford, Eugene R. Peressini, Walter R. Sooy, and Mary L. Spaeth, "Very Long Lasers", Appl. Opt. 13, p. 379, (1974);

68. L. Mandel, E.Wolf, "Optical coherence and quantum optics", Cambridge university press, Cambridge, UK, (1995);

69. B. W.Shore, "The theory of coherent atomic excitation", Wiley, Vol 1 and 2, New York, (1990);

70. M. Born and E. Wolf, "Principles of Optics", Cambridge university press, Oxford, (1984);

71. Y. Liu, M. Seminario, F. G. Tomasel, C. Chang, J. J. Rocca, and D. T. Attwood, "Achievement of essentially full spatial coherence in a high-average-power soft-x-ray laser", Phys Rev A 63, 033802 (2001);

72. P. Lu, E. Fill, Y. Li, J. Maruhn, and G. Pretzler, "Spatial coherence of prepulse-induced neonlike x-ray lasers", Physical Review A 58, 628 (1998);

73. H. Tang et al., "Spatial Coherence Measurement of 13.9 nm Ni-like Ag Soft X-Ray Laser Pumped by a 1.5 ps, 20 J Laser", Jpn. J. Appl. Phys.,vol 42, p. 443-448, (2003);

74. Y. Liu, Y. Wang, M. A. Larotonda, B.M. Luther, J.J. Rocca and D.T. Attwood, "Spatial coherence measurements of a 13.2 nm transient nickel-like cadmium soft X-ray laser pumped at grazing incidence", Optics Express, vol 14, p. 12872 (2006);

75. T. Ditmire, M. H. R. Hutchinson, M. H. Key, C. L. S. Lewis, A. MacPhee, I. Mercer, D. Neely, M. D. Perry, R. A. Smith, J. S. Wark,,and M. Zepf, "Amplification of xuv harmonic radiation in a gallium amplifier", Phys Rev A 51, R4337 (1995);

76. Y. Wang, E. Granados, F. Pedaci, D. Alessi, B. Luther, M. Berrill, and J.J. Rocca, "Phase-coherent, injection-seeded, table-top soft-X-ray lasers at 18.9 nm and 13.9 nm", Nature Photonics 2, 94 (2008);

77. Jeffrey A. Koch, Brian J. MacGowan, Luiz B.Da Silva, Dennis L. Matthews, James H. Underwood, Philip J. Batson, Richard W. Lee, Richard A. London, and Stan Mrowka,

"Experimental and theoretical investigation of neonlike selenium x-ra3t laser spectral linewidths and their variation with amplification", Physical Review A 50, 1877 (1994).

Chapter 2: Numerical simulations

2.1 Introduction

In this chapter we will present numerical simulations that we have performed to investigate the behaviour of the spectral profile of the XUV laser line while it is amplified and saturation is reached. Our simulations are based on a 1D-radiative transfer code, developed by O. Guilbaud, which was described in his thesis [1]. This code calculates the spectral distribution of intensity of the amplified radiation, taking the intrinsic linewidth as an input data. We have used the results of calculations of intrinsic profile made by D. Benredjem (LAC, Orsay) and A. Calisti (PIIM, Marseille), using the PPP code. This code calculates the intrinsic line profile of the considered transition for given values of plasma density and temperatures (ionic and electronic).

The main purpose of this chapter is to illustrate the different spectral behaviours that can apply to XUV laser lines, when the local plasma conditions in the gain zone are varied. The calculations were done for the Ni-like Mo 4p-4d line at 18.9 nm, but the qualitative behaviour discussed below would also apply for other elements and wavelengths.

The second purpose of the study is to investigate how the shape of the XUV laser line is modified while it is amplified. We will see that our simulations predict that the shape of the amplified line tends to a Gaussian shape, even though the intrinsic profile is Lorentzian.

Finally we have used the results of our simulations to evaluate the best conditions that would be necessary to achieve a Fourier-limit duration below 1 ps.

2.2 Calculated intrinsic line profile

The PPP line shape code [2] was developed by A. Calisti and collaborators in the PIIM laboratory. It is a multi- electron radiator line broadening code that calculates theoretical spectral line profiles for a general emitter in plasma, using data for atomic energy levels and radial matrix elements generated by atomic structure programs. The line profile calculations are done in the framework of the standard theory or if necessary including the effects of ionic perturber dynamics by using the Fluctuation Frequency Model [3]. However for the calculations presented below it has been checked that the Stark effect associated with the ion microfield has a negligible contribution to the line profile.

The PPP code was used to calculate the intrinsic spectral profile of the 4d-4p J 0-1 line in Ni-like Mo over an extended range of plasma temperature and density. This range was chosen to cover the wide variety of plasma conditions over which population inversions by

collisional excitation pumping can be achieved in Ni-like Mo [4]. In particular two different ionic temperatures were chosen as being representative of two different pumping regimes:

- kT_i = 20 eV is representative of the transient pumping regime presented in Chapter 1. In this regime the heating of free electrons is very rapid (few picoseconds) and does not allow a significant collisional equilibriation with the cold ions. As a result the ionic temperature is much lower than the electron temperature at the time when collisional excitation pumping occurs (~at the peak of electron temperature).

- kT_i = 200 eV is representative of the quasi-steady state (QSS) pumping regime, also presented in Chapter 1. In this case, the timescale for heating the free electrons by the pump laser is longer (few 100 ps), allowing ions to reach a higher temperature at the time when collisional pumping is achieved.

For these two ionic temperatures, the electron density was varied between 5×10^{19} and 8×10^{20} cm^{-3}, whereas the electron temperature was varied between 200 and 700 eV.

Figure 2-1 shows the overall linewidth (i.e. including both homogeneous and inhomogeneous broadening contributions) calculated from the PPP code simulations over the above parameter range. The FWHM linewidth was inferred from the calculated line profile by first fitting it with a Voigt function. The linewidth is plotted as a function of the electron density Ne. For the two considered ionic temperatures Ti, only the results corresponding to the lowest (200 eV) and highest (700 eV) electron temperatures T_e are shown. Finally the Doppler contribution for each ionic temperature is shown by the horizontal broken-line curves.

Several general remarks can be made from the results of Figure 2-1:

- The calculated intrinsic linewidth varies from 7 to 65 mÅ over the investigated range, thus illustrating the high potential of varying the local plasma parameters to enlarge the bandwidth of the XUV laser line.

- The relative contribution of the Doppler broadening to the overall linewidth strongly depends on the plasma parameters, but also on the pumping regime (or Ti). The Doppler contribution becomes dominant only at low Ne (~10^{19} cm^{-3}). On the other hand this contribution becomes very small at high Ne (~8.10^{20} cm^{-3}) and low Ti (20 eV). When increasing the electron density the intrinsic profile will thus gradually evolve from a (mostly) inhomogeneous profile to a (mostly) homogeneous profile.

We have thus used the results of figure 1 to investigate the behaviour of the amplified spectral profile in these different cases.

In order to extract the homogeneous component $\Delta\lambda_H$ from the calculated overall linewidth $\Delta\lambda_{tot}$ for a given Doppler component $\Delta\lambda_D$ we have used the following formula [5], which gives a good approximation for a Voigt profile:

$$\Delta\lambda_{tot} = \frac{1}{2}\Delta\lambda_H + \left(\frac{1}{4}\Delta\lambda_H^2 + \Delta\lambda_D^2\right)^{\frac{1}{2}} \qquad (2.5)$$

with $\Delta\lambda = \Delta\nu.c/\nu^2$

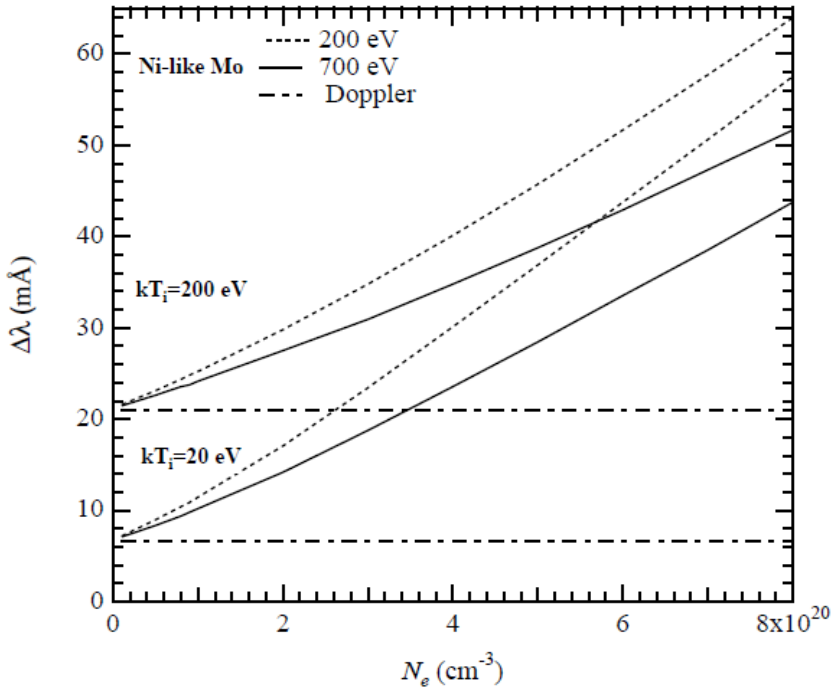

Figure 2-1. Overall intrinsic spectral width calculated with the PPP code as a function of Ne, Te and Ti for the 4d-4p (J = 0 -1) line in Ni-like Mo. The Doppler width is also shown for the two considered ionic temperatures.

2.3 Calculations of amplified line profile

The intrinsic linewidths calculated above were fed into a 1D-radiative transfer code, which calculates the frequency-resolved intensity of the lasing line, as a function of the amplification length. The code was developed by O. Guilbaud (LPGP, Orsay) several years ago [1], following the model discussed by Koch [6] and described in chapter 1.

In this model, the spectral intensity I(ν, z) of the lasing line at the position z along the amplifying plasma column is calculated from the 1D-radiative transfer equation:

$$\frac{dI(v,z)}{dz} = \frac{J_0}{V(v_0)}\left(1+\frac{g_0 I(v,z)}{J_0}\right)\times\int_0^{\infty}\frac{\varphi_D(u)\varphi_H(v,u)du}{1+\frac{1}{I_{sat}}\int_0^{\infty} I(v',z)\varphi_H(v',u)dv'} \qquad (2.6)$$

In this equation J_0 and g_0 are the emissivity and small-signal gain coefficient evaluated at line center. I_{sat} is the spectral saturation intensity, ie the saturation intensity per frequency unit. $\phi_D(u)$ is the Doppler Gaussian profile, with width $\Delta\nu_D$; $\phi_H(v,u)$ is the homogeneous Lorentzian profile, with width $\Delta\nu_H$. Finally $V(\nu_0)$ is the Voigt profile evaluated at line center. The analytic expressions for these quantities are as follows:

$$\phi_D(u) = \frac{2\sqrt{\ln 2}}{\sqrt{\pi}\times\Delta\nu_D}\exp\left(\frac{-4\ln 2\left(u-\nu_0\right)^2}{\left(\Delta\nu_D\right)^2}\right) \qquad (2.7)$$

$$\phi_H(v,u) = \frac{2}{\pi\times\Delta\nu_H}\frac{1}{1+\frac{4\left(\nu-u\right)^2}{\Delta\nu_H^2}} \qquad (2.8)$$

$$V(v) = \int_{-\infty}^{+\infty}\phi_D(v'-v)\times\phi_L(v')dv' \qquad (2.9)$$

The model used for our calculations implies that the plasma parameters are constant in time and space, and that the amplification is unidirectional.

In the numerical code, reduced quantities were defined as follows:

$$I_n(v,z) = I(v,z)/I_{sat}$$

$$J_n = J_0/I_{sat},$$

With these new variables, equation (2.6) can be re-written as:

$$\frac{dI_n(v,z)}{dz} = \frac{J_n}{V(v_0)}\left(1+\frac{g_0 I_n(v,z)}{J_n}\right)\times\int_0^{\infty}\frac{\varphi_D(u)\varphi_H(v,u)du}{1+\int_0^{\infty} I_n(v',z)\varphi_H(v',u)dv'} \qquad (2.10)$$

The typical value of the saturation intensity (integrated over the spectral profile) is 10^{10} W*cm^{-2} [7]. Considering that the typical value for the spectral width is $\Delta\nu\sim10^{11}$-10^{12}Hz, the saturation spectral intensity I_{sat} is 10^{-1} W*cm^{-2}*Hz^{-1}.

The input data are:

- the plasma length L

- the small-signal gain coefficient at line center g_0, here taken at 70 cm^{-1}

- the reduced emissivity, $J_n=J_0/I_{sat}$, typical value is 10^{-6} cm^{-1}.

- the FWHM Doppler width $\Delta\nu_D$ is taken from the results of Figure 1, for the considered set of plasma parameters.

- the FWHM homogeneous width $\Delta\nu_H$ was inferred from the overall linewidth, using equation (2.5)

The output data are:

- the reduced spectral intensity I_n at the output of the plasma of length L;

-the FWHM spectral width of the amplified line at the output of the plasma of length L

By varying the plasma length L we are thus able to investigate the evolution of the spectral width and of the intensity of the XUV laser line when it is amplified and saturation is reached.

Plasma Parameters	Minimum value	Maximum value
Electron density ($10^{20}cm^{-3}$)	0.1	8
Electron temperature (eV)	200	700
Ion temperature (eV)	20	200

Table 2-1. plasma parameters range investigated in the simulation

The line transfer code was run over the plasma parameter range discussed in table 2-1. The results are shown in Figures 2-2 to 2-5 where the overall amplified linewidth is plotted as a function of the plasma amplifier length. up to 7 mm. As it was done for the intrinsic line calculations, the FWHM linewitdh of the calculated amplified spectral profile was inferred by first fitting the calculated profile to a Voigt function $V_a(\nu)$, with width $\Delta\nu_{Va}$ (where the subscript 'a' states for amplified, to discriminate from the intrinsic Voigt profile involved in equation (2.6)).

This Voigt function implies a Gaussian contribution, with width $\Delta\nu_{GV}$, and a Lorentzian contribution, with width $\Delta\nu_{LV}$. The values of $\Delta\nu_{GV}$ and $\Delta\nu_{LV}$ are also plotted in the graphs of

Figures 2-2 to 2-5. Finally, since the amplified profiles were observed to be dominated by the Gaussian contribution, especially for the largest plasma lengths, a Gaussian fit was also performed, and the corresponding width $\Delta\nu_{Ga}$ is also plotted in the graphs.

Figures 2-2 and 2-3 correspond to the low T_i case (20 eV) and to T_e equals to 200 eV and 700 eV respectively. These conditions are relevant to the transient pumping.

Figure 2-4 and 2-5 correspond to the high T_i case (200 eV) and the same T_e values as above. These conditions are relevant to the QSS pumping.

For each figure, each graph corresponds to a different density N_e, as explained in the corresponding captions.

Several general remarks can be made from Figures 2-2 to 2-5:

- In all cases the FWHM linewidth is strongly narrowed in the first 2 mm of amplification, with a reduction of a typically factor 4.

- For plasma length above ~2 mm where the saturation is reached, the linewidth continues to decrease, but much slowly, except for the lower Ne case ($10^{19}cm^{-3}$).

- For the lower N_e case ($10^{19}cm^{-3}$), where the Doppler broadening was noted to be dominant (see figure 2-1), the linewidth decreases to a minimum (typically 1/4 of the intrinsic linewidth) and then rebroadens at saturation.

- For plasma length above ~2 mm, ie when the laser starts to saturate, the profile of the amplified line can be accurately fitted by a Gaussian function, whatever the intrinsic profile is. This can be seen in each graph by noting that the Lorentzian component $\Delta\nu_{LV}$ of the Voigt fit goes to zero, while the Gaussian component $\Delta\nu_{GV}$ of the same Voigt fit approaches the value of the width $\Delta\nu_{Ga}$ of the pure Gaussian fit.

1) T_i=20 eV, T_e=200eV, N_e ~10^{19}cm^{-3}-8×10^{20}cm^{-3}

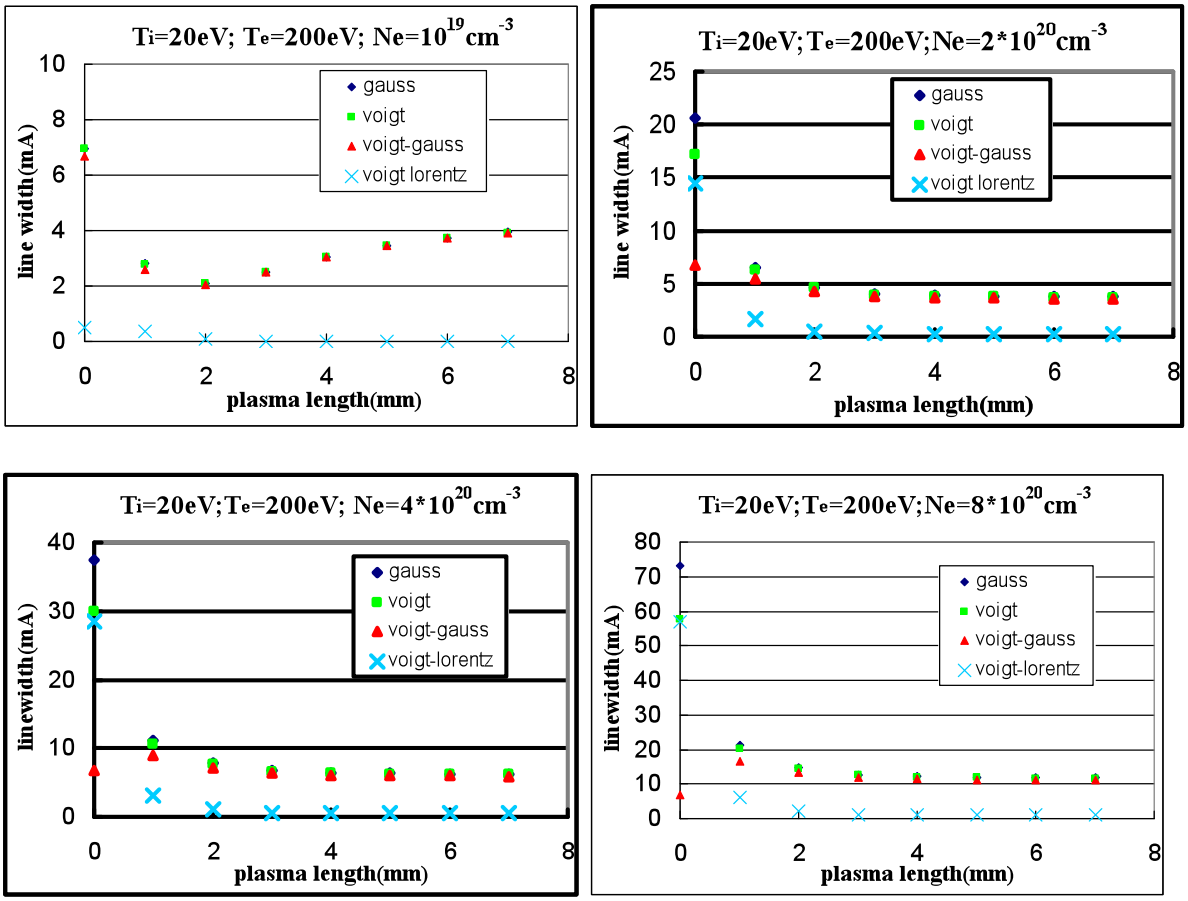

Figure 2-2: Calculated amplified FWHM linewidth as a function of the amplifier length. Plasma parameters: Ti=20eV, Te=200eV and Ne from left to right and up to low: 0.1, 2, 4, 8 * 10^{20} cm^{-3}. Voigt= $\Delta\nu_{Va}$, Voigt-gauss= $\Delta\nu_{GV}$; Voigt-Lorentz=$\Delta\nu_{LV}$; gauss=$\Delta\nu_{Ga}$. See text for definitions of these quantities.

2) T_i=20 eV, T_e=700eV, N_e ~$10^{19}cm^{-3}$-$8\times10^{20}cm^{-3}$

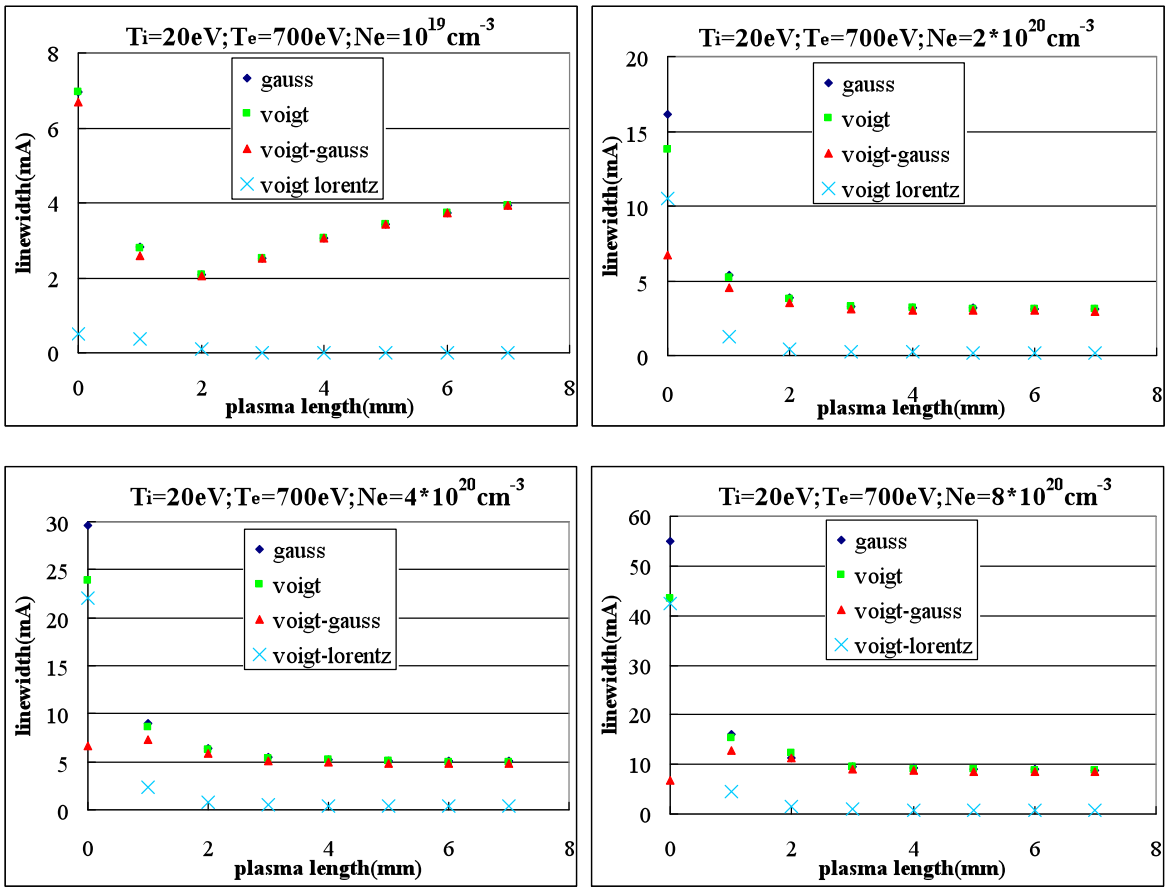

Figure 2-3: Same as figure 2, but Te = 700 eV.

3) T_i=200 eV, T_e=200eV, N_e ~10^{19}cm^{-3}--8×10^{20}cm^{-3}

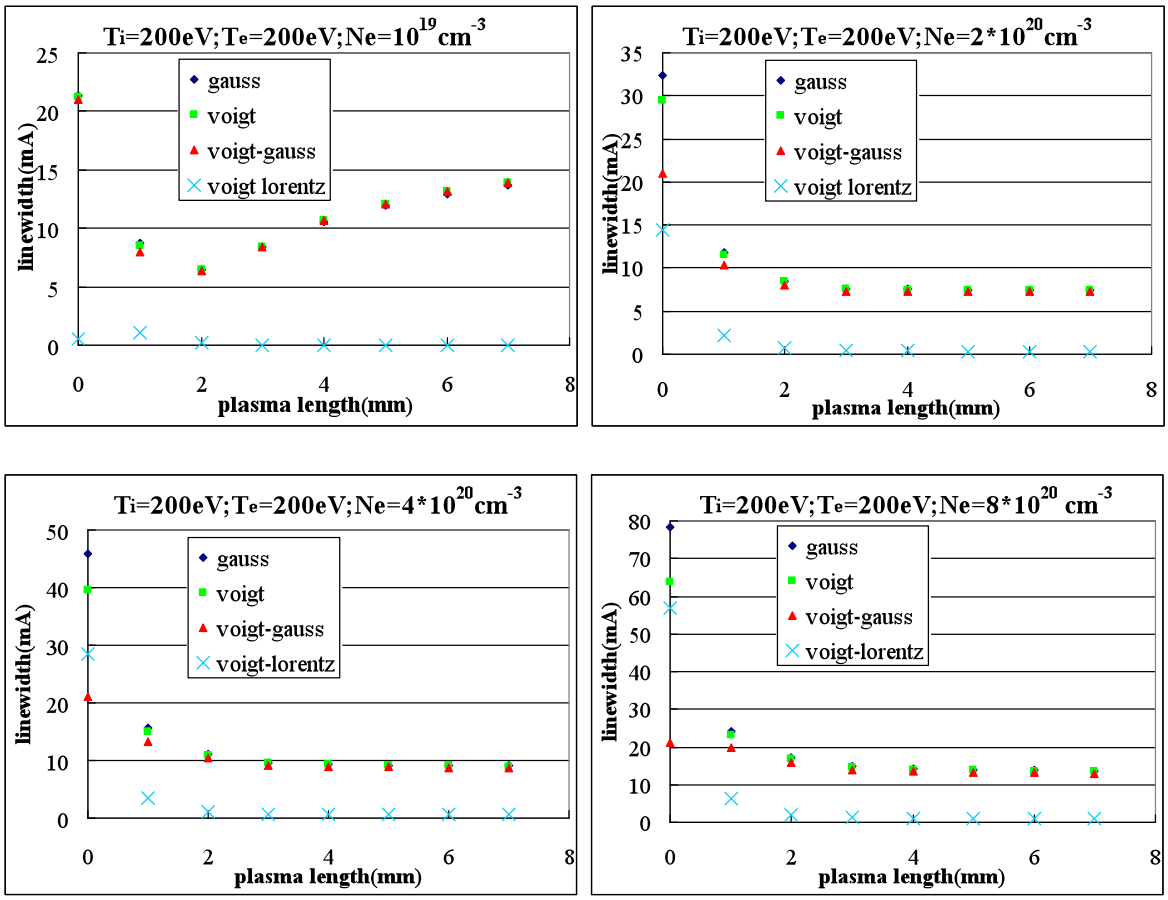

Figure 2-4: Same as figure 2, but Ti=200 eV.

4) T_i=200 eV, T_e=700eV, N_e ~$10^{19}cm^{-3}$--$8\times10^{20}cm^{-3}$

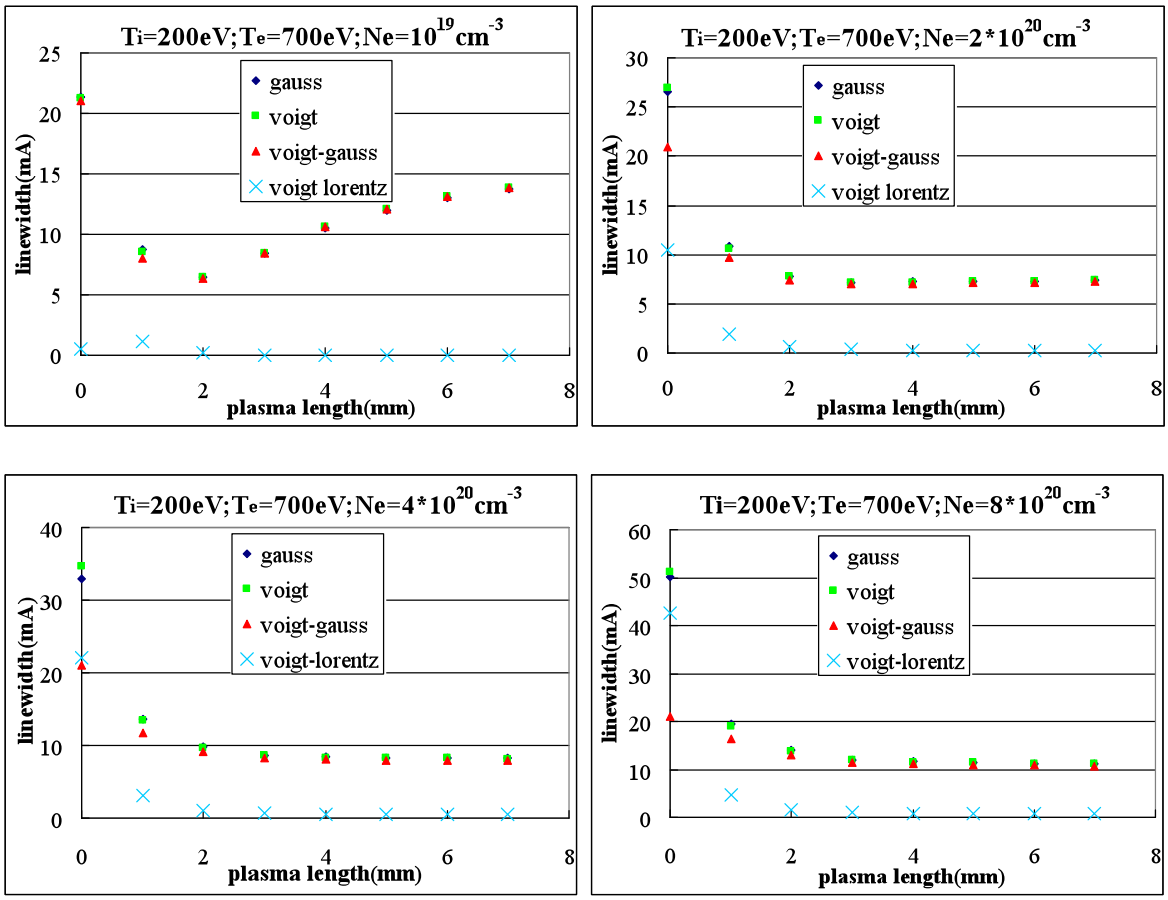

Figure 2-5: Same as figure 2, but Ti=200 eV and Te= 700eV.

2.4 Fourier-transform limit duration

The results presented above can also be used to evaluate the shortest Fourier-transform limit duration τ_{FL} that could be reached while exploring our plasma parameter range.

We compare three different situations, where the intrinsic profile is

- Mixed;

- Extremely homogeneous;

- Extremely inhomogeneous

In all cases we show the results of the radiative transfer calculation in terms of amplified intensity, linewidth and spectral profile as a function of plasma length (Figures 2-6 to 2-11 below).

Finally we calculate in each case the Fourier-transform limit duration using the formula (1-58) derived in chapter 1 for a Gaussian spectral profile:

$$\tau_{FL} = \frac{2Ln2}{\pi \cdot \Delta\nu} = \frac{2 \cdot Ln2}{\pi \cdot c}\frac{\lambda^2}{\Delta\lambda} = 1.55 \cdot 10^{-9}\frac{\lambda^2}{\Delta\lambda} \qquad (2.7)$$

2.4.1 Mixed profile

Plasma parameters: T_i=200eV, T_e=700eV, $N_e = 4\times10^{20}$ cm^{-3},

Intrinsic linewidth:

inhomogeneous component $\Delta\lambda_D$ = 21 mÅ, homogeneous component $\Delta\lambda_H$ = 22 mÅ

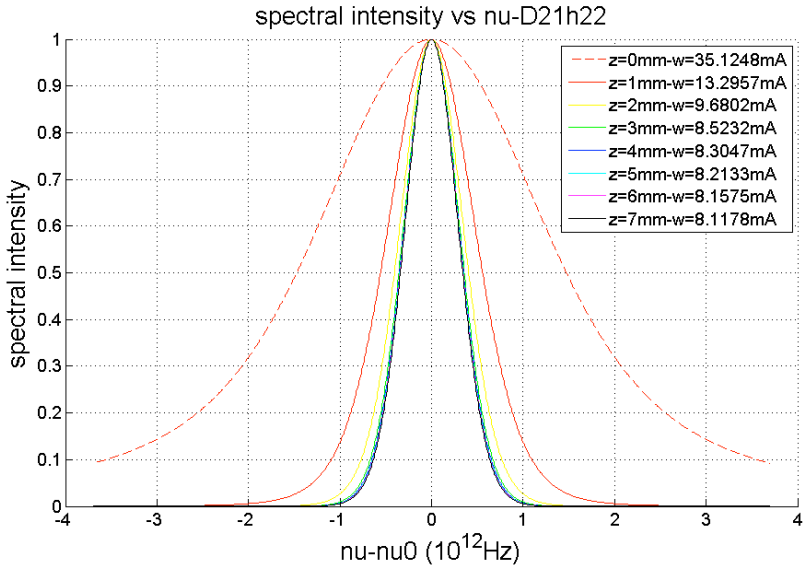

Figure 2-6: case (a) Mixed case (see text). Detail of the evolution the amplified line profile for increasing plasma length (see inset).

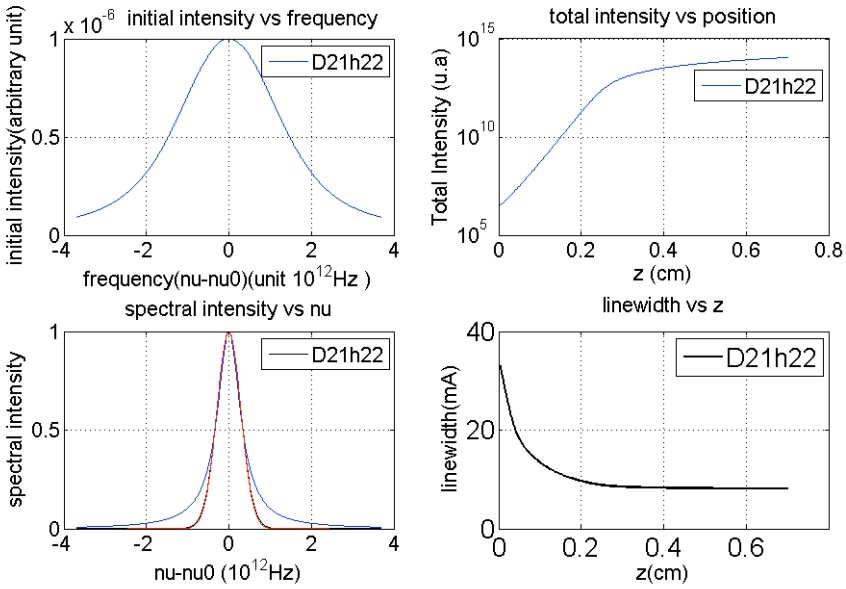

Figure 2-7: case (a) Mixed case (see text). From left to right and up to low: intrinsic profile, "relative" spectrally integrated intensity versus length, amplified profile, amplified linewidth versus length. In the amplified profile versus length (left lower), the black, blue and red lines stand for calculated results and the Lorentz, Gauss fitting with same FWHM separately.

Fourier transform limit duration for L=7 mm: τ_{FL} = **650 fs**

2.4.2 Extremely inhomogeneous profile

Plasma parameters: T_i=200eV, T_e=700eV, $N_e = 0.1\times10^{20}$ cm^{-3},

Intrinsic linewidth:

inhomogeneous component $\Delta\lambda_D$ = 21 mÅ, homogeneous component $\Delta\lambda_H$ = 0.5 mÅ

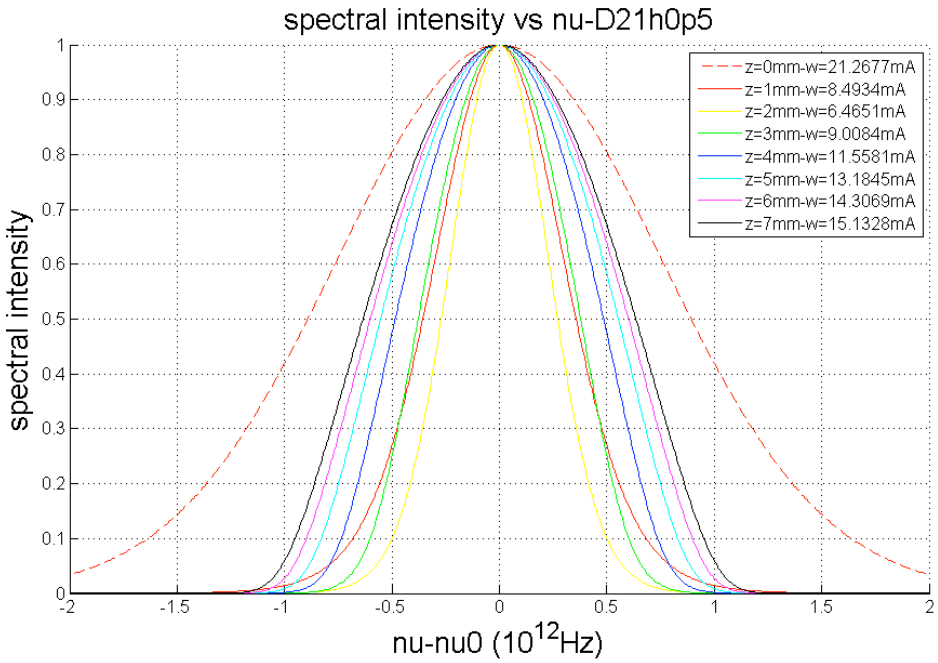

Figure 2-8: same as figure 6, but case (b) extremely inhomogeneous case (see text)

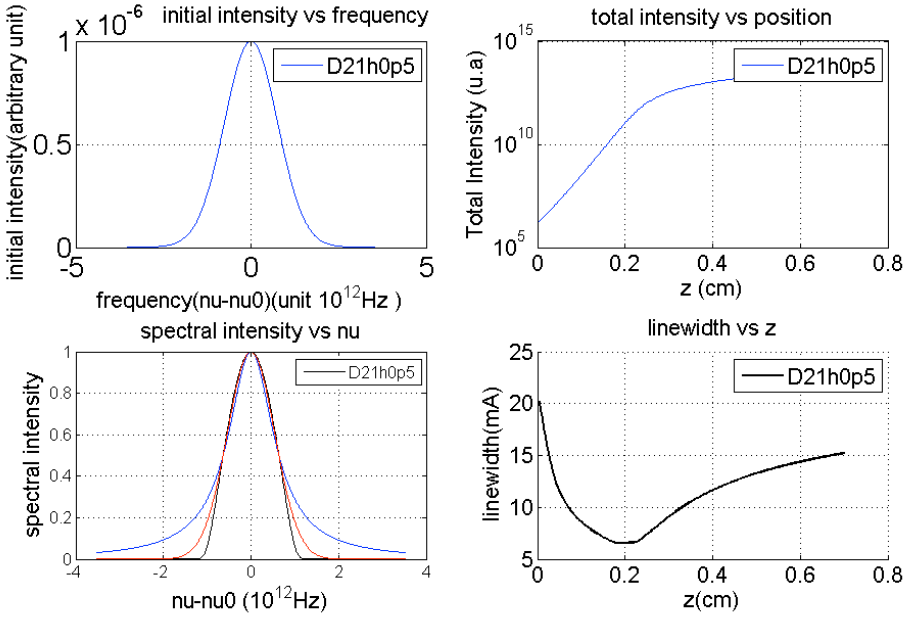

Figure 2-9: same as figure 7, but case (b) extremely inhomogeneous case (see text)

Fourier transform limit duration for L=7 mm: $\boldsymbol{\tau_{FL}}$ **= 380 fs**

2.4.1 Extremely homogeneous profile

Plasma parameters: T_i=20eV, T_e=200eV, $N_e = 8\times10^{20}$ cm^{-3};

Intrinsic linewidth:

inhomogeneous component $\Delta\lambda_D$ = 6.7 mÅ, homogeneous component $\Delta\lambda_H$ = 57 mÅ

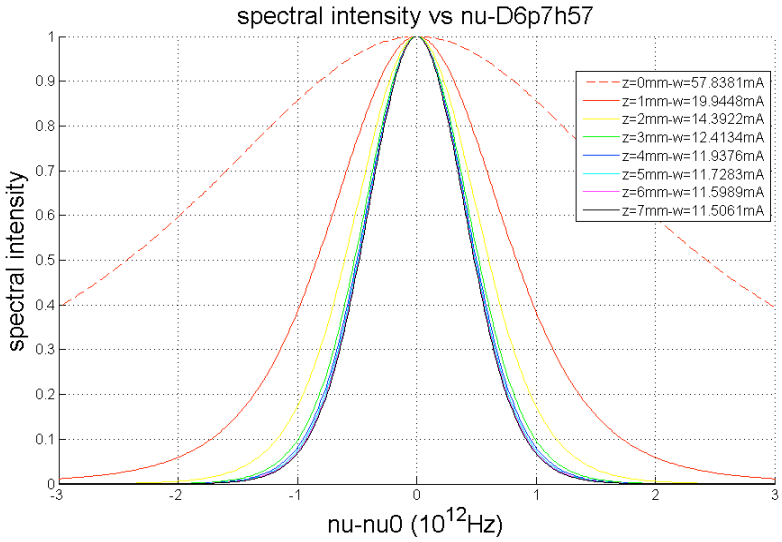

Figure 2-10: same as figure 6, but case (c) extremely homogeneous case (see text)

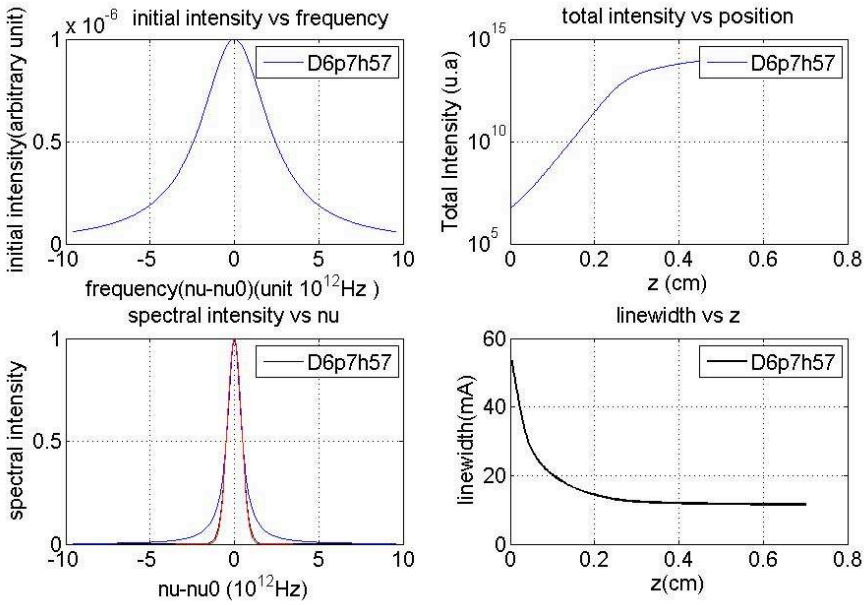

Figure 2-11: same as figure 6, but case (c) extremely homogeneous case (see text)

Fourier transform limit duration for L=7 mm: **τ_{FL} = 450 fs**

The results of the simulation are summarized in table 2-2.

Ion Temperature (eV)	Electron Temperature (eV)	Electron Density (10^{20} cm^{-3})	Calculated spectral width (mÅ)	Calculated Fourier Limit Pulse duration (fs)
200	700	4	8.11	650
200	700	0.1	15.13	380
20	200	8	11.51	450

Table 2-2. summary of calculated results for 3 cases

2.5 Conclusion

In this chapter we have used a 1D-radiative transfer code, as well as the results of detailed intrinsic line profile calculations provided by the PPP code, to investigate in more detail the behaviour of the spectral profile Ni-like Mo 4d-4p J=0-1 line when it is amplified. We have shown that depending on the local plasma parameters in the gain zone, the intrinsic profile strongly changes both in width and in nature (homogeneous/inhomogeneous). Only at very low density the Doppler component is dominant in the overall intrinsic profile. As a result, saturation rebroadening is observed only in this case, whereas in all other cases the linewidth narrows continuously, even after the saturation is reached.

One of the questions that we wanted to address with these calculations was how the shape of the amplified profile was modified. We have shown that even in cases where the initial intrinsic profile is Lorentzian (ie homogeneous), the amplified profile rapidly tends to a Gaussian shape.

Using this result we have calculated the Fourier-transform limit duration that would be reached in three different cases, corresponding to a strongly homogeneous, strongly inhomogeneous, or mixed intrinsic profile. In all cases we find that the Fourier-transform limit duration is below 1 ps. The shortest duration of 380 fs is obtained in the strongly inhomogeneous case, thanks to saturation rebroadening. This result would tend to suggest that low density, high ionic temperature would be more favourable to reach shorter XUV laser duration.

However, a recent study performed by the Marseille group shows that the ionic correlations cannot be ignored in these plasma conditions [8]. The detailed discussion of this effect is beyond the scope of this thesis work, but we point out that one of the main

consequence of ionic correlations will be the homogeneization of the amplified profile, thus preventing any saturation rebroadening.

References

1. O Guilbaud, "Etudes et applications des propriétés de cohérence des lasers X-UV à pompage transitoire", These de Doctorat, Orsay, (2004) ;

2. A. Calisti, F. Khelfaoui, R. Stamm, and B. Talin, "Model for the line shapes of complex ions in hot and dense plasmas", Phys. Rev A 42, 5433 (1990) ;

3. B.Talin, A. Calisti, L. Godbert, and R. Stamm, "Frequency-Auctuation model for line-shape calculations in plasma spectroscopy", Phys. Rev A 51,1918 (1995);

4. Yuelin Li, Joseph Nilsen, James Dunn, and Albert L. Osterheld, "Wavelengths of the Ni-like 4d 1S0– 4p 1P1 x-ray laser line", Phys. Rev. A 58, R2668 (1998) ;

5. Thomas J. Manning, J.D. Winefordner, Byron A. Palmer, Douglas E. Hof, "Observation of line shifts and line profiles in an inductively coupled argon plasma", Acta Part B 45 1031 (1990);

6. Jeffrey A. Koch, Brian J. MacGowan, Luiz B.Da Silva, Dennis L. Matthews, James H. Underwood, Philip J. Batson, Richard W. Lee, Richard A. London, and Stan Mrowka, "Experimental and theoretical investigation of neonlike selenium x-ra3t laser spectral linewidths and their variation with amplification", Physical Review A 50, 1877 (1994);

7. J. Nilsen, Y.Li, J. Dunn, T.W. Barbee, Jr., and A.L. Osterheld, "Modeling and demonstration of a saturated Ni-like Mo X-ray laser", 7th international Conference on X-ray lasers, Saint-Malo, France, (2000) ;

8. A. Calisti et al., "Study of particle correlation effects on line profiles of Ni-like collisional XUV laser amplifier", Proc of 13rd ICXRL Conference (2012).

Chapter 3: Experimental instruments and methods

3.1 Introduction

In chapter 4 we will describe the experimental results that we have obtained during this thesis regarding the characterization of the temporal coherence and spectral width of several collisional XUV lasers, as well as of the duration of the Ni-like Mo transient XUV laser. Here in this chapter we will present the two instruments that we have used to obtain these results: a wavefront division interferometer and a high-resolution X-ray Streak camera. The method used to process the data and to extract the physical quantities from the interferograms will be also discussed in detail.

First we will recall the typical orders of magnitude of the quantities that we want to measure and the different existing instruments available for this purpose.

3.1.1 Temporal coherence and spectral width

As explained in Chapter 1, the temporal coherence and the spectral width of the XUV laser sources that we are interested are Fourier transform pairs. This follows from the Wiener-Khintchine theorem, stating that the Fourier transform of the autocorrelation function of the signal (here electromagnetic field amplitude) is the power spectrum of the signal.

Here we are interested in characterizing both the temporal coherence and the spectral width of XUV lasers. However the direct measurement of this spectral linewidth is out of the reach of existing grating spectrometers. As we will see, the linewidth of XUV lasers is extremely narrow, with a typical bandwidth of $\Delta\lambda/\lambda \sim 1\text{-}4\times10^{-5}$ or less. The first direct measurement of an XUV laser linewidth was reported by Koch et al. in 1994 [1], using a unique grazing incidence grating, flat-field spectrometer [2] specifically designed to reach a resolution as high as $\Delta\lambda/\lambda \sim 3\times10^{-5}$ over a restricted spectral range. This led to the measurement of a 10 mÅ linewidth for the 20.6nm line (3p-3s J=2-1) in Ne-like Se, very close to the resolution limit of the spectrometer. As we will see in chapter 4, some of the XUV laser lines that we have investigated were narrower than that, thus requiring an alternative method of measurement.

The other method consists in measuring the temporal coherence length, by varying the path difference in an interferometric setup. This was first achieved at the Livermore laboratory by a french-US collaboration, using an amplitude-division interferometer in a Michelson configuration [3]. The temporal coherence of the transient Ni-like Pd line (4d-4p J=0-1) line at 14.68 nm was measured and the corresponding spectral bandwidth was inferred as $\Delta\lambda/\lambda \sim 2.3\times10^{-5}$.

In amplitude-division interferometers, the contrast of the interference fringes obtained depends little on the spatial coherence of the radiation and the ratio between the coefficient of the reflection and transmission of the beam splitter. The advantage of this kind of interferometers is that if the configuration of the interferometer is chosen, a path difference between the two beams can be introduced without changing the superposition of the two interfering beams, especially their transverse position. However the accuracy of the measurement is limited by the quality of the multilayer beam splitter used. Although significant progress has been made in the fabrication of these optical elements in the recent years, these devices have several drawbacks that limit their performance level and affect the quality of the results obtained. Firstly, the coefficients of reflection and transmission achieved are relatively low (typically below 20% at 14 nm), leading to energy losses. Second they are difficult to manufacture, relatively fragile, and the cost is also very high. Finally, the use of multi-layer systems implies that the instrument is monochromatic which means that to investigate sources of different wavelengths one has to change all the interfering mirrors. This is why an alternative method was developed by the LIXAM X-ray laser group at the same period, based on a wavefront-division interferometer. This instrument was used for the work described in the thesis. It uses superpolished grazing incidence mirrors in a Fresnel configuration, and will be described in detail below.

3.1.2 Pulse duration

As recalled in chapter 1, the achievement of transient pumping with ultrashort CPA lasers has led to a new generation of XUV lasers delivering much shorter pulse duration than the ones previously obtained in the quasi-steady state regime. The first measurement of the duration of a transient XUV laser was achieved by the LIXAM X-ray laser group at the Rutherford Laboratory (UK) [4]. A pulse duration of 2 ps was reported for the transient Ni-like Ag laser (4d-4p J=0-1) at 13.9nm. This measurement used a fast X-ray Streak camera developed by Axis-Photonique Inc., and it was also used to obtain the results described in this thesis. The principle of operation and characteristics of this instrument will be described below.

Ultrafast X-ray streak cameras are currently the only instruments capable of measuring -in a single-shot- the temporal history of an X-ray pulse on a picosecond timescale. Other methods based on light-field streaking were developed for the attosecond harmonic pulses [5], and more recently extended to the femtosecond regime [6], but it seems difficult to apply them to

picosecond XUV lasers. The picosecond timescale involved would require radiation with centimetric wavelength.

3.2 Wavefront-division interferometer for temporal coherence measurement

3.2.1 Description of the interferometer:

The wavefront-division interferometer we used was specifically designed and built by D. Joyeux and collaborators for the purpose of measuring the temporal coherence of XUV lasers. This interferometer is similar to a usual Fresnel bi-mirror interferometer [7], except that the mirrors have been replaced by dihedrons, as shown in Figure 3-1. The parts of these dihedrons are made from superpolished silica planar blocks [8]. The dihedron mirrors are slightly tilted towards each other, so that after reflection on the dihedrons under 6° grazing incidence, the XUV laser beam is split into two branches that slightly converge towards each other. Interference fringes are formed in the overlapping area. A flat mirror is inserted between the dihedrons and the CCD to redirect and adjust the XUV laser beam towards the CCD camera detector. The CCD is located at 100-150 cm away from the bi-mirror and is tilted at an angle of 35 degrees relative to the propagation axis to stretch the image in the direction across the fringes and improve the spatial resolution. A precision translation stage vertically displaces one of the dihedron mirrors relative to the other inducing a controlled optical path difference between the two interfering beams. This introduces a controlled phase shift on one of the interference field and this leads to a reduction in the interference fringe visibility.

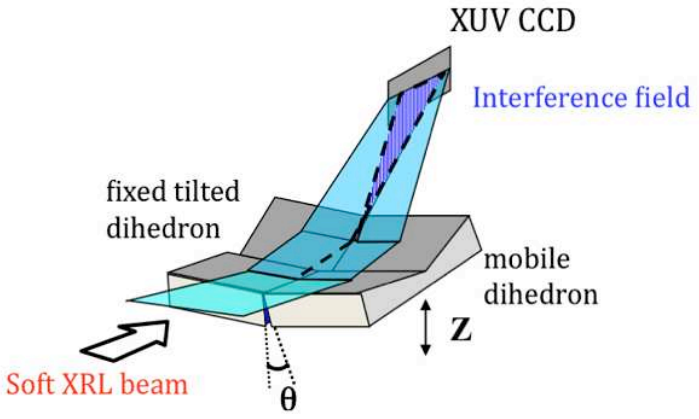

Figure 3-1: Principle of the bi-dihedron interferometerl. θ is the angle of inclination between the surfaces of the mirrors and z the vertical translation of the moblie dihedron.

In order to measure the temporal coherence of the radiation strictly, it is necessary that the path difference variation does not introduce any change in the superposition of secondary beams. Otherwise it will be impossible to determine whether the decrease in the fringe contrast is due to the finite temporal coherence or to the finite spatial coherence or to the limited size of the incident beams. This is why dihedrons were used rather than simple flat mirrors to ensure that the conditions of spatial coherence are kept constant while changing the path difference. Figure 3-2 shows graphically the difference in propagation of the XUV beam after reflection by either a bi-mirror or a bi-dihedron interferometer. The beam is parallel to the edge between the two mirrors with an incidence angle α. One of the mirrors is vertically shifted by z. In the usual Fresnel configuration (Figure 3-2-a), this vertical translation of one mirror introduces a transverse offset between the two secondary beams. In contrast with a bi-dihedron (Figure 3-2-b) the two secondary beams are recombined perfectly after reflection.

(a)

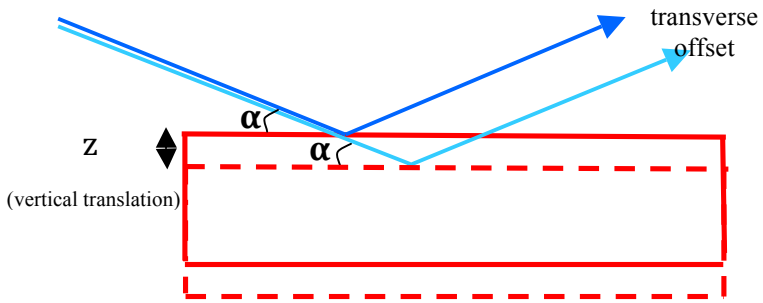

(b)

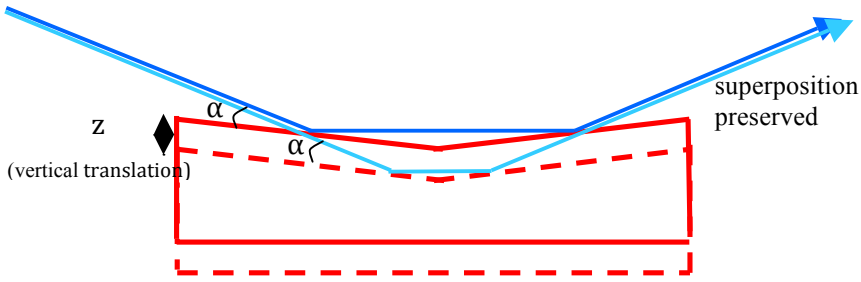

Figure 3-2: Propagation of the incident beam in presence of a path difference z: (a) Fresnel bi-mirror. (b) Bi-dihedron. In (a) the secondary beams undergo a transverse offset, while in (b) their superposition is always maintained.

In Table 3-1 we summarize the characteristics of our bi-dihedron interferometer. The small grazing incidence of the beam (α =6°) allows to provide a good reflectivity of XUV radiation. To facilitate the detection of the fringes, a mirror is placed between the dihedron and the

detector to return the reflected beam along an axis closer to the horizontal as shown in Figure 3-3. The detector used to record the fringes XUV is a back-tinned CCD camera (Andor Technology, 1024x1024 pixels) of 13 microns pixel size. The camera was set about 1.5 m far from the interferometers and tilted by 35 ° to the entrance axis (Figure 3-3-top view) to enlarge the size of the fringe at the detector plane, and thus improve the resolution. The alignment of the interferometer is performed using a Helium-Neon laser beam.

L_o	Length of the dihedron	$80mm$
L_a	Width of the dihedron	$15mm$
θ	Angel between the two mirrors	$0.8mrad$
α	Angle of the incident beem	$6°$
ε	Angle between the two beams reflected by the bi-dihedral	$\varepsilon \approx 4 * \alpha * \theta \approx 0.34mrad$
β	Angle of inclination of the camera 35 °	35°
i	fringe seen by the camera	$i = \frac{\lambda}{\varepsilon \sin \beta}$
z	vertical translation of dihedral mobile	Arbitrary
l	Path difference between the two beams	$l = 2z \sin(2\alpha)$

Table 3-1: Characteristics of the interferometer bi-dihedron.

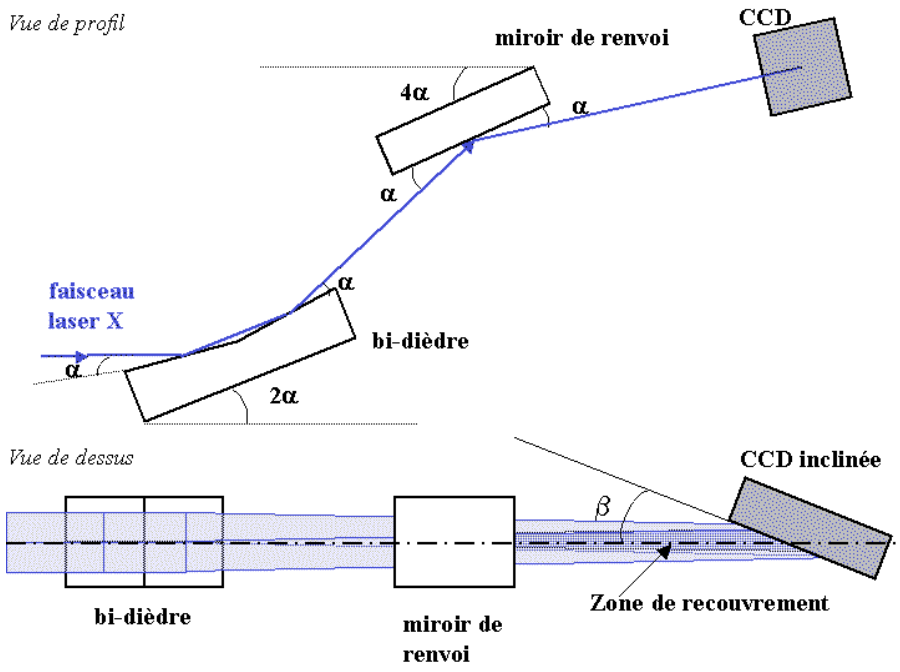

Figure 3-3: side (top) and top (bottom) view of the interferometer (from [9]).

As we have already mentioned, the path difference is introduced between the arms of the interferometer by translating one of the two dihedrons vertically using a high accuracy stepper motor. The corresponding path-difference l is given by the relationship $l = 2z\sin(2\alpha)$, where z is the vertical translation of the mobile dihedron. This creates a delay $\tau = l/c$ between the interfering beams.

The relative angle ε between the two beams after reflection on the dihedons can be calculated as follows:

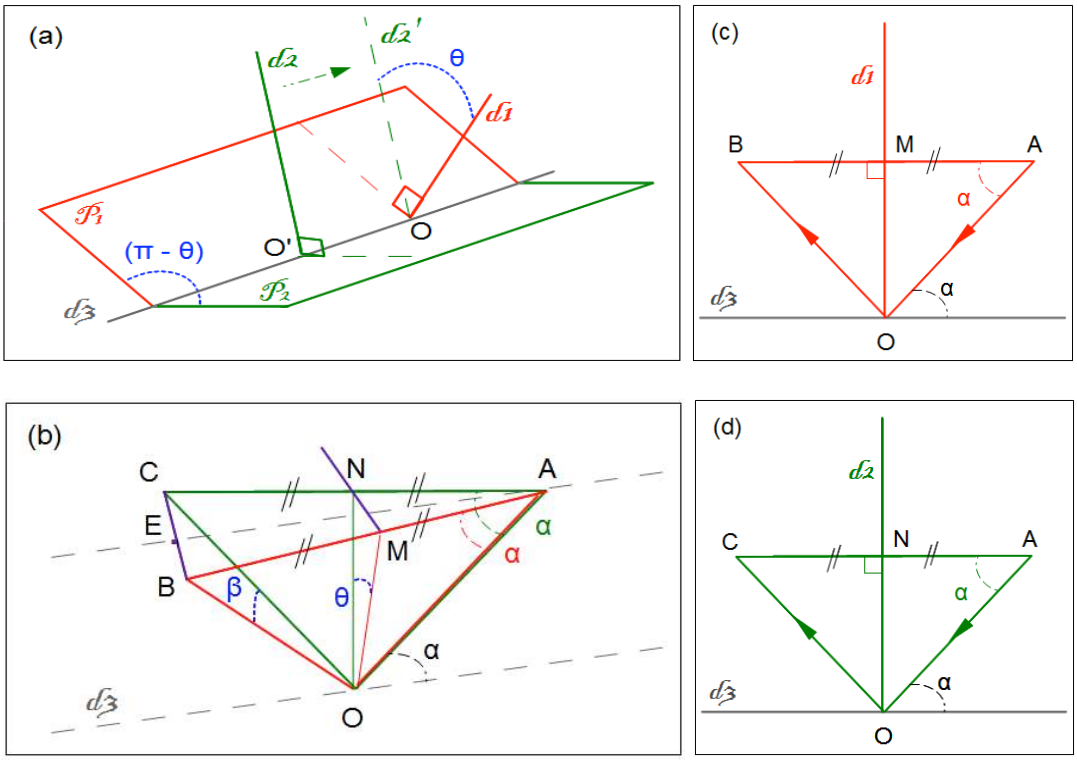

Figure 3-4. Schematic diagram showing the reflected angle

Considering two mirrors P1 and P2, tilt to each other with an angle of θ, d1 and d2 are their normal lines respectively, as shown in figure 3-4(a).

According to the law of reflection, the incident light line, the reflected light line, and the normal line are in the same plane. The beam line is reflected by both mirrors. In order to make it clear, the two reflected beams are represented in figures 3-4(b), (c) and (d).

In figure 3-4(b), (AO) is the incident beam line from point A. (OB) and (OC) are the reflected beams on O by mirrors P1 and P2 respectively. B and C are chosen as we have OB=OC=OA. M and N are the cross points of d1 with [AB] and d2 with [AC] respectively. β is the angle between the two reflected beams (OB) and (OC).

It's easy to know that $OM \perp AB$, $ON \perp AC$, and M, N are the mid-point of [AB] and [AC], The angles $\widehat{OAM} = \widehat{OAN} = \alpha$.

The following calculations to fine the relationship of β with α and θ are based on figure 3-4(b).

The incident angles are : $\widehat{AOM} = \widehat{AON} = \frac{\pi}{2} - \alpha$.

In ΔMON, the angle between the two normal lines $\widehat{MON} = \theta$.

And

$$OM = ON = AO.\sin(\alpha).$$

So

$$MN = 2.OM.\sin\left(\frac{\theta}{2}\right) \Rightarrow MN = 2.AO\sin(\alpha).\sin\left(\frac{\theta}{2}\right)$$

In ΔABC, it is clear that

$$BC = 2.MN \Rightarrow BC = 4.AO.\sin(\alpha).\sin\left(\frac{\theta}{2}\right)$$

In ΔBOC, E is the mid-point of [BC], then

$$\sin\left(\frac{\beta}{2}\right) = \frac{BE}{OB} \Rightarrow \beta = 2\arcsin\left(\frac{BE}{OB}\right) = 2\arcsin\left(\frac{BC}{2.OB}\right)$$

$$\Rightarrow \beta = 2\arcsin\left(\frac{4.AO.\sin(\alpha).\sin\left(\frac{\theta}{2}\right)}{2.OB}\right) = 2\arcsin\left(2.\sin(\alpha).\sin\left(\frac{\theta}{2}\right)\right) \text{ since AO = OB.}$$

When α and _ are very small, at the first order: $\sin(\alpha) \approx \alpha$, $\sin(\theta/2) \approx \theta/2$

So

$$\beta \approx 2\arcsin(\alpha.\theta)$$

And for same reason:

$$\beta \approx 2\alpha.\theta$$

That is to say that, if the incident angle is $\frac{\pi}{2} - \alpha$ and the two mirrors tilt with an angle _, and both α and _ are small enough, it concludes that the angle β between the two reflected beams is about 2.α._.

As we use dihedrons instead of flat mirrors, there is a second reflection with the same incident and tilted angles, and the final angle between the reflected beams $\varepsilon = 2.\beta = 4.\alpha.\theta$.

3.2.2 Acquisition and processing of the experimental data

The measurement of the temporal coherence consists in acquiring a set of single-shot interferograms while increasing the path difference between the two arms of the interferometer. In order to account for possible shot-to-shot fluctuations, a minimum of three (possibly) identical shots are performed for each path difference position. The information on the temporal coherence and the spectral shape of the source can not be fully determined by performing scanning for the positive values. It should ensure that the absolute position of the path difference is perfectly known. The zero path difference of the system, i.e. when the two dihedrons are exactly at the same height, was determined prior to the experiment with an accuracy of ~1 μm, using an optical source. As we shall see, it must be determined to better than 100 λ, where λ is the wavelength of the laser XUV. This was done by looking for interference fringes with a broadband light of limited temporal coherence. In our case we used infrared femtosecond laser pulse. Note that in some cases where the zero was accidentlly lost, the scan was extended to negative path differences to ensure that the zero path difference could be determined from the overall visibility curve. Figure 3-5 shows two examples of interferograms obtained in the present work. In the overlaping region, the two coherent beams lead to interference fringes. On each side of the fringe area, one can see the beams reflected by each dihedron. Finally the black zones above and below the reflected beams is the background zone. This zone is also important because the background has to be carefully subtracted from the signal before the visibility of the fringes can be measured.

Each detected interferogram is numerically processed in order to determine the map of local fringe visibility $V(z)$ across the interference area. We have used a Matlab software, previously developed by O. Guilbaud in his thesis. We will now describe the successive steps of the interferogram processing.

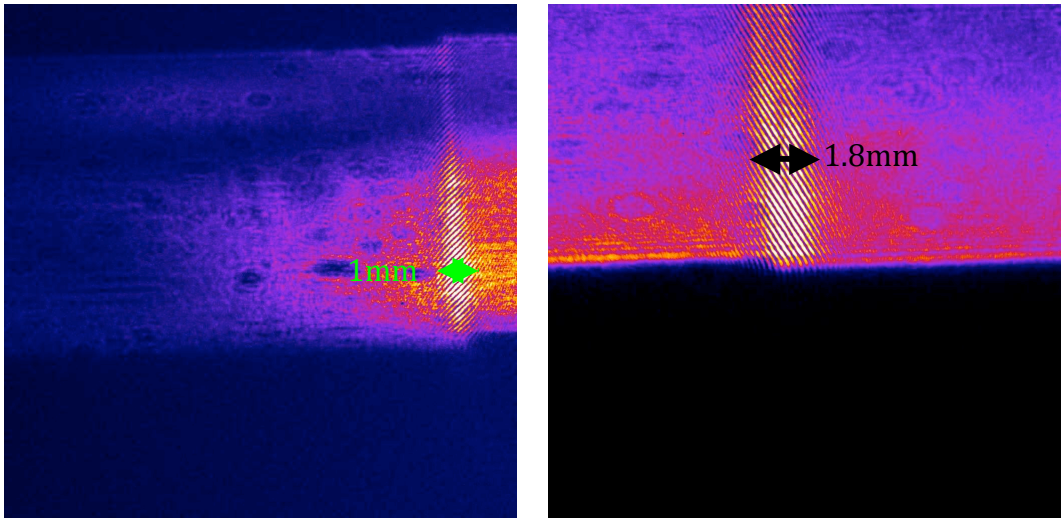

Figure 3-5: two examples of interferogram

Figure 3-6 shows a copy of the analysis window of the software used to process the experimental interferograms. The left image is the raw experimental data. The white squares show the two regions of interest for the numerical processing: the fringe area and the background area. The background level averaged over this area is subtracted from the signal in the fringe area. The top-right image in Fig. 3-6 ("Region of interest") is the selected interference area (background corrected) over which the fringe visibility will be measured. This is achieved by performing numerically a Fast-Fourier-Transfom (FFT) processing of the signal over the zone of interest by using a small sliding window. The size of this sliding window is a user-defined parameter of the software, and it is chosen to include ~3 fringe maxima. Each FFT of the signal in the window yields a local 2D spatial frequency spectrum, as the one shown in Fig. 3-6 (top center image). In this image the two secondary peaks that appear on each side of the zero-order central peak correspond to the fringe modulation frequency. The local fringe visibility is then given by $V=2.\ A_1/A_0$, where A_1 (resp. A_0) is the amplitude of the secondary peak (resp. central peak). The FFT is applied to the full zone of interest by sliding the window horizontally and vertically. This yields the 2D visibility map corresponding to the region of interest, as shown in the right-down image.

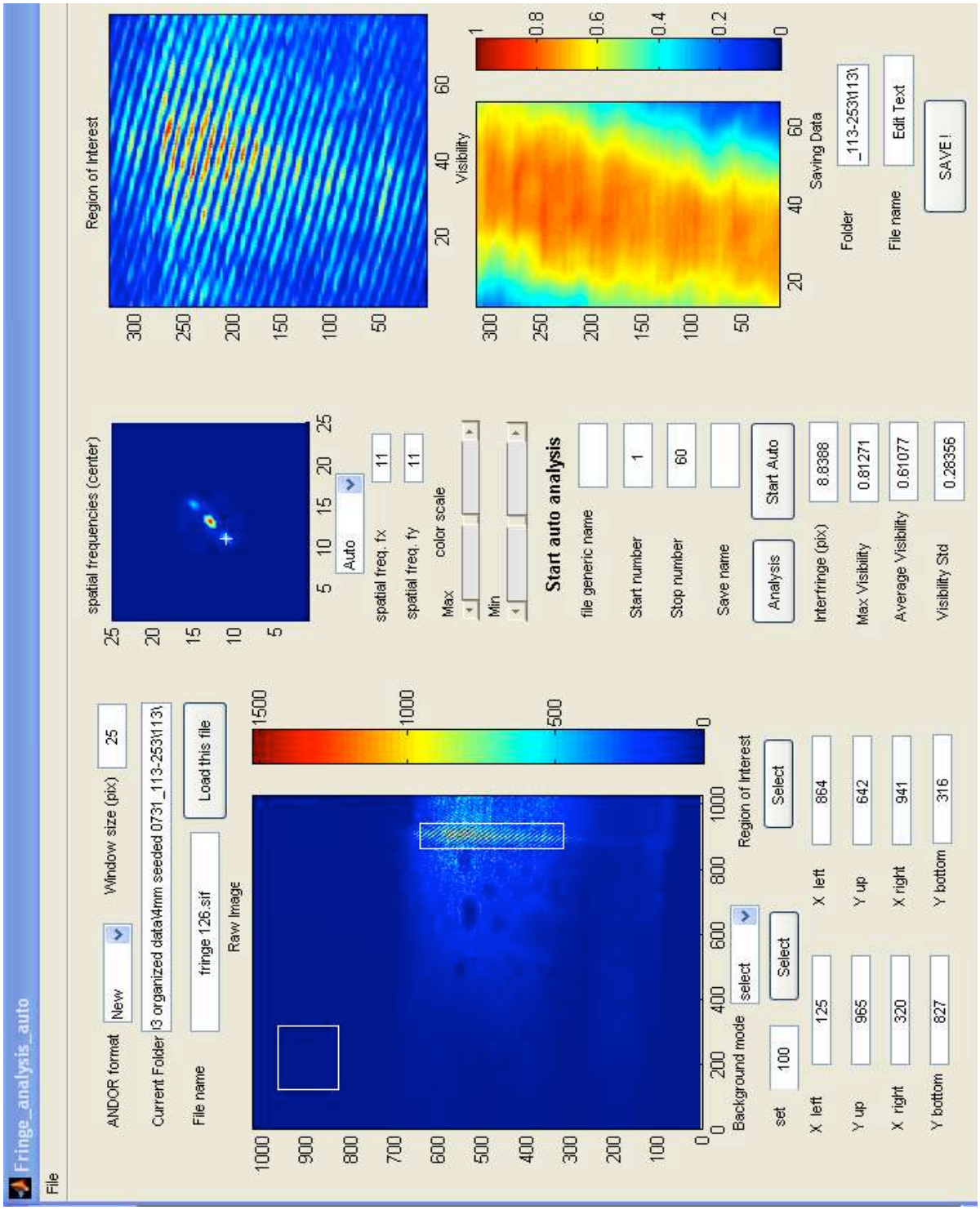

Figure 3-6 analysis window of the software used to process the experimental interferograms. The units of the size are all in pix, and 1pix =13um

One can see that the measured visibility is not uniform over the region of interest. The software also indicates the maximum visibility in this region, as well as the average value and the standard deviation. The relevant value that is used in our analysis is the maximum visibility. The reason is as follows:

The visibility of the fringes depends not only on the coherence of the two interfering beams, but also on their balance of intensity. This is expressed by the relation (already discussed in section 1.4 of chapter 1):

$$V = \frac{\sqrt{R}}{1+R} |\gamma(\tau)|$$

where $R=I_1/I_2$ and I_1, I_2 are the intensities of the two interfering beams. $\gamma(\tau)$ is the complex degree of coherence defined in equations 1-32 and 1-33. If we assume that the same coherence conditions exist over the small beam section sampled by the interferometer, then the variations of visibility are only due to variations of the intensity ratio R across the zone where the interfering beams overlap. The relevant visibility is thus the maximum one, corresponding to R = 1. This aspect was already discussed by O. Guilbaud in his thesis [9]. The standard deviation of the measured visibility (typically 20%) was found be consistent with the observed variation of R. In the interferograms that we have processed, the non-uniformity of the interfering beams can lead to a local ratio of ~5, which would lead to a visibility reduced by ~25%.

Each interferogram processed with the technique described above yields the fringe visibility achieved for the corresponding conditions, in particular the path difference. As mentioned above, the complete measurement involves a scan of the path difference over an appropriate range. It is also essential to have several measurements for each path difference to account for inevitable shot-to-shot fluctuations. The measured visibility are then plotted as shown in Figure 3-7 (left). The error bars are the standard deviation of the measured visibility values for a given path difference. The longitudinal (temporal) coherence length is defined as the path difference at which the visibility has decreased by 1/e of its maximum.

The visibility data are then fitted with an appropriate analytical function (here a sum of 2 Gaussian functions), which is chosen to maximize the fitting coefficient (χ-square). Using the Wiener-Khintchine theorem discussed in section 1.4, the Fourier-transform of the fitted visibility curve yields the spectral profile of the lasing line and its spectral width, as shown in Figure 3-7(right).

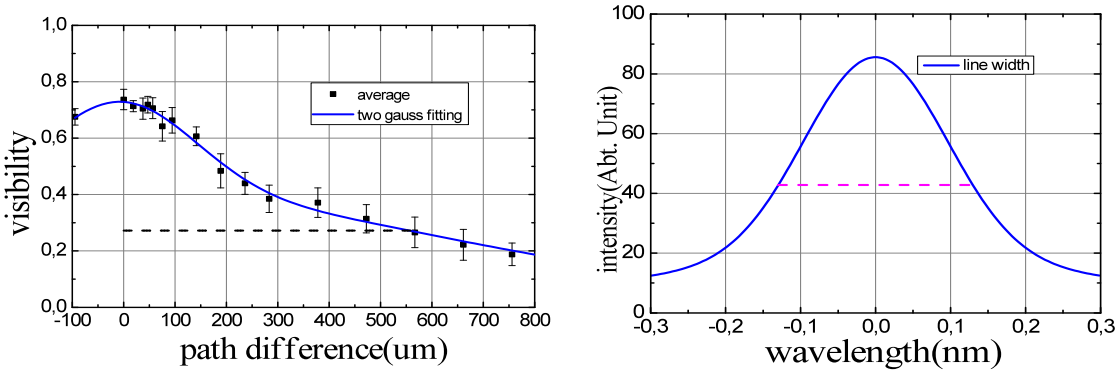

Figure 3-7: Example of a visibility curve (left) obtained from the processing of the acquired interferograms with fitting curve and corresponding Fourier transform showing the spectral profile (right).

3.3 High-resolution X-ray streak camera

3.3.1 Description of the camera

In a streak camera, a photocathode is used to generate electron bunches with temporal structures identical to that of the incident light pulses. The electrons are accelerated, then transversally deflected by a rising electric field and finally detected on a phosphor screen. Several phenomena limit the resolution of the instrument, among which the spread of the initial moment of the electrons released from the photocathode, which leads to a significant temporal broadening. The streak camera that we have used was manufactured by Axis-Photonique Inc. and belongs to the LULI-Palaiseau laboratory. It was equipped with a KBr photocathode (Luxel).

The Axis Photonique streak camera can be operated in two different regimes according to the type of acceleration: (1) acceleration by a grid or (2) acceleration by a slit. In the grid mode, the electronic optics images the 2-D image of the photocathode plane. This mode allows an application of slits of different widths. The resolution is then controlled by its width (within the resolution limits of the camera), because the best resolution with the slit is given by the time corresponding to the width of the slit image on the output screen. In the present work we have used the camera in the slit mode. In this case a virtual 150-µm wide slit placed on the photocathode plane is imaged. Hence it is not necessary to use any additional slit and the resolution remains always constant at its maximal value. However, the dynamic sensitivity is slightly reduced.

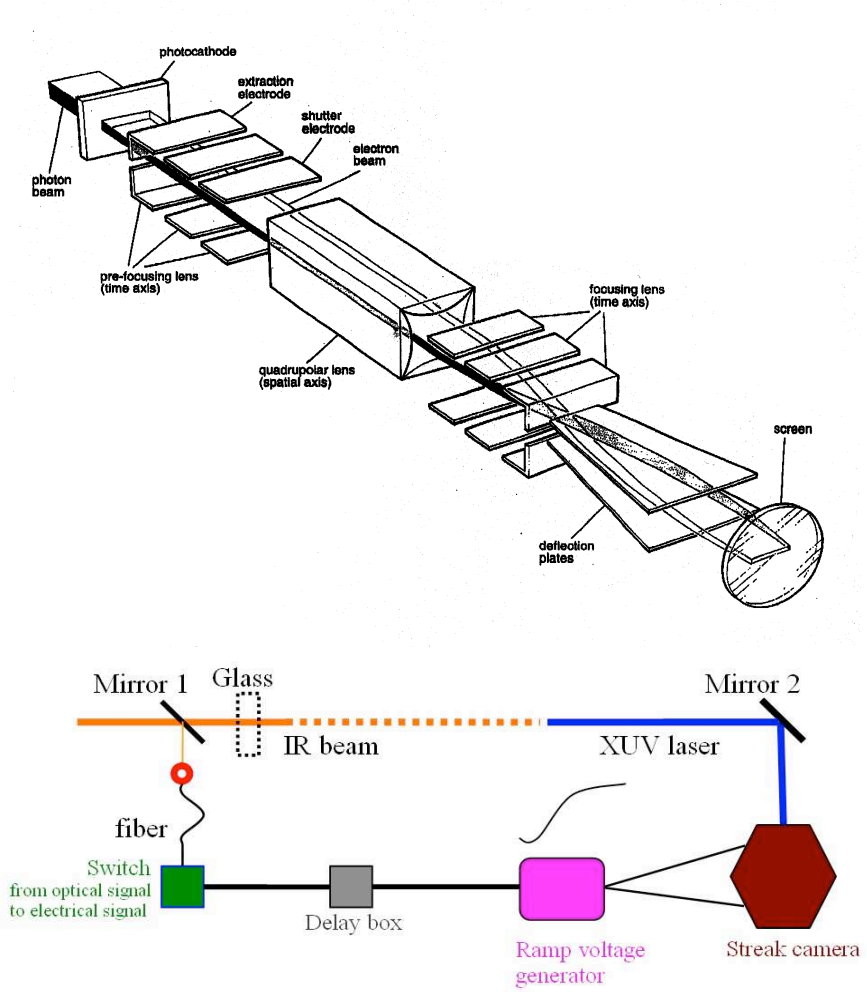

Figure 3-8. Up: schematic drawing of the Axis Photonique streak camera [10]. Down:sketch of the streak camera triggering system.

The sweeping ramp of the streak camera was synchronized with the XUV laser pulse using a switch triggered with a 0.1 mJ Ti:sapphire laser pulse (see Figure 3-8), yielding a shot-to-shot jitter of less than 10 ps. Finally a delay box was used to control the delay between the sweep of the ramp and the arrival of the XUV laser.

The specifications of the Axis Photonique streak camera are the following [11]:

Magnification in the spatial direction:	1.7
Magnification in the temporal direction:	0.4
Resolution on the output:	4.8 ± 0.4 ps/mm
Temporal resolution:	~700 fs in the 1-2keV range
	<500 fs at 260 nm (UV)

The temporal resolution had been previously measured in the UV range and in the keV range, but was never measured in the XUV range. Using high-order harmonic radiation of

duration ~30 fs generated at the LASERIX facility, we have measured in-situ the temporal duration of the camera at λ~20 nm. We find that the temporal resolution is lower than expected, T_r ~ 2.0±0.18 ps (see Figure 3-9).

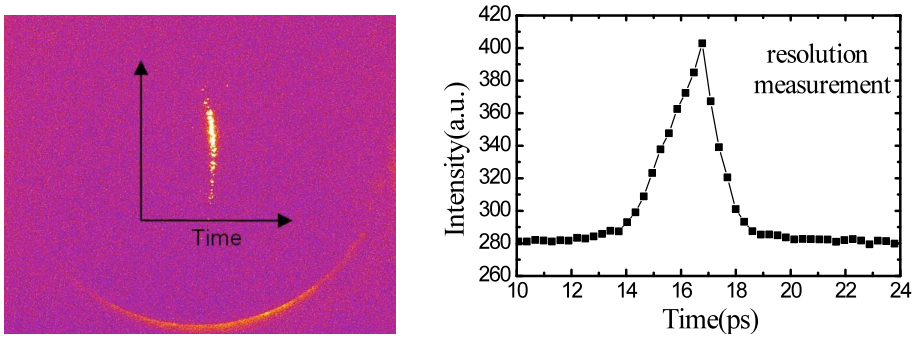

Figure 3-9. The temporal resolution of the Streak camera was measured using a femtosecond high-order harmonic pulse. Left: time-resolved signal. Right Lineout versus time, after correction from distortion. The temporal resolution is measured at 2.0±0.18 ps.

Finally the sweep speed of the streak camera was checked in-situ by generating a double-pulse XUV laser, with a known temporal separation. This was achieved by inserting a glass wedge (BK7, thickness 12.9 mm, corresponding to 23.2 ps delay) in half of the beam section of the short pump pulse. This resulted in half of the line focus being irradiated at a later time and in the generation of two successive XUV laser pulses, as shown in figure 3-10. The measurement of the peak-to-peak separation between the two pulses shown in the plot (figure 3-10, right) yields a temporal scale, or sweep speed, of 0.305 ps/pixel. This value is consistent with the calibration indicated in the technical report of the camera.

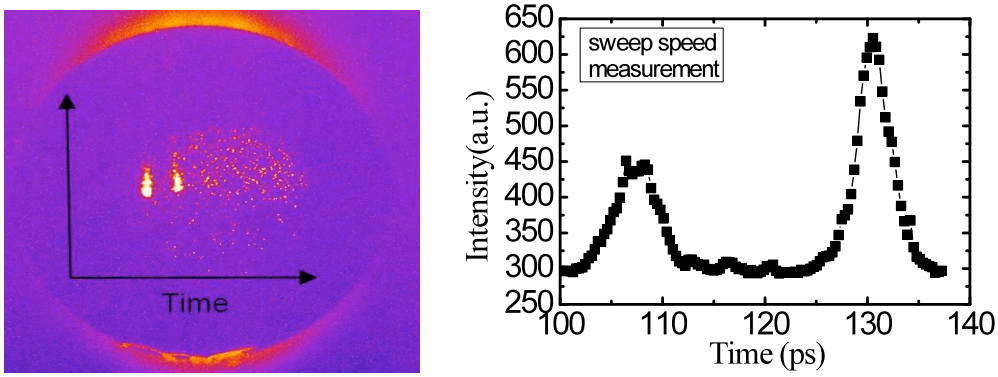

Figure 3-10. A double pulse XUV laser was generated to calibrate the sweep speed of the streak camera. Left: time-resolved image. Right: lineout versus time, after correction from distortion. The temporal separation between the pulses is 23.2 ps.

3.3.2 Acquisition and processing of the data

For the experiment described in chapter 4, the XUV laser beam was reflected by a spherical multilayer mirror which formed the magnified (M = 6), time-integrated image of the output plane of the source (near-field image). Using a translatable flat multilayer mirror, this image could be formed either onto a CCD camera (time-integrated mode) or onto the entrance slit of the streak camera (time-resolved mode). Aluminium filters with variable thickness (0.3 - 2μm) were used to attenuate the XUV laser signal. Finer adjustment of the signal level was obtained by adjusting the size of the XUV laser beam spot at the photocathode slit with a slight translation of the imaging mirror. The size of the spot was increased until it was observed that space-charge broadening, due to a too intense signal, had no appreciable effect on the temporal measurements.

Figure 3-11 shows a typical example of time-resolved image. The curved shape of the time-resolved signal is due to instrumental distortion [12] and needs to be corrected numerically before quantitative analysis of the pulse duration. A plot of the corrected image along the temporal axis is then performed, from which the FWHM temporal width T_m is measured. The measured value T_m is then deconvolved from the finite temporal resolution T_r to yield the actual duration T_{XUV} of the Ni-like Mo laser, assuming a quadratic relation: $T_{XUV}^2 = T_m^2 - T_r^2$.

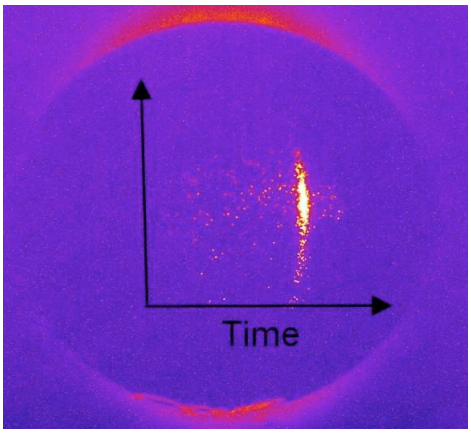

Figure 3-11. Example of tie-resolved image obtained. The curvature of the signal is due to instrumental distortion and is numerically corrected before quantitative analysis.

References

1. Jeffrey A. Koch, Brian J. MacGowan, Luiz B.Da Silva, Dennis L. Matthews, James H. Underwood, Philip J. Batson, Richard W. Lee, Richard A. London, and Stan Mrowka, "Experimental and theoretical investigation of neonlike selenium x-ra3t laser spectral linewidths and their variation with amplification", Physical Review A 50, 1877 (1994);

2. M.C. Hettrick, J.H. Underwood, P.J. Batson, M.J. Eckart, "Resolving power of 35,000 (5 mA) in the extreme ultraviolet employing a grazing incidence spectrometer", Applied Optics 27, 200 (1988);

3. R.F. Smith, J. Dunn, J.R. Hunter, J. Nilsen, S. Hubert, S. Jacquemot, C. Remond, R. Marmoret, M. Fajardo, P. Zeitoun, L. Vanbostal, C.L.S. Lewis, M.F. Ravet, and F. Delmotte, "Longitudinal coherence measurements of a transient collisional x-ray laser", Optics Letters 28, 2261 (2003);

4. A. Klisnick, J. Kuba, D. Ros, R. Smith, G. Jamelot, C. Chenais-Popovics, R. Keenan, S.J. Topping, C.L.S. Lewis, F. Strati, G.J. Tallents, D. Neely, R. Clarke, J. Collier, A.G. MacPhee, F. Bortolotto, P.V. Nickles, and K.A. Janulewicz, "Demonstration of a 2-ps transient x-ray laser",Physical Review A 65, 20 (2002);

5. R. Kienberger, E. Goulielmakis, M. Uiberacker, A. Baltuska, V. Yakovlev, F. Bammer, A. Scrinzi, Th. Westerwalbesloh, U. Kleineberg, U. Heinzmann, M. Drescher and F. Krausz, " Atomic transient recorder ", Nature 427, 817(2004);

6. Ulrike Frühling, Marek Wieland, Michael Gensch, Thomas Gebert, Bernd Schütte, Maria Krikunova, Roland Kalms, Filip Budzyn, Oliver Grimm, Jörg Rossbach, Elke Plönjes and Markus Drescher, "Single-shot terahertz-field-driven X-ray streak camera", Nature Photon. 3, 523(2009);

7. F. Albert, D. Joyeux, P. Jaegle, A. Carillon, J.P. Chauvineau, G. Jamelot, A. Klisnick, J.C. Lagron, D. Phalippou, D. Ros, S. Sebban, P. Zeitoun, "Interferograms obtained with a X-ray laser by means of a wavefront division interferometer", Opt Comm,142, 184,(1997);

8. F. Polack, D. Joyeux, J. Svatoš, and D. Phalippou, "Applications of wavefront division interferometers in soft x rays", Rev. Sci. Instr., 66, 2180 (1995) ;

9. O Guilbaud, "Etudes et applications des propriétés de cohérence des lasers X-UV à pompage transitoire", These de Doctorat, Orsay, (2004) ;

10. Axis Photonique Inc.: Caméra subpicoseconde à balayage de fente Axis-PX, Notice Technique & Rapport de tests, August 1998 (streak camera manual in French) ;

11. C. Chenais-Popovics: Mise en route de la caméra à balayage de fente Axis-photonique (Compléments de la notice), Report LULI, 1998 (in French) ;

12. C. Bonté, M. Harmand, F. Dorchies, S. Magnan, V. Pitre, J.-C. Kieffer, P. Audebert, and J.-P. Geindre, "High dynamic range streak camera for subpicosecond time-resolved x-ray spectroscopy", Rev. Sci. Inst. 78, 043503 (2007).

Chapter 4: Experimental study of the spectral and temporal properties of XUV lasers

4.1 Introduction

In this chapter we present the experimental results obtained during my thesis concerning the measurement of temporal coherence and corresponding spectral width of several types of collisional XUV lasers, all operated in the saturation regime. The experiments were carried out at three different laboratories, which allowed us to have access to 3 types of XUV lasers and to carry out a unique comparison of their spectral properties, using the same interferometer described in chapter 3.

In section 4.2 we present the results of the experiment performed at CSU (USA), where the temporal coherence and spectral width of a transient XUV laser operated in seeded mode was investigated in detail. The experiment discussed in section 4.3 was also carried out at CSU but was devoted to the Ne-like Ar XUV laser pumped by an electrical discharge in a capillary. For each of these two experiments the results are presented in the form of the corresponding scientific paper, which was published in Optics Express and Physical Review A, respectively. In section 4.4 we present the most recent experiment, which was carried out at the PALS facility (Czech Republic) in March 2012. In this experiment we have investigated the Ne-like Zn XUV laser pumped in the quasi-steady state regime.

Finally in section 4.5 we describe the results of a complementary experiment, performed at the LASERIX facility, which was focused on the investigation of the temporal properties of a transient XUV laser. The results are presented in the form of the corresponding scientific paper, published recently in Applied Physics Letters.

In section 4.6 we summarize the results obtained and discuss the comparison between the different types of investigated XUV lasers in terms of temporal coherence, spectral width and capability to amplify ultrashort (femtosecond) pulses.

4.2 Transient XUV laser in seeded and ASE modes

4.2.1 Introduction

The experiment described in the scientific paper contained in this section was carried out at the Colorado State University (CSU) in July 2009, before I started my thesis. I have been deeply involved in the processing, analysis and interpretation of the different series of interferogram data that were obtained there.

The main purpose of the experiment was to investigate the behaviour of the temporal coherence and corresponding spectral width when the Ni-like Mo transient XUV laser was operated in the seeded mode, using a high-harmonic pulse as a seed. Until now this group is the only one worldwide that has achieved seeding of transient XUV laser .The collaboration with the group of J Rocca at CSU, then, was a unique opportunity to perform our study.

In the seeded mode the length of the plasma amplifier was varied between 2 mm and 4 mm to investigate the narrowing of the line with amplification. For the longest length a measurement was performed in the ASE mode (i.e. without seeding).

The main difficulty encountered in analysing the results obtained from the processing of the interferograms (the method was described in chapter 3) was to determine the best fit of the visibility curves. As can be seen from Fig. 2 in the Optics Express paper included in this section, the shape of the visibility curve, which was found to best fit the experimental data, changes when changing the plasma length, or between seeded and ASE mode. The reason for this is not understood until now, and is not accounted for by our modelling simulations described in chapter 2.

The shape of the analytical function used to fit the data does not influence the measurement of the coherence time τ_C, which is defined as the path difference delay at which the visibility is reduced by 1/e of its maximum. However this affects the value of the corresponding linewidth, which is inferred using the Wiener-Khintchin theorem. As we have explained in chapter 1 (see section 1.4.1), the numerical coefficient, which relates the linewidth to the coherence time, depends on the shape of the coherence function $\gamma_{11}(\tau)$, or of the visibility curve. In our case the determination of the shape of the visibility curve is not accurate enough to fully rely on the different shapes observed. Hence we have used a different method to infer the coherence time and the spectral linewidth from the experimental data. This method is described in the "Principles of Optics" textbook by Born & Wolf and relies on the quadratic mean of the quantities:

$$\tau_{cq}^2 = \frac{\int_{-\infty}^{+\infty} \tau^2 |V(\tau)|^2 d\tau}{\int_{-\infty}^{+\infty} |V(\tau)|^2 d\tau} \qquad (4.1)$$

$$(\Delta\nu_q)^2 = 4\frac{\int_{-\infty}^{+\infty} (\nu - \bar{\nu})^2 G^2(\nu) d\nu}{\int_{-\infty}^{+\infty} G^2(\nu) d\nu} \qquad (4.2)$$

where $V(\tau)$ is the visibility measured as a function of path difference τ, $G(\nu)$ is the line profile, defined as the Fourier-transform of $V(\tau)$ and $\bar{\nu} = \frac{\int_{-\infty}^{+\infty} \nu G^2(\nu) d\nu}{\int_{-\infty}^{+\infty} G^2(\nu) d\nu}$. The factor 4 in the definition of $\Delta\nu_q$ assumes that the spectral profile is symmetrical. The subscript 'q' is used to distinguish from the usual definitions of τ_c (1/e of maximum visibility) and $\Delta\nu$ (FWHM).

The relationship between these usual quantities τ_c and $\Delta\nu$ and their quadratic means τ_{cq} and $\Delta\nu_q$ can be easily calculated in the exponential/Lorentzian and Gaussian/Gaussian cases, as we will show now:

Exponential visibility/Lorentzian spectrum:

$$V(t) = V(0) * \exp(-\frac{t}{\tau_c})$$

$$G(\nu) = \sqrt{\frac{2}{\pi}} \frac{G(0) * \tau}{1 + 4\pi^2\tau^2\nu^2}$$

$$\Delta\nu = \Delta\nu_{1/2-Lorentz} = \frac{1}{\pi * \tau_c}$$

Using (4.1), we find: $$\tau_{cq} = \frac{\tau_c}{\sqrt{2}} \qquad (4.3)$$

Using (4.2), we find: $$\Delta\nu_q = \frac{1}{\pi\tau_c} = \Delta\nu \qquad (4.4)$$

Gaussian visibility/ Gaussian spectrum:

$$V(t) = V(0) * Exp[-t^2 / \tau^2]$$

$$G(\nu) = \frac{G(0)}{\sqrt{2}} \exp(-\pi^2 \tau_c^2 \nu^2)$$

$$\Delta\nu = \Delta\nu_{1/2-Gauss} = \frac{2\sqrt{Ln2}}{\pi \cdot \tau_c}$$

Using (4.1), we find: $$\tau_{cq} = \frac{\tau_c}{2} \quad (4.5)$$

Using (4.2), we find: $$\Delta\nu_q = \frac{1}{\pi\tau_c} = \frac{\Delta\nu}{2\sqrt{Ln2}} \quad (4.6)$$

By comparing the quadratic linewidth $\Delta\nu_q$ expressions (4.4) and (4.6), one can see a given value of τ_c (measured at V_{max}/e in the visibility curve) will lead to the same (quadratic) spectral width $\Delta\nu_q$ for the two types of profile. Hence the quadratic definition is less sensitive to the particular shape of the analytical function used to fit the experimental data.

4.2.2 Experimental results

Temporal coherence and spectral linewidth of an injection-seeded transient collisional soft x-ray laser

L. M. Meng,[1,*] D. Alessi,[2] O. Guilbaud,[3] Y. Wang,[2] M. Berrill,[2] B.M. Luther,[2] S. R. Domingue,[2] D. H. Martz,[2] D. Joyeux,[4] S. De Rossi,[4] J. J. Rocca,[2] and A. Klisnick[1]

[1]ISMO, Bât. 350, CNRS, Université Paris-Sud 11, 91405 Orsay, France
[2]NSF Center for EUV Science and Technology, Colorado State University, Fort Collins, CO, USA
[3]LPGP, Bât. 210, CNRS, Université Paris-Sud 11, 91405 Orsay, France
[4]LCFIO, Institut d'Optique-Graduate School, 91128 Palaiseau, France
**limin.meng@u-psud.fr*

Scientific paper published in *Optics Express 19 (13) 2011, 12087*

Temporal coherence and spectral linewidth of an injection-seeded transient collisional soft x-ray laser

L. M. Meng,[1,*] D. Alessi,[2] O. Guilbaud,[3] Y. Wang,[2] M. Berrill,[2] B.M. Luther,[2] S. R. Domingue,[2] D. H. Martz,[2] D. Joyeux,[4] S. De Rossi,[4] J. J. Rocca,[2] and A. Klisnick[1]

[1]*ISMO, Bât. 350, CNRS, Université Paris-Sud 11, 91405 Orsay, France*
[2]*NSF Center for EUV Science and Technology, Colorado State University, Fort Collins, CO, USA*
[3]*LPGP, Bât. 210, CNRS, Université Paris-Sud 11, 91405 Orsay, France*
[4]*LCFIO, Institut d'Optique-Graduate School, 91128 Palaiseau, France*
*limin.meng@u-psud.fr

Abstract: The temporal coherence of an injection-seeded transient 18.9 nm molybdenum soft x-ray laser was measured using a wavefront division interferometer and compared to model simulations. The seeded laser is found to have a coherence time similar to that of the unseeded amplifier, ~1ps, but a significantly larger degree of temporal coherence. The measured coherence time for the unseeded amplifier is only a small fraction of the pulsewidth, while in the case of the seeded laser it approaches full temporal coherence. The measurements confirm that the bandwidth of the solid target amplifiers is significantly wider than that of soft x-ray lasers that use gaseous targets, an advantage for the development of sub-picosecond soft x-ray lasers.

OCIS codes: (140.7240) UV, XUV, and X-ray lasers; (300.6300) Spectroscopy, fourier transforms; (300.6560) Spectroscopy, x-ray.

References and links

1. Y. Wang, E. Granados, M. A. Larotonda, M. Berrill, B. M. Luther, D. Patel, C. S. Menoni, and J. J. Rocca, "High-brightness injection-seeded soft-x-ray-laser amplifier using a solid target," Phys. Rev. Lett. 97(12), 123901 (2006).
2. Ph. Zeitoun, G. Faivre, S. Sebban, T. Mocek, A. Hallou, M. Fajardo, D. Aubert, Ph. Balcou, F. Burgy, D. Douillet, S. Kazamias, G. De Lachèze-Murel, T. Lefrou, S. Le Pape, P. Mercère, H. Merdji, A. S. Morlens, J. P. Rousseau, and C. Valentin, "A high-intensity highly coherent soft X-ray femtosecond laser seeded by a high harmonic beam," Nature 431(7007), 426–429 (2004).
3. Y. Wang, E. Granados, F. Pedaci, D. Alessi, B. Luther, M. Berrill, and J. J. Rocca, "Phase-coherent, injection-seeded, table-top soft-X-ray lasers at 18.9 nm and 13.9 nm," Nat. Photonics 2(2), 94–98 (2008).
4. J. Ph. Goddet, S. Sebban, J. Gautier, Ph. Zeitoun, C. Valentin, F. Tissandier, T. Marchenko, G. Lambert, M. Ribières, D. Douillet, T. Lefrou, G. Iaquaniello, F. Burgy, G. Maynard, B. Cros, B. Robillard, T. Mocek, J. Nejdl, M. Kozlova, and K. Jakubczak, "Aberration-free laser beam in the soft x-ray range," Opt. Lett. 34(16), 2438–2440 (2009).
5. Y. Wang, M. Berrill, F. Pedaci, M. Shakya, S. Gilbertson, Z. Chang, E. Granados, B. Luther, M. Larotonda, and J. Rocca, "Measurement of 1-ps soft-x-ray laser pulses from an injection-seeded plasma amplifier," Phys. Rev. A 79(2), 023810 (2009).
6. D. S. Whittaker, M. Fajardo, Ph. Zeitoun, J. Gautier, E. Oliva, S. Sebban, and P. Velarde, "Producing ultrashort, ultraintense plasma-based soft-x-ray laser pulses by high-harmonic seeding," Phys. Rev. A 81(4), 043836 (2010).
7. A. Klisnick, O. Guilbaud, D. Ros, K. Cassou, S. Kazamias, G. Jamelot, J. C. Lagron, D. Joyeux, D. Phalippou, Y. Lechantre, M. Edwards, P. Mistry, and G. J. Tallents, "Experimental study of the temporal coherence and spectral profile of the 13.9nm transient X-ray laser," JQRST 99, 370 (2006).
8. O. Guilbaud, F. Tissandier, J.-P. Goddet, M. Ribière, S. Sebban, J. Gautier, D. Joyeux, D. Ros, K. Cassou, S. Kazamias, A. Klisnick, J. Habib, P. Zeitoun, D. Benredjem, T. Mocek, J. Nedjl, S. de Rossi, G. Maynard, B. Cros, A. Boudaa, and A. Calisti, "Fourier-limited seeded soft x-ray laser pulse," Opt. Lett. 35(9), 1326–1328 (2010).

#145253 - $15.00 USD Received 15 Apr 2011; revised 25 May 2011; accepted 25 May 2011; published 7 Jun 2011

9. F. Tissandier, S. Sebban, M. Ribière, J. Gautier, Ph. Zeitoun, G. Lambert, A. Barszczak Sardinha, J.-P. Goddet, F. Burgy, T. Lefrou, C. Valentin, A. Rousse, O. Guilbaud, A. Klisnick, J. Nejdl, T. Mocek, and G. Maynard, "Observation of spectral gain narrowing in a high-order harmonic seeded soft-x-ray amplifier," Phys. Rev. A 81(6), 063833 (2010).
10. M. Berrill, D. Alessi, Y. Wang, S. R. Domingue, D. H. Martz, B. M. Luther, Y. Liu, and J. J. Rocca, "Improved beam characteristics of solid-target soft x-ray laser amplifiers by injection seeding with high harmonic pulses," Opt. Lett. 35(14), 2317–2319 (2010).
11. R. Keenan, J. Dunn, P. K. Patel, D. F. Price, R. F. Smith, and V. N. Shlyaptsev, "High-repetition-rate grazing-incidence pumped x-ray laser operating at 18.9 nm," Phys. Rev. Lett. 94(10), 103901 (2005).
12. B. M. Luther, Y. Wang, M. A. Larotonda, D. Alessi, M. Berrill, M. C. Marconi, J. J. Rocca, and V. N. Shlyaptsev, "Saturated high-repetition-rate 18.9-nm tabletop laser in nickellike molybdenum," Opt. Lett. 30(2), 165–167 (2005).
13. O. Guilbaud, A. Klisnick, K. Cassou, S. Kazamias, D. Ros, G. Jamelot, D. Joyeux, and D. Phalippou, "Origin of microstructures in picosecond X-ray laser beams," Europhys. Lett. 74(5), 823–829 (2006).
14. O. Guilbaud, A. Klisnick, D. Joyeux, D. Benredjem, K. Cassou, S. Kazamias, D. Ros, D. Phalippou, G. Jamelot, and C. Möller, "Longitudinal coherence and spectral profile of a nickel-like silver transient soft X-ray laser," Eur. Phys. J. D 40(1), 125–132 (2006).
15. M. Born, and E. Wolf, "*Principles of Optics*" 7th edition, (Cambridge University Press, 2002), Chap. 10.8.3.
16. R. F. Smith, J. Dunn, J. R. Hunter, J. Nilsen, S. Hubert, S. Jacquemot, C. Remond, R. Marmoret, M. Fajardo, P. Zeitoun, L. Vanbostal, C. L. S. Lewis, M.-F. Ravet, and F. Delmotte, "Longitudinal coherence measurements of a transient collisional x-ray laser," Opt. Lett. 28(22), 2261–2263 (2003).
17. O. Larroche, D. Ros, A. Klisnick, A. Sureau, C. Möller, and H. Guennou, "Maxwell-Bloch modeling of x-ray-laser-signal buildup in single- and double-pass configurations," Phys. Rev. A 62(4), 043815 (2000).
18. M. A. Larotonda, Y. Wang, M. Berrill, B. M. Luther, J. J. Rocca, M. M. Shakya, S. Gilbertson, and Z. Chang, "Pulse duration measurements of grazing-incidence-pumped high repetition rate Ni-like Ag and Cd transient soft x-ray lasers," Opt. Lett. 31(20), 3043–3045 (2006).

The demonstration of injection-seeded soft X-ray lasers (SXRL), generated by either transient collisional excitation in solid target plasmas [1] or optical-field-ionization in gaseous targets [2], has opened new prospects for the utilization of high-brightness plasma-based coherent soft x-ray sources for various applications. The use of high-order harmonic (HH) pulses as a seed has led to a dramatic enhancement of the spatial coherence [3,4] over those exhibited in amplified spontaneous emission (ASE) operation. The degree of temporal coherence is an important parameter that also needs to be characterized for applications. The coherence time, linked to the spectral width $\Delta\nu$ of the laser line through $\tau_c \sim 1/\Delta\nu$, also determines the ultimate minimum pulse duration that can be achieved. The shortest pulse duration measured to date for a seeded SXRL is ~1.1 ps in a Ne-like Ti plasma [5]. In order to make further progress towards sub-picosecond pulse soft x-ray lasers [5,6] it is important to obtain experimental information about the spectral characteristics of these sources. This is a challenging measurement because the narrow linewidth of SXRL lines (typically $\Delta\lambda/\lambda \sim 10^{-5}$) typically lies beyond the resolution limit of existing spectrometers in this spectral range.

In this paper we report the first measurement of the temporal coherence and spectral width of a transient solid-target SXRL injection-seeded by HH pulses. Measurements for a seeded 18.9 nm Ni-like Mo amplifier were compared to results for the ASE mode of operation and model simulations. It is shown that the injection-seeded and ASE lasers have a similar linewidth, but that the degree of temporal coherence of the seeded laser is significantly larger, approaching full temporal coherence. The narrow linewidth was resolved using a wavefront-division interferometer specifically designed to measure temporal coherence [7] from which the spectral linewidth is inferred. Such interferometer was previously used to investigate other types of SXRLs, including a 32.8 nm injection-seeded optical-field-ionization (OFI) SXRL in a Xe gas medium developed at Laboratoire d'Optique Appliquée (France) [8,9]. The transient amplifiers created by irradiation of solid targets [10] studied here are measured to have significantly larger linewidths that support the generation of shorter pulse durations.

#145253 - $15.00 USD Received 15 Apr 2011; revised 25 May 2011; accepted 25 May 2011; published 7 Jun 2011

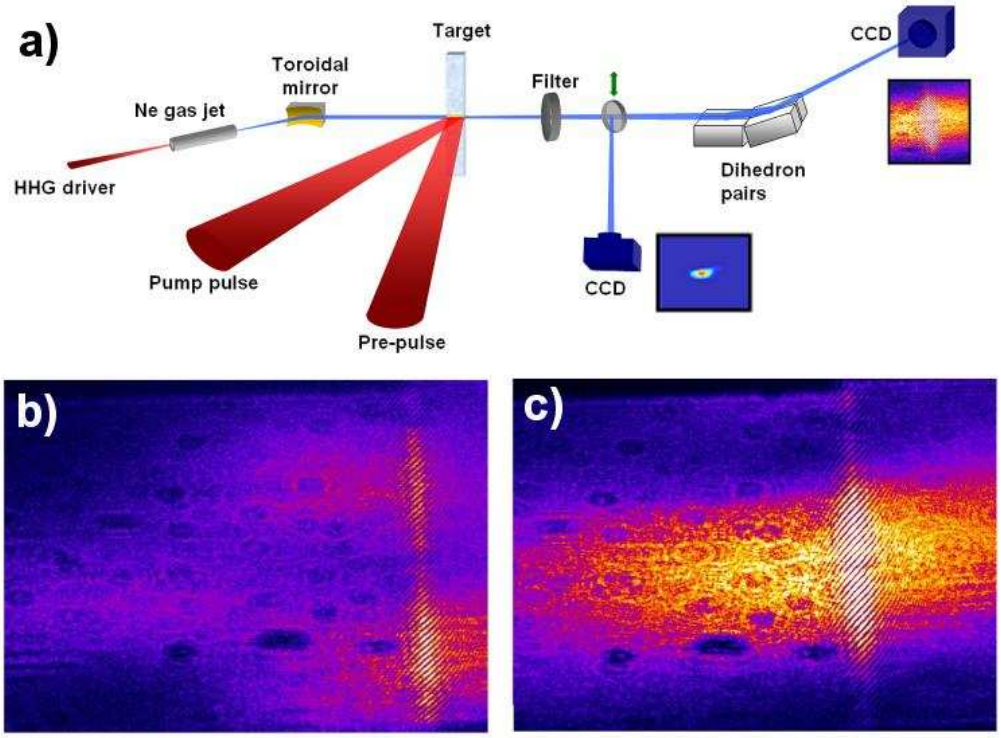

Fig. 1. (a) Experimental set up used to measure the temporal coherence of an 18.9 nm molybdenum plasma amplifier. Interferograms of the ASE (b) and seeded (c) 18.9 nm laser beam with a zero path difference between the arms of the interferometer. A 300 nm thick aluminum filter was used. In the ASE case (b) the beam is composed of several juxtaposed speckle structures. Two of them are apparent (orange white zones) in the fringe area. In the seeded case (c) one single spot is apparent, corresponding to the amplified seed beam.

The experiment was carried out at Colorado State University (CSU) using a 18.9 nm SXRL amplifier in the transient regime generated by irradiation of a solid molybdenum slab target at grazing incidence [11, 12] with pulses from an λ = 800 nm Titanium:Sapphire (Ti:Sa) laser. A sequence of two 210 ps FWHM duration pulses with energies of 45 mJ and 420 mJ are focused onto a 30 μm wide by 4 mm long line at normal incidence to the target producing a plasma with a large fraction of the ions in the Ni-like state. At a delay of 500 ps, a 3.3 ps FWHM duration heating pulse of 1J energy impinges onto the plasma at a grazing incidence angle of 23 degrees in an overlapping line focus, resulting in transient population inversion at 18.9nm. This laser amplifier was seeded with the 43rd harmonic of a femtosecond pulse from a Ti:Sa laser as described in [3] yielding a highly collimated, almost fully spatially coherent beam. The duration of the Ti:Sa pulses used to generate the high harmonic seed in this experiment was ~100fs. The output characteristics of the seeded laser are similar to that described in [3]. The SXRL beam was directed toward a variable path-difference interferometer which was set at a distance of 3 m from the source (Fig. 1(a)). A far-field monitor, consisting of a 45 degrees multilayer mirror and an XUV CCD camera could be inserted in the X-ray laser beamline (see Fig. 1(a)) to allow verification of the beam alignment before each series of measurements. The interferometer consists of a pair of dihedrons slightly tilted towards each other and irradiated under 6 degrees grazing incidence [7]. Interference fringes, which are formed in the overlapping region, are detected with a XUV CCD camera. The CCD chip is inclined to a 35 degrees incidence angle in order to increase the apparent fringe spacing to ~5 pixels/fringe. A variable path difference between the two interfering

#145253 - $15.00 USD Received 15 Apr 2011; revised 25 May 2011; accepted 25 May 2011; published 7 Jun 2011

beamlets is introduced by translating one of the two dihedrons vertically. Using a dihedron instead of a flat mirror ensures that the loss of fringe visibility when the path difference is increased is solely due to the finite temporal coherence, not to a geometrical change in the beam overlap, which depends also of the finite spatial coherence of the source. The tilt angle between the interfering mirrors is 1.6 mrad, leading to an interference field of 1 mm in the plane normal to the beam, or 1.8 mm in the CCD detector plane.

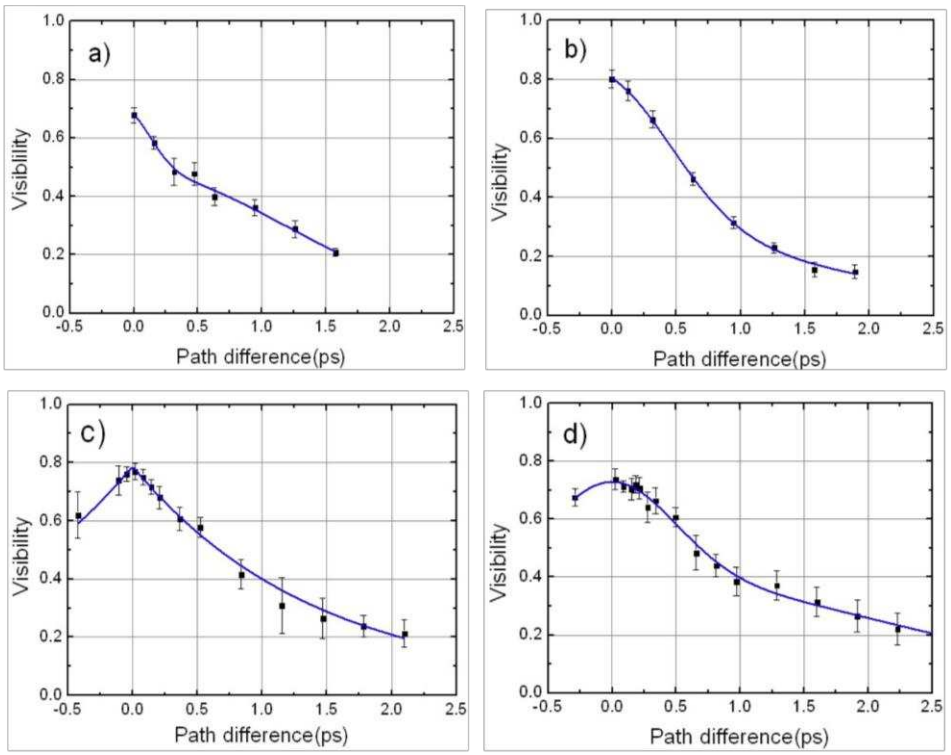

Fig. 2. (a) Visibility as a function of the path difference measured in the injection-seeded mode for the plasma amplifier lengths of 2 mm (a), 3 mm (b) and 4 mm (c). (d) Visibility data corresponding to the 4 mm ASE amplifier. The solid-line curves show the best analytical fit of the experimental data. Different types of analytical functions were used: (a) sum of two Gaussians; (b) sum of Gaussian and decreasing exponential; (c) decreasing exponential; (d) sum of two Gaussians

Series of interferograms with increasing path difference were acquired for different X-ray laser amplifier lengths. Figure 1 (b, c) shows two typical interferograms of the 18.9 nm laser obtained in the ASE mode and injection seeded mode respectively. In the ASE case, the beam is composed of randomly distributed speckles [13] which are apparent in the image. In the injection seeded case, the highly-collimated amplified HH beamlet is centered on the interference region [10]. Each interferogram was processed numerically to infer the fringe visibility for a given path difference. After background subtraction, a Fourier-transform with a sliding window [8] was applied to the full interference zone, yielding a map of visibility. The visibility was found to vary by about 20% across the zone of interest in the ASE case. This variation can be attributed to the non-uniformity of the X-ray laser beam [14] which can be seen in the images shown in Fig. 1. When the two non-uniform beamlets overlap, the visibility of the fringes is maximum only at those positions where the intensities in the two interferometer arms are equal and it is lower elsewhere. Hence the maximum visibility in the interference field was considered as the relevant value for a given interferogram. For the injection seeded case, the visibility was measured in a restricted zone containing the amplified

#145253 - $15.00 USD Received 15 Apr 2011; revised 25 May 2011; accepted 25 May 2011; published 7 Jun 2011

HH beamlet, excluding the ASE zone. In this restricted zone the variation of visibility is smaller than in the ASE case, namely less than 10%.

Figure 2 (a-c) shows the measured visibility curves obtained from the path difference scans for three different injection seeded Mo amplifier lengths. Figure 2(d) shows the measured visibility curve corresponding to the 18.9 nm laser amplifier (L = 4 mm) operated in the ASE mode. Each data point is the average of the visibility measured over 5 to 10 laser shots, and the error bar represents the standard deviation, mainly due to shot-to-shot fluctuation. In each graph, the solid-line curve shows the best analytical fit of the experimental data. To infer the coherence time τ_C and the corresponding frequency linewidth $\Delta\nu$ from our measurements we used the definitions given in [15], assuming that the spectral profile is symmetrical with respect to the central frequency $\bar{\nu}$:

$$\tau_c^{\,2} = \frac{\int_0^\infty t^2 \cdot \left|V^2(t)\right| \cdot dt}{\int_0^\infty \left|V^2(t)\right| \cdot dt} \qquad \Delta\nu^2 = 2\frac{\int_0^\infty \upsilon^2 \cdot \left|G^2(\nu+\bar{\nu})\right| \cdot d\nu}{\int_0^\infty \left|G^2(\nu+\bar{\nu})\right| \cdot d\nu} \tag{1}$$

where *V(t)* is the visibility as a function of the path difference (given by the analytical fit), *G(ν)* is the spectral power density and $\bar{\nu}$ is the average central frequency of the line. *G(ν)* is given by the Fourier-transform of *V(t)*. The above definitions, which are based on the quadratic mean of the quantities, are less sensitive to the shape of the visibility curve (i.e. to the chosen fit for the experimental data) than the usual definitions used previously [9, 14, 16]. Hence it can be judged as more appropriate in cases like ours where the shape of the visibility curve is difficult to determine accurately.

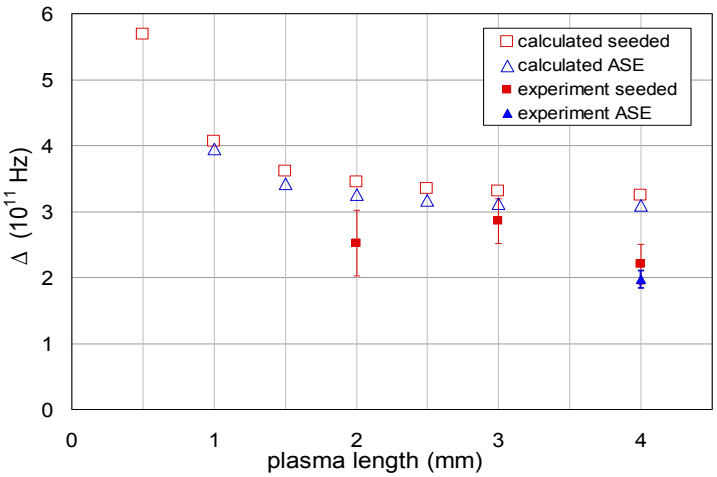

Fig. 3. Measured and computed linewidth (as defined in Eq. (1) of the injection-seeded and ASE 18.9 nm molybdenum SXRLs for different plasma lengths (see color online).

The variation of the linewidth of the seeded and ASE lasers as a function of amplifier length was simulated using the combination of a 2-dimensional hydrodynamic/atomic physics code and a 3-dimensional ray propagation code developed at CSU. The ray propagation tracks the amplification for each frequency component as the individual rays propagate taking into account refraction and gain saturation [10]. While this code does not allow the full self-consistent treatment of Maxwell-Bloch codes [17], it does include temporal broadening due to bandwidth narrowing and has the advantage of including a more detailed atomic model. The code was previously shown to satisfactorily predict the physical behavior as well as the pulse duration and energy of injection-seeded transient soft x-ray lasers in agreement with experiments [3,5]. The evolution of the plasma parameters was computed by the

#145253 - $15.00 USD Received 15 Apr 2011; revised 25 May 2011; accepted 25 May 2011; published 7 Jun 2011

hydrodynamic code and fed into the ray propagation code. The ray propagation calculation is fully resolved in space, angle, frequency, and time. Figure 3 displays the values of the measured and simulated quadratic linewidth of the injection-seeded and ASE lasers for different plasma lengths obtained using the expression defined in (1). It can be observed that smaller spectral linewidth (2.2×10^{11} Hz) corresponding to the larger temporal coherence time, (1.0 ± 0.2) ps is obtained for the longest plasma length of 4 mm, as expected from amplified radiation in the absence of saturation rebroadening. However, since most of the line narrowing due to amplification occurs in the first 2 mm of the plasma column, the measured variations as a function of plasma length are small and mostly within the error bars. It is also observed that the linewidth of the ASE X-ray laser, 1.95×10^{11} Hz, is slightly smaller (although again within the error bars) than the injection-seeded laser linewidth corresponding to the same amplifier length, as already observed for the 32.8 nm OFI SXRL in a recent experiment [9]. Such a behavior is consistent with the numerical simulations, and reflects the fact that the linewidth of the ASE and seeded lasers are dominated by the bandwidth of the amplifier, that is in turn dependent of the plasma conditions. There is no line rebroadening after saturation. The measured longitudinal coherence time for the longer seeded columns lengths of 3 and 4 mm are 0.8 ps and 1.0 ps respectively. These values are similar to the measured pulse duration of 1.13 ± 0.47 ps for a seeded solid target Ne-like Ti laser [5], that our model computations predict to be close to the pulse duration of the seeded Ni-like Mo laser, 1.3-1.5 ps. In contrast, the measured temporal coherence time is much shorter than the 4-6 ps duration computed for the ASE Ni-like Mo laser, that in turn resembles the measured ~5ps pulse durations of other similar transient collisional grazing incidence ASE lasers that were accurately predicted using the same model [18]. Therefore, it is concluded that while the injection-seeded and ASE lasers are measured to have very similar linewidths, the seeded laser has a significantly higher degree of temporal coherence that approaches full temporal coherence. The coherent time of the injection-seeded Ni-like Mo laser is also several times shorter than the transform limited pulsewidth of 4.7 ps reported for the 32.9 nm OFI laser [8], corroborating the high potential of injection-seeded transient collisional solid target amplifiers for the development of table-top SXRLs of shorter pulse duration.

Acknowledgments

This work was supported by the NSF Center for Extreme Ultraviolet Science and Technology under NSF Award EEC-0310717, by the Chemical Sciences, Geosciences and Biosciences Division, Office of Basic Energy Sciences, U.S. Department of Energy.

#145253 - $15.00 USD Received 15 Apr 2011; revised 25 May 2011; accepted 25 May 2011; published 7 Jun 2011

4.2.3 Summary

In this experiment, we measured the temporal coherence length of the Mo laser in 4 conditions: one is in ASE mode and plasma length 4mm, the others are in seeded mode and plasma length are 2 mm, 3 mm, and 4 mm separately. In table 4-2-1 we summarize all the measured values for the (quadratic) coherence length and spectral line width:

Mode	Plasma length l (mm)	Coherent length L_{cq} (μm)	Coherent time τ_{cq} (ps)	Line width $\Delta\lambda_q$ (mÅ)	Spectral width $\Delta\nu_q$ (10^{11} Hz)
seeded	2	246±15	0.82±0.05	3.0±0.6	2.52±0.50
seeded	3	249±49	0.83±0.16	3.4±0.4	2.86±0.34
seeded	4	300±46	1±0.15	2.6±0.4	2.20±0.30
ASE	4	320±150	1.1±0.5	2.4±0.2	1.97±0.13

Table 4-2-1 Summary of measured values (all the values are defined by quadratic mean)

Several additional features were noted when analysing the series of interferograms:

(1) The signal level in the seeded beam, for the same plasma length, is larger than in the ASE beam (see Figs 1 (b) and (c) in the preceding paper, generally 360 photons/pix for seeded beam vs 80 photons/pix for ASE beam).

(2) The maximum visibility in the seeded beam (typically 0.8) is slightly larger than in the ASE beam (typically 0.75) (see Figs 2 (c) and (d) in the preceding paper)

Both these features are related to the fact that the seeded beam is more coherent and more collimated than the ASE beam.

The two following features are related to the inevitable superposition, in the interferograms obtained in the seeded mode, of a central collimated seeded beam surrounded by a less intense and broader ASE beam (see Fig. 1 (c) in the preceding paper):

(3) When the path difference is large, we found that the visibility at the edge of the beam (ie in the ASE part of the beam) is slightly higher than in the centre (ie in the seeded part of the beam) (0.38 compare to 0.3). This observation is consistent with our measurement of the temporal coherence: as shown in Table 4-2-1 the temporal coherence length of the ASE beam

is slightly larger than the seeded one (although as noted in the paper, the difference lies within the error bar).

(4) In the seeded mode, for the shortest plasma length of 2 mm, the signal level in the central part corresponding to the seeded beam is very low. As a result in this case the contribution of the ASE beam to the measured signal could be significant. Since we have seen above that the temporal coherence of the ASE beam is larger than the seeded one, this could lead to a small overestimation of the coherence length of the seeded beam, and a corresponding underestimation of the spectral width. This could explain the apparent inconsistency of our results, where the measured spectral width for the 2 mm plasma is smaller than the one for the 3 mm plasma (see Fig. 3 in the preceding paper).

The main conclusions of the experiment are the following:

- The seeded mode does not affect the amplified linewidth of the XUV laser significantly although, as already observed previously in OFI-pumped lasers and in agreement with simulations results, the linewidth of the seeded pulse is slightly larger than the ASE one;

- Our results suggest that the temporal coherence of the beam is significantly increased by seeding, mainly because the duration of the seeded pulse is closer to the coherence time. This conclusion is inferred from the measurement of pulse duration achieved in similar conditions at a different lasing wavelength (32.6 nm in Ne-like Ti) and from the predictions of numerical simulations. A simultaneous measurement of the pulse duration and the coherence time of the same seeded XUV laser would be useful to confirm our statement.

- Finally we note that the apparent change in the shape of the visibilty curve when varying the plasma length, or when operating in ASE mode, is not yet understood and is not accounted for by our radiative transfer calculations. One possible explanation could be related to the fact that the XUV laser pulse is neither fully coherent, nor incoherent, but partially coherent, in a regime where the formalism used (in particular the Fourier-Khintchine theorem) could fail. Further investigations are needed beyond the present work.

4.3 Capillary discharge XUV laser

4.3.1 Introduction

The experiment described in the scientific paper contained in this section was again carried out at the Colorado State University (CSU). It was implemented in December 2009 as a follow-up of the experiment presented in the previous section. The series of measurements have been performed by the CSU PhD student L Urbanski throughout 2010, in close (remote) collaboration with our group. In particular I was responsible for the processing of all data and then took an active part in the analysis and interpretation of the results.

The main purpose of the experiment was to investigate the behaviour of the temporal coherence and corresponding spectral width of the capillary discharge XUV laser, emitted at 46.9 nm (Ne-like Ar, 3p-3s J=0-1), when reaching the saturation regime. As explained in chapter 1, this laser differs from the other collisional excitation XUV lasers by several aspects, notably the plasma parameters in the gain zone: the electron density is relatively low (~2. 10^{18} cm^{-3}) while the ionic temperature is of the same order of magnitude as the electron temperature (~100eV). As a result, the homogeneous collisional contribution to the broadening of the lasing line is much smaller than the inhomogeneous Doppler one: 5.4×10^{10} Hz and 7.3×10^{11} respectively, as predicted from calculations performed at CSU.

The capillary discharge XUV laser is thus the best suited, among the different types of collisional XUV lasers, to investigate the possible effect of saturation rebroadening, which is indeed predicted by theory when the inhomogeneous broadening is dominant. This effect was discussed in chapter 2 where the behaviour of the spectral linewidth as a function of the amplification length was investigated with radiative transfer numerical simulations. In the case of an extremely inhomogeneous profile (see section 2.4.2), the calculated spectral width was predicted to narrow down to a minimum, and then rebroaden to about 3/4 of the intrinsic width while amplified in the saturation regime.

The experimental investigation of this effect was done by measuring the temporal coherence of the capillary discharge XUV laser for several lengths, possibly both beyond and at saturation. In practice, however, it was not possible to obtain data for plasma shorter than 17 cm because the output signal was too weak. The same capillary tube was used and was progressively cut to a shorter length after the series of acquisition for a given length was completed.

The results shown in the following paper involve the processing of a very large number of interferograms, hence leading to a good statistical accuracy. More precisely the data plotted in Figure 4b of the paper correspond to an average over five series of measurements (ie from one capillary tube). In each series, the measurement of the temporal coherence was made for 7 different plasma lengths. For each plasma length, the path difference between the interfering beams was scanned over negative and positive range, with 17 different positions. For each path difference position, five successive interferograms were acquired to account for shot-to-shot fluctuations. In summary a total of ~3000 interferograms were processed and used to assess the spectral behaviour at saturation of the capillary-discharge XUV laser.

4.3.2 Experimental results

PHYSICAL REVIEW A 85, 033837 (2012)

Spectral linewidth of a Ne-like Ar capillary discharge soft-x-ray laser and its dependence on amplification beyond gain saturation

L. Urbanski,[1] M. C. Marconi,[1,*] L. M. Meng,[2] M. Berrill,[3] O. Guilbaud,[4] A. Klisnick,[2] and J. J. Rocca[1]
[1]*NSF ERC for Extreme Ultraviolet Science and Technology, Colorado State University, Fort Collins, Colorado 80523, USA*
[2]*ISMO, Bâtiment 350, CNRS, Université Paris-Sud 11, Orsay, France*
[3]*Oak Ridge National Laboratory, Oak Ridge, Tennessee 37831, USA*
[4]*LPGP, Bâtiment 210, CNRS, Université Paris-Sud 11, Orsay, France*
(Received 20 January 2012; published 29 March 2012)

Scientific paper published in *Phys. Rev. A 85 (2012) 033837*

Spectral linewidth of a Ne-like Ar capillary discharge soft-x-ray laser and its dependence on amplification beyond gain saturation

L. Urbanski,[1] M. C. Marconi,[1,*] L. M. Meng,[2] M. Berrill,[3] O. Guilbaud,[4] A. Klisnick,[2] and J. J. Rocca[1]

[1]*NSF ERC for Extreme Ultraviolet Science and Technology, Colorado State University, Fort Collins, Colorado 80523, USA*

[2]*ISMO, Bâtiment 350, CNRS, Université Paris-Sud 11, Orsay, France*

[3]*Oak Ridge National Laboratory, Oak Ridge, Tennessee 37831, USA*

[4]*LPGP, Bâtiment 210, CNRS, Université Paris-Sud 11, Orsay, France*

(Received 20 January 2012; published 29 March 2012)

We report the measurement of the linewidth and temporal coherence of a $\lambda = 46.9$ nm neon-like argon capillary discharge soft-x-ray laser and its variation with plasma column length. A wave-front-division interferometer was used to resolve the $3p\ ^1S_0$–$3s\ ^1P_1$ laser line, resulting in measured relative linewidths of $\Delta\lambda/\lambda = (3\text{–}4) \times 10^{-5}$. The measurements do not observe saturation rebroadening when this clearly dominantly Doppler-broadened inhomogeneous line is amplified beyond the intensity corresponding to gain saturation. Model simulations indicate this is the result of a comparatively small collisional broadening that sufficiently homogenizes the line profile to practically eliminate inhomogeneous saturation rebroadening. Collisional redistribution is computed to play only a very minor role in homogenizing the line profile.

DOI: 10.1103/PhysRevA.85.033837 PACS number(s): 42.55.Vc

I. INTRODUCTION

Capillary discharge soft-x-ray lasers, first demonstrated in 1994 [1], remain to date as the highest average power tabletop source of coherent soft-x-ray radiation [2,3]. The capillary discharge Ne-like Ar laser operating at $\lambda = 46.9$ nm is also the tabletop soft-x-ray laser most broadly utilized in applications. It has been used in interferometric studies of high-density plasmas [4], high-resolution microscopy [5,6], holographic imaging [7], nanoscale patterning and machining [8,9], material ablation [10,11], single-photon ionization mass spectrometry studies of nanoclusters [12], the measurement of optical constants of materials [13], and other applications. This practical tabletop laser has been widely characterized. The gain [1,14–16], output pulse energy [2,3,16,17], pulse duration [1,2,16,17], beam divergence [1,2,15–17], and wave-front characteristics [18] have been measured. The spatial coherence of the beam has also been measured to increase as a function of plasma column length [19], reaching essentially full spatial coherence in capillary discharges 36 cm in length [20]. However, the spectral linewidth and the temporal coherence, which are important parameters in applications such as interferometry and large area nanopatterning, remained to be characterized.

Besides the practical interest in knowing the temporal coherence of capillary discharge lasers for applications, the measurement of the linewidth behavior as a function of plasma column length is also of significant interest for fundamental reasons [21,22]. This is so because this laser medium offers the opportunity to study the gain saturation behavior of a highly inhomogeneous line. In soft-x-ray laser amplifiers created by laser irradiation of solid targets the amplified laser lines have not been observed to significantly rebroaden as their intensity increases beyond the saturation intensity [21,22]. This observed lack of inhomogeneous saturation rebroadening was attributed by Koch *et al.* to homogeneous lifetime broadening resulting from electron collisions with the radiating ions, and to collisional redistribution effects that can be expected to effectively homogenize the Doppler component [21]. The latter is the result of velocity-changing collisions that transfer populations among the different velocity groups of the radiating ions such that a single velocity is no longer associated with each radiator (collisional redistribution). The capillary discharge plasma amplifiers differ from those laser-pumped solid-target collisional soft-x-ray lasers in that the electron density is typically up to two orders of magnitude lower, while the ion temperature exceeds the electron temperature. The Doppler broadening contribution clearly dominates the Voigt line profile and the collisional component that homogenizes the line profile is much less significant. This highly inhomogeneous line profile could be expected to lead to the observation of saturation rebroadening of the line not observed in previous studies of line amplification in soft-x-ray plasma amplifiers [21,22]. The relatively low electron density and moderate ion temperature that characterizes the capillary discharge plasma amplifiers also gives origin to a small linewidth that is further narrowed in the amplification process. This results in a very narrow laser line that is difficult to measure because its width is below the resolution of most existing spectrometers at this wavelength. Several measurements of the linewidth of different types of laser-pumped soft-x-ray lasers have been reported [22–27]. These measurements were conducted using either a custom-made spectrometer of extremely high resolution [22], or different types of interferometers [23–27].

In this paper we report measurements of the linewidth and temporal coherence of a capillary discharge neon-like argon soft-x-ray laser, and compare the results to model simulations. The variation of the linewidth as a function of amplifier plasma column length was measured for plasma lengths between 18 and 36 cm. The measurements were conducted using a wave-front-division interferometer specifically designed to measure the temporal coherence of soft-x-ray sources [27]. The line profile was inferred from the measurements of the fringe visibility as a function of path difference in the interferometer.

*marconi@engr.colostate.edu

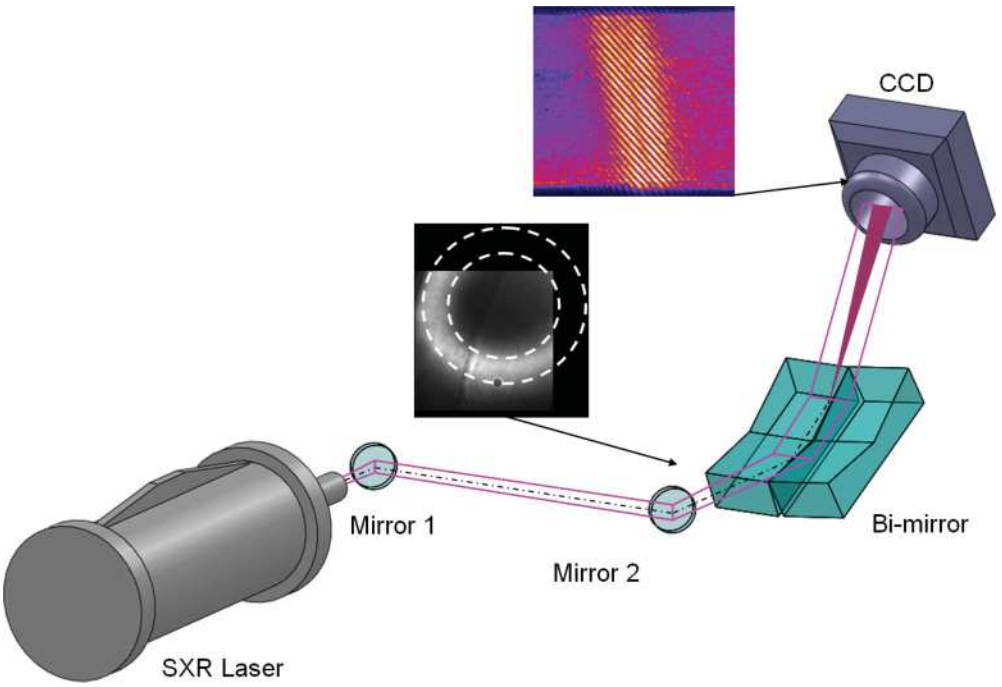

FIG. 1. (Color online) Schematic representation of the experimental set up. The output of the table top soft x ray (SXR) capillary laser is aligned with the axis of the bimirror interferometer using two multilayer mirrors that also contribute to filter off-band plasma radiation. The wave-front-division interferometer produces two beams that interfere onto a CCD. The inset shows the doughnut shape of the far-field profile of the laser beam recorded using a CCD. The size of the detector did not allow the recording of the entire beam.

This interferometer was previously used to investigate other types of collisional soft-x-ray lasers, including a 32.8-nm injection-seeded optical-field-ionization soft-x-ray laser in a Xe gas medium [23] and injection-seeded and self-seeded transient collisional soft-x-ray lasers in the 18.9-nm line of Ni-like Mo in plasmas created by laser irradiation of solid targets [26].

II. EXPERIMENTAL METHOD

The experimental setup used in the linewidth measurements is shown in Fig. 1. The capillary discharge laser beam is reflected by two 45° incidence-angle Sc-Si multilayer mirrors that are used to steer the beam for alignment with the interferometer axis. Due to its limited reflective bandwidth, the set of multilayer mirrors serves as a band-pass filter that eliminates the unwanted background caused by off-band plasma emission. The wave-front-division interferometer is based in a pair of dihedrons slightly tilted towards each other and irradiated at 6° grazing incidence (Fig. 1) [27]. This setup splits the incoming beam into two branches that are made to interfere onto the surface of a back-thinned CCD detector. The CCD is located at 50 cm from the bimirror and is tilted at an angle of 35° relative to the propagation axis to improve the spatial resolution. A precision translation stage vertically displaces one of the bimirrors relative to the other inducing a controlled optical path difference between the two interfering beams. The change in optical path difference introduces a controlled phase shift between the two beams which in turn modifies the contrast of the interference fringes. A more detailed description of the instrument can be found in Ref. [27].

Figure 2(a) shows a typical capillary discharge laser interferogram obtained with the optical path difference set to zero. The overlap of the reflections from the bimirror creates a rectangular interference region of $\sim 1.5 \times 14$ mm^2 dimension at the detector. The relative alignment of the two beams determines the orientation and density of the fringes observed. A cross section of the interferogram in Fig. 2(b) shows a visibility of 80%, indicating a high degree of spatial coherence. The measurements were conducted for discharges in a 3.2-mm-diameter capillary channel filled with a pressure of 440 mTorr of argon excited by a 21-kA peak amplitude current pulse with a 10%–90% rise time of 44 ns. This current pulse amplitude, the maximum that can be obtained in this setup for a 36-cm-long capillary, is smaller than that of some of the previously reported capillary lasers [2,3] but matches that of the most compact capillary discharge lasers [17]. It was selected to allow us to maintain the current pulse amplitude, and hence the plasma conditions, practically constant as the capillary length was increased from 18 to 36 cm to study the gain-saturation linewidth behavior. At the discharge conditions of this experiment the far-field laser beam pattern was recorded to be characterized by a doughnut shape (inset in Fig. 1) with a peak-to-peak divergence of 3.8 mrad (FWHM divergence of 4.4 mrad), resulting from refraction of the amplified beam in the radial density gradient of the cylindrical plasma column. It is possible to use the refraction angle measured from the far-field pattern to estimate the maximum electron density [28,29], in this case $\sim 1.8 \times 10^{18}$ cm^{-3}.

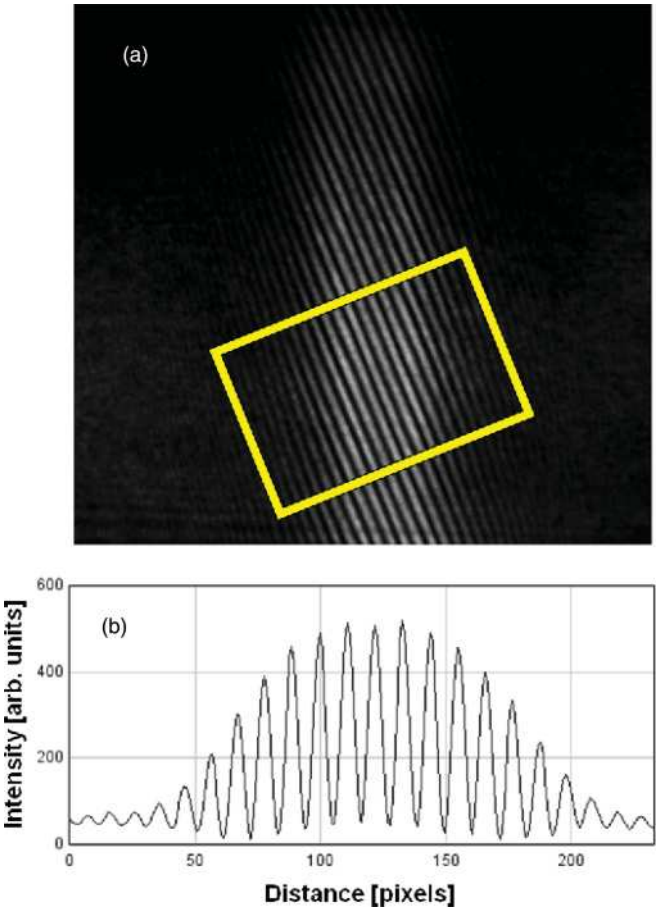

FIG. 2. (Color online) (a) Typical interferogram corresponding to the zero-path-length difference in the interferometer. The interferogram corresponds to a capillary discharge plasma column 21 cm in length. (b) Line representation of the interferogram computed from the region within the box in (a).

The spatial coherence of the beam was measured to decrease with decreasing plasma length of the neon-like Ar capillary discharge laser [20]. At the location of our interferometer, 5 m from the capillary exit, the spatial coherence radius can be estimated from these measurements to be of the order of 1 and 4 mm for the 18- and 36-cm-long capillaries, respectively. For the measurements described in this paper, this means that the maximum visibility at the zero path difference is not constant, but monotonically decreases when the plasma length is varied from 36 to 18 cm. Nevertheless it should be understood that the dihedron reflector interferometer design assures that the same two regions of the beam interfere as the path-length difference is changed [27]. This makes the measured loss of visibility independent of the variation of the spatial coherence for different capillary lengths, and solely dependent on the temporal coherence.

III. MEASUREMENTS, SIMULATIONS, AND DISCUSSION

Figure 3 shows the measured variation of the fringe visibility as a function of optical path difference for a 36-cm-long capillary discharge plasma column. Each value results from averaging the visibility measured for five laser shots. The figure

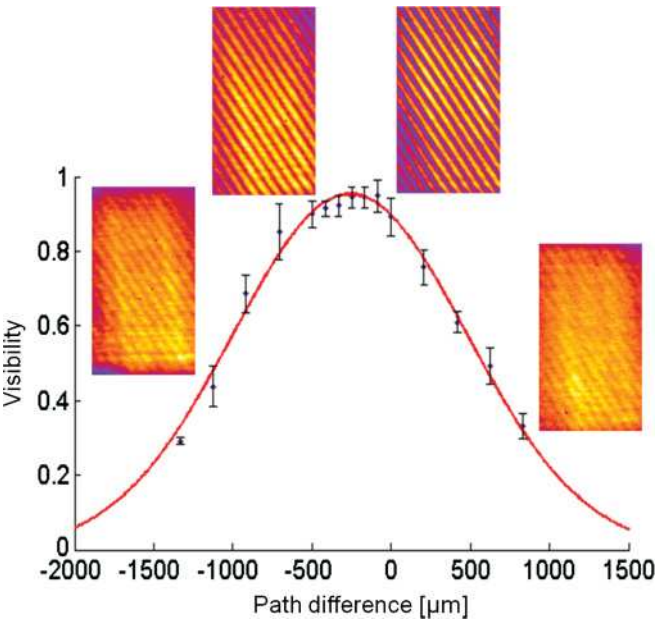

FIG. 3. (Color online) Visibilities as a function of optical path difference for a capillary discharge plasma column 36 cm in length. The insets are interferograms that illustrate the deterioration of the fringe visibility with increased path difference due to finite temporal coherence. The line is a Gaussian fit to the data.

also shows raw interferograms corresponding to different path differences, along with a Gaussian fit to the data that yields a temporal coherence length L_c defined as the e^{-1} visibility point in the Gaussian profile of $L_c = 690\ \mu$m. The corresponding linewidth is of 16.6 mÅ, or $\Delta\lambda/\lambda = 3.5 \times 10^{-5}$.

Figure 4(a) shows the measured variation of the laser output intensity, and Fig. 4(b) shows the corresponding measured variation of the laser line bandwidth as a function of capillary plasma column length. This graph shows measurements that span plasma columns lengths that are shorter and longer than the saturation length, that are observed to occur at $L_s \sim 24$ cm. Figures 4(a) and 4(b) also compare the data to the result of a model simulation that computes the line propagation along the amplifier axis taking into account gain saturation and refraction losses. The model simulates the amplification of the laser line by solving the frequency-dependent intensity and population equations accounting for Doppler and collisional broadening, gain saturation, beam refraction, and collisional redistribution. The line transport is computed by breaking the different ion velocities into subgroups, solving the population equation including stimulated emission for each velocity subgroup, and using the natural line shape with collisional broadening to obtain the frequency-dependent gain profile for each subgroup. The subgroups are summed to obtain the total frequency-dependent line shape, which is used to solve the frequency-dependent intensity equation. In turn, the total frequency-dependent intensity is used to calculate the stimulated emission rate for each population subgroup. The resulting system of equations are coupled together into a combined solution. Refraction losses are estimated according to Ref. [29] from the doughnut-shaped far-field beam profile shown in the inset in Fig. 1. Collisional redistribution of

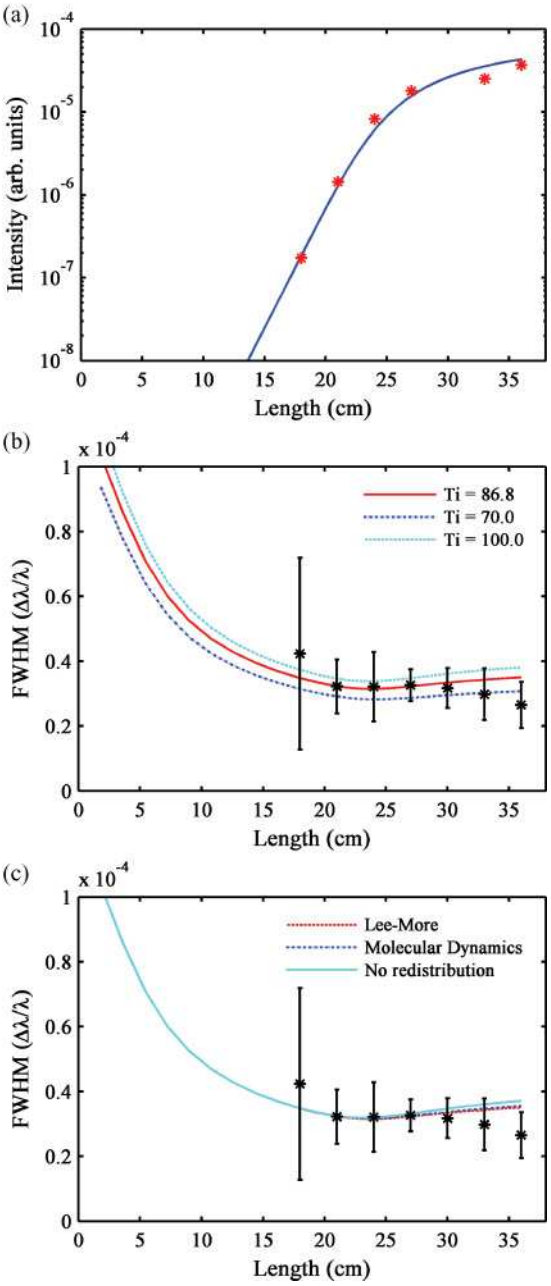

FIG. 4. (Color online) (a) Measured laser output intensity as a function of capillary discharge plasma column length. Gain saturation is observed to occur for a plasma column length of ∼24 cm. (b) Measured laser linewidth as a function of discharge plasma column length. Five independent measurements of the linewidth were averaged for each capillary length. The error bars were selected to include all measurements. The lines are the results of simulations for the plasma conditions discussed in the text, assuming ion temperatures of 100, 87, and 70 eV from top to bottom, respectively. The computations take into consideration collisional redistribution. (c) The lines show the computed variation of the linewidth neglecting (full line) and including (dashed lines) collisional redistribution. The denser dashed line was computed using the ion-ion collision time of Lee and More and the other using a collision time determined by a molecular dynamics computation [32]. The plasma parameters are those described in the text and the ion temperature is 87 eV.

the population subgroups is accounted for in a way similar to that described by Koch *et al.* [21] by considering that ion-ion collisions change the ion velocities in the direction of the laser beam, and using the ion-ion collision time to obtain the redistribution rate. This results in an additional term that couples the equations governing the different population subgroups.

The simulation results shown in Fig. 4 correspond to a plasma with an electron density of 1.8×10^{18} cm^{-3} derived from the beam divergence measured from the far-field beam refraction pattern, to ion temperatures of 70, 87, and 100 eV, and to the electron temperatures that produce the best fit in each case. The corresponding electron temperatures required to obtain the best fit of the experimental data do not change significantly, ranging from 87.4 to 92.6 eV. The value of the electron temperature required to fit the data also depends on the fraction of neon-like ions, that for the fit in Fig. 4 was assumed to be 0.75. For different fractions of neon-like ions ranging from 0.8 to 0.6 the electron temperature corresponding to the best fit varies from 88.5 to 98.1 eV. For the plasma conditions used to obtain the fits in Fig. 4 the Doppler and Lorentzian contributions to the line profile are computed to be 7.3×10^{11} and 5.4×10^{10} Hz, respectively. Most of the line narrowing due to amplification is computed to take place at plasma column lengths shorter than 18 cm, the minimum length at which the laser beam intensity was sufficiently high to allow for reliable interferometry measurements. The line does not significantly rebroaden after gain saturation is reached, contrary to the case of a purely inhomogeneously broadened line. The simulations predict only a small amount of rebroadening, that mostly falls within the error bars of the measurements. Instead the line maintains a value of $\Delta\lambda/\lambda \sim 3.5 \times 10^{-5}$. Collisional redistribution, which was previously considered by Koch *et al.* [21,22] and Pert [30] to affect the amplification dynamics of laser-pumped collisional soft-x-ray lasers created by irradiation of solid targets [21,22] is computed to play only a very small role in the saturation behavior of the capillary discharge laser. This is illustrated in Fig. 4(c) that shows small differences between fits to the data that include or neglect the effect of velocity-changing ion-ion collisions. The fits were performed with collisional redistribution rates corresponding to either the ion-ion collision time from Lee and Moore [31] (19 ps) or from a molecular dynamics computation performed specifically for the argon ions of interest (27 ps) [32]. The absence of observable rebroadening after gain saturation, caused by homogenization of the line profile by collisional broadening, takes place in spite of the fact that capillary discharge lasers operate in a regime in which Doppler broadening greatly dominates the line profile. Since the capillary discharge plasmas have up to two orders of magnitude lower plasma density than those corresponding to laser-pumped collisional soft-x-ray lasers that use solid targets [22,24–27], and a higher ion temperatures than that characteristic of optical-field-ionization soft-x-ray lasers [33], it is difficult to find among the current soft-x-ray lasers plasma conditions in which the inhomogeneous component is more dominant. This suggests that the observation of saturation rebroadening in soft-x-ray plasma amplifiers would be an unusual event.

IV. CONCLUSIONS

In conclusion, we have conducted measurements of the linewidth and temporal coherence of a capillary discharge soft-x-ray laser, and have studied its variation as a function of amplifier length. While the line profile in this discharge amplifier is clearly dominated by Doppler broadening, the relatively small collisional broadening component is still sufficiently large to homogenize the line to the point at which no rebroadening was measured to take place as the line intensity continued to increase beyond gain saturation. The narrow relative linewidth of this laser, $\Delta\lambda/\lambda = (3\text{–}4) \times 10^{-5}$, corresponds to a coherence time of ~2 ps that is much shorter than the pulse duration of 1.2–1.8 ns [2,3,17]. The degree of temporal coherence of the capillary discharge 46.9-nm laser is thus significantly lower than those previously measured in two other types of collisional soft-x-ray lasers (SXRLs), namely the 32.8-nm optical-field-ionization SXRL in a Xe gas medium [23], and the 13.9-nm and 18.9-nm transient collisional soft-x-ray lasers in Ag and Mo plasmas created by laser irradiation of solid targets [25,26]. The difference arises from the fact that while these laser-pumped systems are transient gain systems in which the laser pulse duration of a few picoseconds is relatively close to full temporal coherence, the capillary discharge laser is essentially a quasi-cw laser in which the laser pulse duration is more than two orders of magnitude longer than both the upper-laser-level lifetime and the laser pulse of the transient lasers. Nevertheless, the $L_c \sim 700\ \mu\text{m}\ (e^{-1})$ temporal coherence length measured for this capillary discharge SXRL is either similar or in some cases even larger than that of other collisional soft-x-ray lasers [24–26], which facilitates applications requiring high temporal coherence, such as interferometry [4] and large-area Talbot nanopatterning [34].

ACKNOWLEDGMENTS

We acknowledge fruitful discussion with A. Calisti (PIIM, Université de Marseille, France) on ionic correlations. The support and expertise from D. Joyeux and S. de Rossi (LCF, Institut d'Optique, Palaiseau, France) are greatly appreciated. This work was supported by NSF Grant No. PHY-1004295, the NSF Center for Extreme Ultraviolet Science and Technology under NSF Grant No. EEC-0310717, DTRA under Contract No. HDTRA 1-10-1-0070, and by the AMOS program of the Office of Basic Energy Sciences, US Department of Energy. M.B. acknowledges support for staff members at Oak Ridge National Laboratory managed by UT-Battelle, LLC, for the US Department of Energy under Contract No. DE-AC05-00OR22725.

[1] J. J. Rocca, V. N. Shlyaptsev, F. G. Tomasel, O. D. Cortazar, D. Hartshorn, and J. L. A. Chilla, Phys. Rev. Lett. **73**, 2192 (1994).

[2] B. R. Benware, C. D. Macchietto, C. H. Moreno, and J. J. Rocca, Phys. Rev. Lett. **81**, 5804 (1998).

[3] C. D. Macchietto, B. R. Benware, and J. J. Rocca, Opt. Lett. **24**, 1115 (1999).

[4] J. Filevich, K. Kanizay, M. C. Marconi, J. L. A. Chilla, and J. J. Rocca, Opt. Lett. **25**, 356 (2000).

[5] C. A. Brewer, F. Brizuela, P. Wachulak, D. H. Martz, W. Chao, E. H. Anderson, D. T. Attwood, A. V. Vinogradov, I. A. Artyukov, A. G. Ponomareko, V. V. Kondratenko, M. C. Marconi, J. J. Rocca, and C. S. Menoni, Opt. Lett. **33**, 518 (2008).

[6] F. Brizuela, G. Vaschenko, C. Brewer, M. Grisham, C. S. Menoni, M. C. Marconi, J. J. Rocca, W. Chao, J. A. Liddle, E. H. Anderson, D. T. Attwood, A. V. Vinogradov, I. A. Artioukov, Y. P. Pershyn, and V. V. Kondratenko, Opt. Express **13**, 3983 (2005).

[7] P. W. Wachulak, M. C. Marconi, R. A. Bartels, C. S. Menoni, and J. J. Rocca, J. Opt. Soc. Am. B **25**, 1811 (2008).

[8] P. W. Wachulak, M. G. Capeluto, M. C. Marconi, C. S. Menoni, and J. J. Rocca, Opt. Express **15**, 3465 (2007).

[9] L. Ottaviano, F. Bussolotti, S. Piperno, M. Rinaldi, S. Santucci, F. Flora, L. Mezi, P. Dunne, J. Kaiser, A. Reale, A. Ritucci, and P. Zuppella, Plasma Sources Sci. Technol. **17**, 024019 (2008).

[10] G. Vaschenko, A. G. Etxarri, C. S. Menoni, J. J. Rocca, O. Hemberg, S. Bloom, W. Chao, E. H. Anderson, D. T. Attwood, Y. Lu, and B. Parkinson, Opt. Lett. **31**, 3615 (2006).

[11] L. Juha, M. Bittner, D. Chvostova, J. Krasa, Z. Otcenasek, A. R. Präg, J. Ullschmied, Z. Pientka, J. Krzywinski, J. B. Pelka, A. Wawro, M. E. Grisham, G. Vaschenko, C. S. Menoni, and J. J. Rocca, Appl. Phys. Lett. **86**, 034109 (2005).

[12] S. Heinbuch, F. Dong, J. J. Rocca, and E. R. Bernstein, J. Chem. Phys. **126**, 244301 (2007).

[13] I. A. Artioukov, B. R. Benware, J. J. Rocca, M. Forsythe, Yu. A. Uspenskii, and A. V. Vinogradov, IEEE J. Sel. Top. Quantum Electron. **5**, 1495 (1999).

[14] J. J. Rocca, D. P. Clark, J. L. A. Chilla, and V. N. Shlyaptsev, Phys. Rev. Lett. **77**, 1476 (1996).

[15] A. Ben-Kish, M. Shuker, R. A. Nemirovsky, A. Fisher, A. Ron, and J. L. Schwob, Phys. Rev. Lett. **87**, 015002 (2001).

[16] G. Tomassetti, A. Ritucci, A. Reale, L. Palladino, L. Reale, S. V. Kuhklevski, F. Flora, L. Mezi, A. Faenov, T. Pikuz, and A. Gaudieri, Opt. Commun. **231**, 403 (2004).

[17] S. Heinbuch, M. Grisham, D. Martz, and J. J. Rocca, Opt. Express **13**, 4050 (2005).

[18] S. Le Pape, Ph. Zeitoun, M. Idir, P. Dhez, J. J. Rocca, and M. François, Phys. Rev. Lett. **88**, 183901 (2002).

[19] M. C. Marconi, J. L. A. Chilla, C. H. Moreno, B. R. Benware, and J. J. Rocca, Phys. Rev. Lett. **79**, 2799 (1997).

[20] Y. Liu, M. Seminario, F. G. Tomasel, C. Chang, J. J. Rocca, and D. T. Attwood, Phys. Rev. A **63**, 033802 (2001).

[21] J. A. Koch, B. J. MacGowan, L. B. Da Silva, D. L. Matthews, J. H. Underwood, P. J. Batson, R. W. Lee, R. A. London, and S. Mrowka, in *X-Ray Lasers, 1994, Williamsburg, VA*, Proceedings of the 4th International Colloquium on X-Ray Lasers–Fourth International Colloquium Book Series: AIP Conf. Proc. No. 332, (AIP, New York, 1994), pp. 574–578.

[22] J. A. Koch, B. J. MacGowan, L. B. DaSilva, D. L. Matthews, J. H. Underwood, P. J. Batson, R. W. Lee, R. A. London, and S. Mrowka, Phys. Rev. A **50**, 1877 (1994).
[23] F. Tissandier, S. Sebban, M. Ribière, J. Gautier, Ph. Zeitoun, G. Lambert, A. Barszczak Sardinha, J.-Ph Goddet, F. Burgy, T. Lefrou, C. Valentin, A. Rousse, O. Guilbaud, A. Klisnick, J. Nejdl, T. Mocek, and G. Maynard, Phys. Rev. A **81**, 063833 (2010).
[24] R. F. Smith, J. Dunn, R. Hunter, J. Nilsen, S. Hubert, S. Jaquemot, C. Remond, R. Marmoret, M. Fajardo, P. Zeitoun, L. Vanbostal, C. L. S. Lewis, M. F. Ravet, and F. Delmotte, Opt. Lett. **28**, 2261 (2003).
[25] O. Guilbaud, A. Klisnick, D. Joyeux, D. Benredjem, K. Cassou, S. Kazamias, D. Ros, D. Phalippou, and G. Jamelot, Eur. Phys. J. D **40**, 125 (2006).
[26] L. M. Meng, D. Alessi, O. Guilbaud, Y. Wang, M. Berrill, B. M. Luther, S. R. Domingue, D. H. Martz, D. Joyeux, S. De Rossi, J. J. Rocca, and A. Klisnick, Opt. Express **19**, 12087 (2011).
[27] A. Klisnick, O. Guilbaud, D. Ros, K. Cassou, S. Kazamias, G. Jamelot, J. C. Lagron, D. Joyeux, D. Phalippou, Y. Lechantre, M. Edwards, P. Mistry, and G. J. Tallents, J. Quant. Spectrosc. Radiat. Transfer **99**, 370 (2006).
[28] R. London, Phys. Fluids **31**, 184 (1988).
[29] J. L. A Chilla and J. J. Rocca, J. Opt. Soc. Am. **13**, 2841 (1996).
[30] G. J. Pert, Phys. Rev. A **50**, 4412 (1994).
[31] Y. T. Lee and R. M. More, Phys. Fluids **27**, 1273 (1984).
[32] B. Talin, E. Dufour, A. Calisti, M. A. Gigosos, M. A. Gonzalez, T. del Rıo Gaztelurrutia, and J. W. Dufty, J. Phys. A **36**, 6049 (2003).
[33] S. Sebban, T. Mocek, D. Ros, L. Upcraft, Ph. Balcou, R. Haroutunian, G. Grillon, B. Rus, A. Klisnick, A. Carillon, G. Jamelot, C. Valentin, A. Rousse, J. P. Rousseau, L. Notebaert, M. Pittman, and D. Hulin, Phys. Rev. Lett. **89**, 253901 (2002).
[34] A. Isoyan, F. Jiang, Y. C. Cheng, P. Wachulak, L. Urbanski, J. Rocca, C. Menoni, M. C. Marconi, and F. Cerrina, J. Vac. Sci. Technol. B **27**, 2931 (2009).

4.3.3 Summary

As explained in the preceding paper, the original goal of the experiment to demonstrate saturation rebroadening of a Doppler-dominated XUV laser line has not been reached. Since the effect predicted by the numerical simulations is quite small it could have been masked by the relatively limited accuracy of our measurement.

Table 4-3-1 summarizes the measured values of temporal coherence (1/e) and linewidth (FWHM) for the different plasma lengths.

Plasma length l(mm)	Coherent length L_c (μm)	Coherent time τ_c (ps)	Spectral width $\Delta\nu$ (10^{11} Hz)	Line width $\Delta\lambda$ (mÅ)
18	~557.6	1.86	2.38	17.4
21	653.4	2.18	2.03	14.9
24	651.6	2.17	2.03	14.9
27	688.4	2.29	1.92	14.1
30	657.9	2.19	2.01	14.7
33	718.2	2.39	1.84	13.5
36	795.3	2.65	1.67	12.2

Table 4-3-1 Summary of measured values

The main conclusions of the experiments are the following:

- The longitudinal coherence length of the capillary-discharge XUV laser is significantly large, typically ~700μm. This feature is clearly an asset for the application to imaging or nanopatterning developed at CSU with this source. Temporal coherence is in particular important for interferometric lithography (see e.g. refs 8 and 34 in the preceding paper).

- The coherence time of the capillary-discharge XUV laser is of 2.3 ps. This is much smaller than the pulse duration of ~2 ns measured for this laser by the CSU group. The capillary-discharge laser is thus much less temporally coherent than the transient XUV laser investigated in section 4.2.

- Much shorter pulses, in the picosecond range, could thus be obtained by seeding the capillary-discharge plasma with a femtosecond, HHG pulse. This would require an accurate synchronization (within 1 ns) between the electrical discharge system and the Ti-Sa pump laser used to generate the harmonic pulse.

4.4 Quasi-steady state XUV laser

4.4.1 Introduction

The experiment described in this section was carried out at the Prague Asterix Laser System (PALS, Czech Republic) in March 2012. The 3-week experimental campaign was performed in the frame of the Laserlab-Europe [13] transnational access to infrastructures. It involves collaborations with Institute of Physics (M. Kozlova), LOA (F. Tissandier et al.) and LPGP (O. Guilbaud). The main purpose of our experiment was to investigate the behaviour of the temporal coherence and corresponding spectral width of the QSS XUV laser, emitted at 21.2 nm (Ne-like Zn, $(2p^5_{1/2}3p_{1/2})_{J=0} \rightarrow (2p^5_{1/2}3s_{1/2})_{J=1}$). The specificities of this pumping regime were described in chapter 1 (see section 1.2.2).

4.4.2 Experimental set-up

The experimental arrangement for the XUV laser generation is shown in Figure 4-4-1. The XUV laser amplifier is generated by irradiating a 3-cm-long target, which consists of an optically-polished zinc slab with a surface flatness of about 5 μm or better. The pump-laser sequence consists of a prepulse (2J, 300ps), followed after 10 (±0.5) ns by the main driving pulse (420J, 300ps). To achieve an efficient extraction of the population inversion, the XUV laser is operated in a double-pass, using a half-cavity mirror. The mirror is positioned at 8.5 mm from the plasma. Upon activating the half-cavity mirror, the XUV laser output from a 3-cm plasma is boosted typically 11 times, compared to single-pass [1].

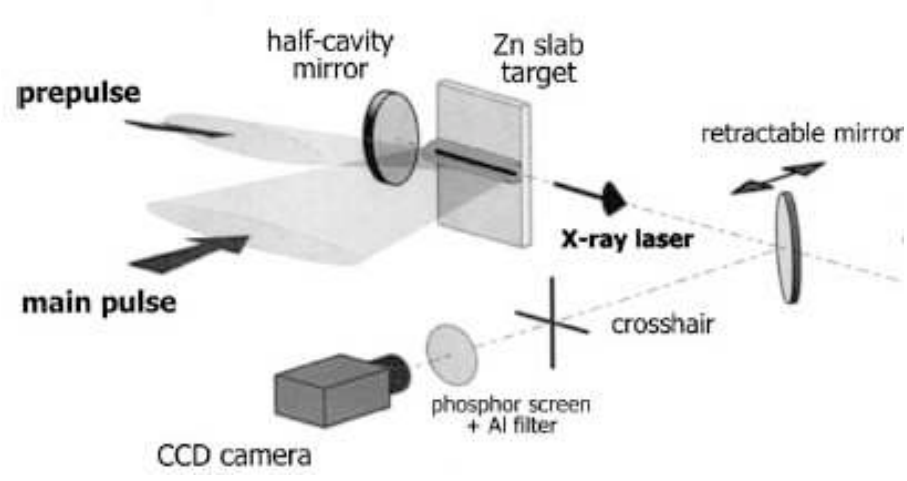

Figure 4-4-1. Schematic representation of the experimental setup for the generation of the QSS Zn XUV laser at PALS (from [1]).

The spatial coherence of the Zn XUV laser beam was investigated by the PALS group, using a Fresnel wavefront interferometer [1]. The inferferometer was positioned at a distance of 3 meters from the source. Figure 4-4-2 shows the maximum fringe visibility measured by

the authors from the interferometric images, as a function of the pump laser energy. One can see that the visibility increases with the pump energy, while the maximum visibility is ~0.5. On the other hand, the data that were collected for several days exhibit a notable scatter, which was observed to occur especially on a day-to-day basis. According to the authors, "the origin of this scatter, which is in stark contrast to the reproducibility of the x-ray laser output intensity, is not clear; it may however be at least partially attributed to the rising edge shape of the pump laser, which was observed to vary during this particular series of shots [1]. As we will see, this day-to-day variation of the spatial coherence of the XUV laser beam was also a major concern during our experiment.

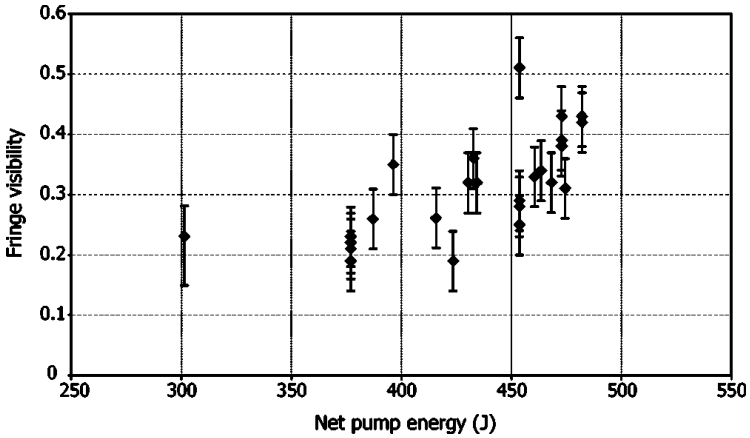

Figure 4-4-2. Visibility of the interferometric fringes generated by the half-cavity Zn laser, as a function of the pump laser energy. From Ref. [1]

For our interferometric measurement of the temporal coherence, we need that the fringe visibility at zero path-difference be larger than 0.5. It was thus decided to implement the interferometer at a distance of 5 meters from the source. At this distance, the spatial coherence length was expected to be of the same order of magnitude as the size of the overlapping region of the 2 interfering beams, that is about 900μm.

Figure 4-4-3 shows the experimental set-up used in the first part of the experiment. As we will see the visibility of the fringes at zero path-difference was found lower than expected. In the second part of the experiment, the path of the XUV laser beam to the interferometer was increased (see Figure 4-4-4) to reach a total distance of ~7 m. However as we will see this did not lead to a significant increase of the fringe visibility.

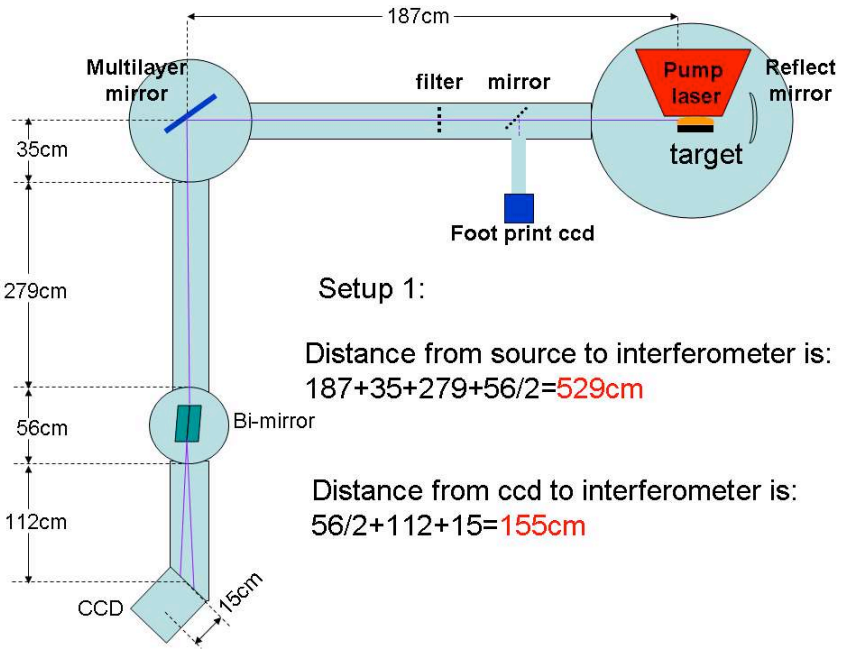

Figure 4-4-3. Experimental setup showing the XUV laser chamber and the bi-mirror interferometer positioned at 5.29 m from the source.

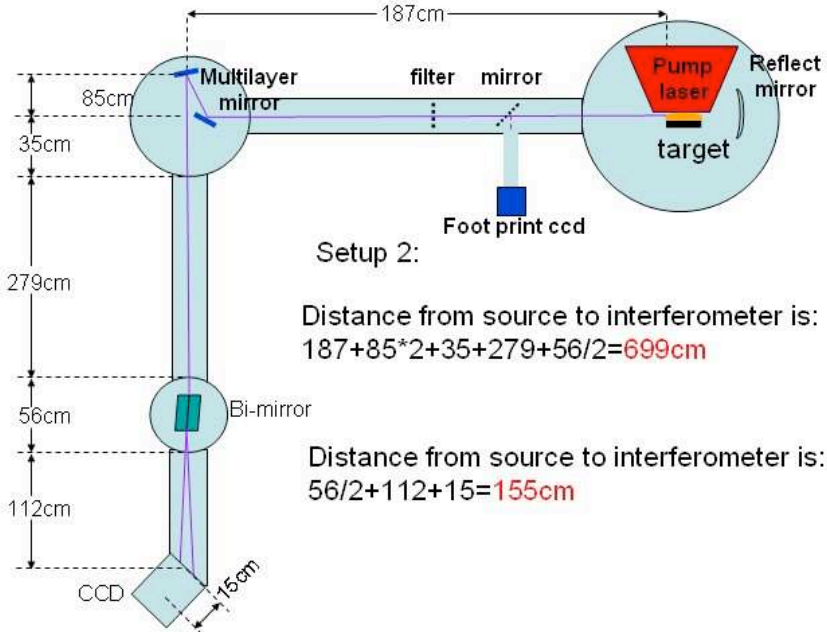

Figure 4-4-4. Same as Fig. 4-4-3 but the distance between source and interferometer is increased to 7 meters.

A footprint monitor, consisting of a translatable 45° multilayer mirror and a CCD, was used to check the stability of the XUV laser beam pointing and intensity on a day-to-day basis. An aluminium filter (thickness 2µm for D=5m and 1.2µm for D=7m) was used to attenuate the signal level at the CCD recording the interferograms. As explained in chapter 3, the CCD is set at an angle of 35° relative to the incident rays, in order to increase the apparent fringe spacing. However, due to a slight misalignment of the dihedrons that happened during

the shipping of the equipment, the fringes appeared to be much more tilted than in previous experiments. To allow a more significant stretching of the fringes through anamorphose, the CCD camera was thus rotated by 90°. In this case the image (see Figure 4-4-5 below) is stretched in the vertical direction, that is in the direction of the fringe spacing, instead of the horizontal direction.

4.4.3 Experimental results

Figure 4-4-5 shows an example of obtained interferogram in the first configuration (distance source-interferometer: 5 m) for a zero path-difference between the interfering beams. The fringe spacing is 6 pixels and the overlapping zone is 650µm. The measured fringe visibility is reasonably uniform over the interference area, but it is lower than expected: ~ 0.36.

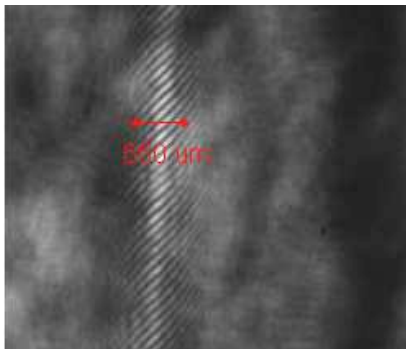

Figure 4-4-5. Portion of an interferogram showing the interference fringes formed by the Zn XUV laser

A first series of measurements was carried out with this configuration. The path difference was varied positively and negatively up to ~ 200µm around the zero path-difference position. Figure 4-4-6 shows the measured visibility as a function of path difference (in microns). The measurement data were obtained within 3 successive days (represented with 3 different colors in Fig. 4-4-6). The visibility data were then fitted with a Gaussian function shown in Figure 4-4-6.

From this fit a temporal coherence length (at 1/e) L_{tc} of **212 ±9 µm** was inferred.

A second series of measurements was carried out in the second configuration, ie with a distance source-interferometer of 7 meters. To avoid possible fluctuations of the spatial coherence of the XUV laser beam on a day-to-day basis (as mentioned above), all the data shots were acquired in the same day. The measured visibility data are shown in Figure 4-4-7. As can be seen the visibility is not improved by increasing the distance to the source, a result

which is not understood. As in the previous configuration the visibility data exhibit a Gaussian shape.

The Gaussian fit yields a temporal coherence length (at 1/e) L_{tc} of **310 ±12µm**.

This value differs from the previous one by more than the error bar, but can still be considered as consistent, taking into account the relatively low statistics in each series, and the problem of day-to-day reproducibility of the source.

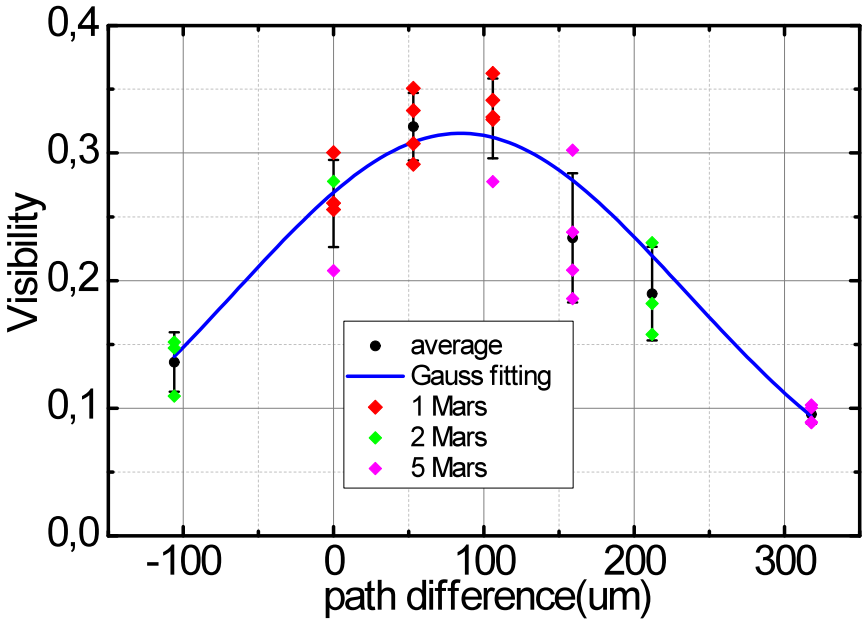

Figure 4-4-6. Series 1: Visibility measured as a function of path difference. Experimental data taken on 3 successive days and gaussian fit (blue).

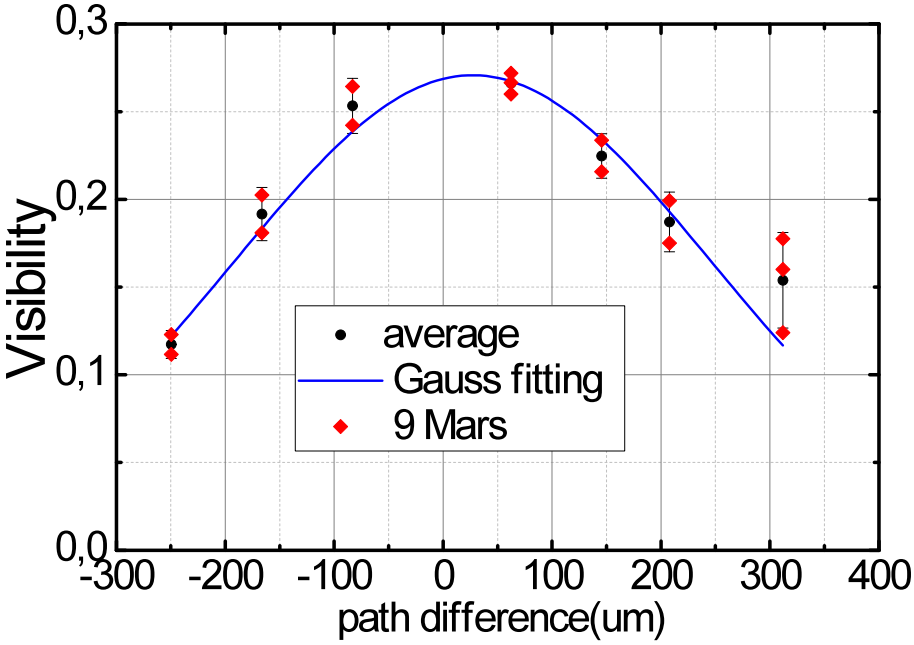

Figure 4-4-7: Series 2: Same as Fig. 4-4-8 but distance from source to interferometer is 7 m (instead of 5 m).

To calculate the corresponding FWHM spectral linewidth Δν we use the formula discussed in chapters 1 and 2:

$$\Delta\nu = \frac{2c\sqrt{\ln 2}}{\pi L_c} \text{(gaussian shape) and} \quad \Delta\lambda = \frac{\lambda^2}{c}\Delta\nu$$

The measured quantities can also be used to infer the Fourier-transform limit duration τ_{FL} that would be reached for a coherent pulse having this spectral bandwidth. We use the formula corresponding to a Gaussian spectral profile:

$$\tau_{FL} = \frac{2 \cdot Ln2}{\pi \cdot \Delta\nu}$$

The results are summarized in Table 4-4-1.

Data series	L_c (μm)	Δν (10^{11} Hz)	Δλ (mÅ)	τ_{FL}(ps)
Series 1	212 ±9	7.5±0,3	11.2±0,5	0.59 ±0.02
Series 2	310 ±12	5.1± 0,2	7.7±0,3	0.86 ±0.03

Table 4-4-1: Measured coherence length (1/e) for the two series of measurements shown in Figs 4-6 and 4-7 and corresponding spectral width (FWHM) and Fourier-transform limit duration.

The spectral width of the 21.2 nm laser line is thus measured as 11.2 mÅ in series 1 and 7.7 mÅ in series 2.

This corresponds to Fourier-transform limit durations that are both below 1 picosecond, **in contrast with all XUV lasers investigated until now**.

4.4.4 Comparison with numerical simulations

Calculations of the intrinsic linewidth of the Zn XUV laser were performed by A. Calisti and colleagues from PIIM, using the PPP code already mentioned in chapter 2. Since the plasma parameters in the gain zone are not known accurately, upper and lower bounds of the plasma density and temperatures were considered [14]:

Ne ~ 2-5.10^{20} cm^{-3}, kTe ~ 200-300 eV; kTi ~ 150-200 eV

The results of the calculations are summarized in Table 4-4-2, which shows the homogeneous component and the overall intrinsic linewidth (FWHM).

Plasma condition		Overall $\Delta\lambda_{tot}$ (mÅ)	Homogeneous $\Delta\lambda_h$ (mÅ)	Doppler $\Delta\lambda_D$ (mÅ)
Te=200eV	Ne=2×10^{20}cm^{-3}	30.5	11.8	23.8
Ti=150eV	Ne=5×10^{20}cm^{-3}	39.1	24.3	24
Te=300eV	Ne=2×10^{20}cm^{-3}	33.4	11.0	27.4
Ti=200eV	Ne=5×10^{20}cm^{-3}	40.9	22.1	27.7

Table 4.4-2: Instrinsic spectral width calculated with the PPP code for the plasma parameters typical for the Zn XUV laser

As already described in chapter 2, the homogeneous component was inferred from the overall linewidth $\Delta\lambda_{tot}$ and the Doppler component $\Delta\lambda_D$ using the formula:

$$\Delta\lambda_{tot} = \frac{1}{2}\Delta\lambda_H + \left(\frac{1}{4}\Delta\lambda_H^2 + \Delta\lambda_D^2\right)^{\frac{1}{2}}$$

One can see that the relative contribution of the homogeneous (collisional) broadening varies significantly with the electron density. For the largest density (N_e= 5*10^{20} cm^{-3}) the homogeneous and inhomogeneous (Doppler) contributions are similar. For the smaller density (N_e = 2*10^{20} cm^{-3}) the Doppler component is more than twice as large.

The calculated intrinsic linewidths for the 4 different plasma conditions above were then fed in the 1D-radiative transfer code described in chapter 2 to calculate the amplified linewidth.

The input parameters were as follows:

- small-signal gain g_0: 7 cm^{-1}

- reduced emissivity $j_r=j_0/I_{sat}$: varied between 10^{-7} cm^{-1} and 10^{-5} cm^{-1},

where j_0 is the emissivity.

Figures 4-4-8 to 4-4-11 show the evolution of the amplified linewidth as a function of the gain-length product G*L for the 4 different plasma conditions. In each case, three different values for the reduced emissivity are shown (expressed as JL = log(j_r) = -7, -6 or -5).

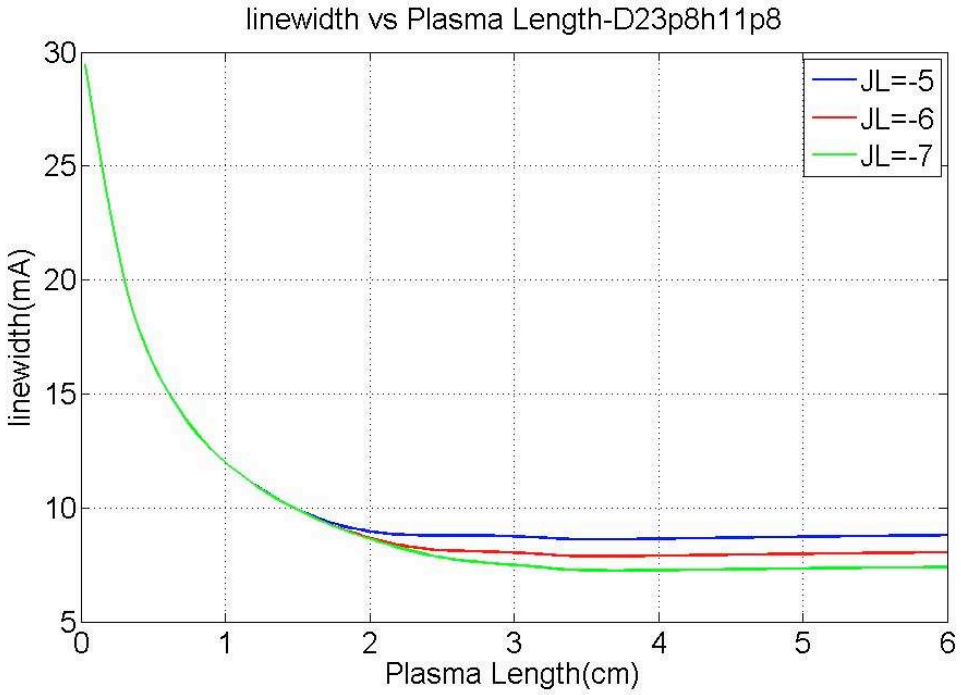

Figure 4-4-8: Amplified linewidth as a function of plasma length: kTe = 200 eV, kTi = 150 eV; Ne=2×10^{20}cm^{-3}; $\Delta\lambda_D$ =23.8 mÅ, $\Delta\lambda_h$ =11.8 mÅ; $\Delta\lambda_{tot}$ = 30.5 mÅ

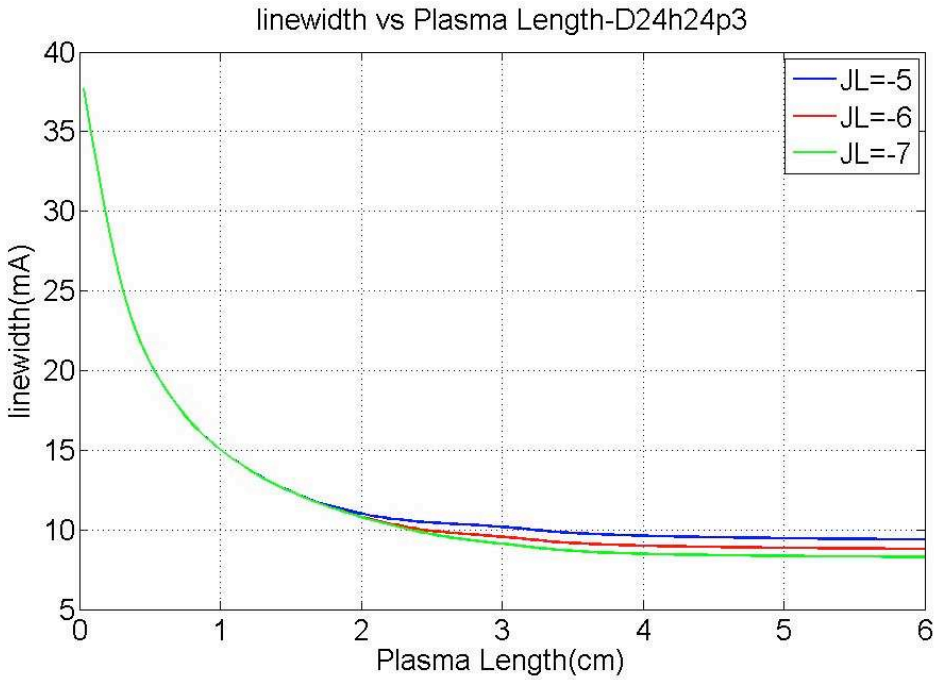

Figure 4-4-9: Same as Fig. 4-4-8, but kTe = 200 eV, kTi = 150 eV; Ne=5×10^{20}cm^{-3}; $\Delta\lambda_D$ =24 mÅ, $\Delta\lambda_h$ =24.3 mÅ; $\Delta\lambda_{tot}$ = 39.1 mÅ

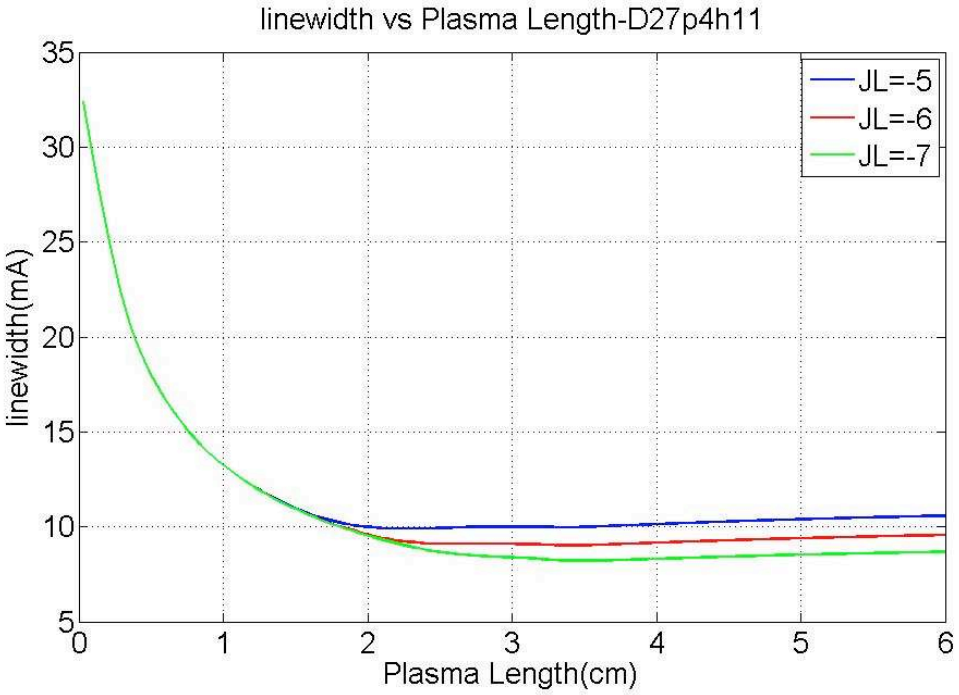

Figure 4-4-10: Same as Fig. 4-4-8, but Ne=2×10^{20}cm^{-3}; $\Delta\lambda_D$ =27.4 mÅ, $\Delta\lambda_h$ =11 mÅ; $\Delta\lambda_{tot}$ = 33.4 mÅ

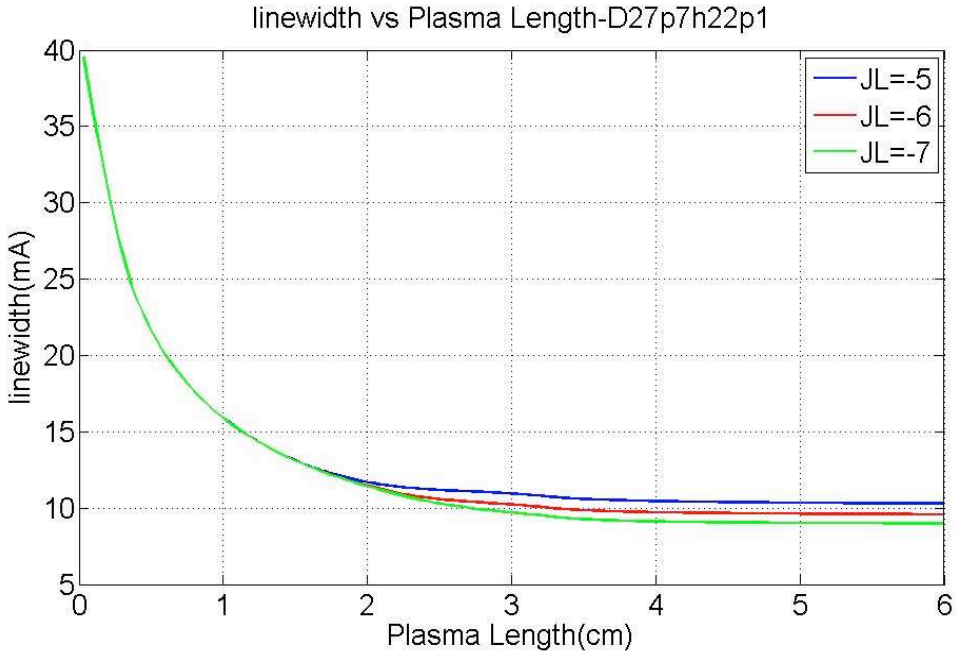

Figure 4-4-11: Same as Fig. 4-4-8, but kTe = 300 eV, kTi = 200 eV; Ne=5×10^{20}cm^{-3}; $\Delta\lambda_D$ =27.7 mÅ, $\Delta\lambda_h$ =22.1 mÅ; $\Delta\lambda_{tot}$ = 40.9 mÅ.

Finally the values of the linewidth calculated at saturation are summarized in Table 4-4-3.

Plasma condition		Intrinsic Linewidth (mÅ)	Amplified linewidth (mÅ) for different J_0/I_{sat}		
			10^{-7}	10^{-6}	10^{-5}
Te=200eV Ti=150eV	Ne=2×10^{20}cm^{-3}	30.5	7. 4	8.0	8.8
	Ne=5×10^{20}cm^{-3}	39.1	8.3	8.8	9.4
Te=300eV Ti=200eV	Ne=2×10^{20}cm^{-3}	33.4	8.7	9.6	10.6
	Ne=5×10^{20}cm^{-3}	40.9	9.0	9.6	10.3

Table 4-4-3: Amplified spectral width of the Zn laser calculated with the radiative transfer code

The calculated values of $\Delta\lambda$ shown in Table 4-4-3 account very well for our measurements of 7.7 mÅ and 11.2 mÅ. The range over which the calculated values vary suggests that the difference between our two measurements might be due to slightly different plasma conditions in the gain zone.

4.4.5 Summary

We have measured the temporal coherence and spectral width of Ne-like Zn XUV lasers pumped in the quasi-steady state regime. The measured values, which have been summarized in Table 4-4-1, are in good agreement with the results of our radiative transfer calculations, within the considered plasma parameter range.

Our experimental results should however still be considered as preliminary, owing to the small number of useful shots available during the experimental campaign. In particular the two series of measurements lead to values that are consistent but differ by more than the estimated error bar.

The accuracy of our measurement has been limited by several points, which should be improved for a future new experiment (currently in discussion):

(1) The limited spatial coherence of the beam led to a low visibility at zero path difference. The spatial coherence of the beam at the interferometer could be improved by inserting spatial filtering in the XUV laser beam path. Since the number of photons in the Zn laser pulse is very high, the measurement would not suffer from the corresponding loss of photons.

(2) The spatial coherence fluctuates especially on a day-to-day basis. A shot-to-shot monitor of the spatial coherence should be implemented. This could be done by inserting a diffraction edge or wire in the part of the XUV laser beam that is not used by the interfering mirrors.

Finally the main conclusion of the experiment is that we have measured for the first time a spectral bandwidth compatible with amplified pulse duration shorter than 1 picosecond. The Fourier-transform limit duration inferred from our measurements is between 0.6 and 0.9 ps. The QSS-pumped Zn XUV laser is thus of particular interest for the generation of seeded XUV lasers with duration in the femtosecond range. The implementation of a HHG source in the XUV laser chamber is already considered at PALS. A 1 Joule-class, Ti-Sa laser is now available in the PALS building. This laser is used for different studies such as laser-acceleration of electrons. The main challenge that is now being addressed by the PALS laser team is the accurate synchronization of this Ti-Sa laser with the high-energy iodine pump laser.

4.4.6 Annex

The following paper corresponds to an oral presentation that I gave at the *13rd International Conference on X-ray Lasers.* held in Paris in June 2012. The paper was submitted for publication in the Proceedings of the Conference.

Temporal coherence and spectral linewidth of neon-like XUV lasers pumped in the quasi-steady state regime

L. Meng[1], A. Klisnick[1], M. Kozlova[2], K. Bohacek[2], M. Krus[2], J. Prokupek[2], L. Urbanski[3], M.C. Marconi[3], M. Berrill[3], J.J. Rocca[3], O. Guilbaud[4], F. Tissandier[5], S. Sebban[5], P. Zeitoun[5], A. Calisti[6], S. Ferri[6], C. Mossé[6], B. Talin[6]

[1]ISMO, CNRS- Université Paris-Sud, Orsay, France
[2]Institute of Physics of ASCR, Prague, Czech Republic
[3]NSF-ERC for EUV Science and Technology, Colorado State University, Fort Collins, USA
[4]LPGP, CNRS- Université Paris-Sud, Orsay, France
[5]LOA, ENSTA Palaiseau, France
[6]PIIM, CNRS -Aix-Marseille Université, Marseille, France

Abstract. We report recent experimental progress in the characterization of the temporal coherence and related spectral linewidth of plasma-based soft X-ray lasers (SXRL). New measurements were carried out with two types of SXRLs pumped in the quasi-steady state (QSS) regime, in a capillary-discharge plasma and in a laser-produced plasma. We describe the main results obtained from both experiments and compare them to dedicated numerical simulations. We discuss the results in the context of the possibility to achieve XUV lasers with pulse duration below 1 picosecond.

1 Introduction

The progress of collisional soft X-ray lasers (SXRL), generated by quasi-steady state [1] or transient pumping in solid target plasmas [2], optical-field-ionization in gaseous targets [3], and capillary discharges [4], have opened the way to compact devices and new prospects for various applications. This requires a detailed characterization of their output parameters, like the energy per pulse, duration etc. The spectral linewidth $\Delta\lambda$, or the coherence time τ_c are also very important parameters, since they determine the shortest pulse duration (Fourier-transform limit τ_{FL}) that can be achieved (in a linear amplification regime), through the relation: $\tau_{FL} = \alpha \frac{\lambda^2}{\Delta\lambda} = \beta\tau_c$, where α and β are numerical factors depending on the particular shape of the line profile. The spectral width of the SXRL line results from the complex combination of several processes, namely the contribution of homogeneous (natural and collisional) and inhomogeneous (Doppler) broadenings of the intrinsic profile, followed by gain narrowing with amplification of the line along the plasma length [5]. When inhomogeneous broadening is the dominant cause of broadening the line can be rebroadened when the laser reaches saturation [6].

The purpose of our work is to characterize experimentally the spectral behaviour of existing collisional excitation SXRLs, and to evaluate their potential to support the amplification of pulses with duration below 1 ps. Over the recent years, our previous studies were devoted to short pulse (femtosecond to picosecond) pumped systems, in which the duration of the SXRL pulse is of the same order of magnitude as the coherence time. At LOA-Palaiseau (France), a coherence time of ~ 5 ps was measured in a Ni-like Kr laser generated at 32.8 nm from an optical-field ionized plasma [7]. At Colorado State University (USA), a shorter coherence time of ~1 ps was measured in a Ni-like Mo laser (λ = 18.9 nm) pumped in the transient regime with a grazing incidence irradiation geometry [8]. Here in the present paper, we present new measurements that were carried out with two types of neon-like SXRLs, pumped in the quasi-steady state (QSS), long pulse (100 ps to nanosecond) regime: the capillary-discharge argon laser generated

at CSU (USA) [9, 10], and the Ne-like Zn laser generated at PALS (Czech Republic) [1]. These sources differ from the previous ones by several aspects, among which a higher ionic temperature leading to a larger contribution of Doppler broadening of the laser lines.

We used a variable path-difference, wavefront-division interferometer, which was specifically designed to measure the temporal coherence of the source. This interferometer, described in [11], is composed of two dihedrons, tilted towards each other with a small angle. The incoming beam is separated into two beamlets that slightly converge towards each other after reflection on the dihedrons. In their overlapping region, interference fringes can be recorded using a XUV CCD camera. One of the dihedrons can be accurately translated vertically in order to introduce a path difference between the interfering beams. By following the evolution of the fringe visibility as a function of the delay with successive shots performed in identical conditions, it is possible to measure the coherence time of the pulse, and to infer the spectral width of the line through a Fourier transform.

2 Capillary-discharge Ne-like Ar laser

Capillary discharge XUV lasers are the highest average power tabletop source of coherent soft-x-ray radiation [9, 12] up to date. The capillary discharge Ne-like Ar laser operating at λ = 46.9 nm (3p-3s J=0-1 line), was first demonstrated in 1994 [4] and has been widely characterized [13-17]. However, the spectral linewidth and the temporal coherence, which are important parameters in applications such as interferometry [18] and large area nanopatterning [19], remained to be measured. Capillary discharge plasmas are characterized by a low electron density ($N_e \sim 2\times10^{18}$ cm^{-3}) and a relatively high ionic temperature ($kT_i \sim 100$ eV). The Doppler effect is thus expected to be the dominant cause of broadening of the laser line. The Ne-like Ar laser is thus an appropriate system to study the possible existence of saturation rebroadening predicted in highly inhomogeneous line profiles [20]. This is achieved by measuring the linewidth evolution with the plasma column length.

The experiment was performed at CSU (USA). The experimental setup and the results obtained are presented in more detail in [10] as well as in a companion paper (see Urbanski et al., this conference). Figure 1 (a) shows an example of the measured variation of the fringe visibility with the path difference. The coherence time is defined as the delay at which the visibility is decreased by 1/e of its maximum. We find that the experimental data fit very well to a Gaussian curve. The corresponding spectral profile, inferred by a Fourier transform of the visibility curve, is also Gaussian. The linewidth is defined as the FWHM of the spectral profile.

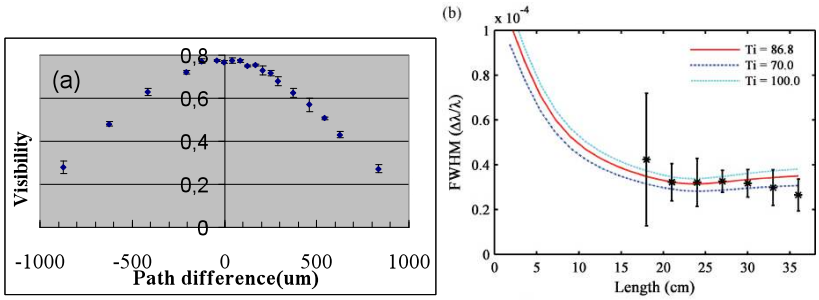

Figure 1: (a) example of a measured visibility curve; (b) measured spectral width as a function of amplifier length. The black points with error bars stand for experimental data, and the three curves show the simulation results for different temperatures [10].

The measured variation of the spectral bandwidth as a function of the plasma length is shown in Fig. 1(b). One can see that the bandwidth decreases slowly, while no rebroadening of the line is apparent for the longest lengths, although the laser is operated at saturation. The experimental data are compared to the predictions of numerical simulations, performed at CSU, that compute the line propagation along the amplifier axis taking into account gain saturation and refraction losses. One can see that these calculations predict a weak rebroadening of the line beyond L ~24 cm. However this effect is small compared to our experimental error bars. For the longest plasma length, the typical coherence time τ_c is 2.3 ps , corresponding to a Fourier limit pulse duration τ_{FL} of 1.9 ps, which are both much shorter than the duration of the SXRL pulse (1.2–1.8 ns).

3 Laser-based Ne-like Zn laser

More recently we carried out a temporal coherence measurement of the Ne-like Zn laser, emitting at 21.2 nm (3p-3s J=0-1 line, as above). This SXRL is generated at the PALS (Prague, Czech Republic) laser facility and was used for several applications [21]. The lasing plasma is pumped by a succession of a low-energy prepulse and high-energy main pulse, both ~300 ps in duration, delivered by an iodine pump laser (λ=1.315 μm). After double-pass amplification in a 3-cm zinc plasma column, the 21.2 nm pulse reaches saturation with a typical energy of ~ 1 mJ per pulse or more [1].

Although lasing is obtained on the same Ne-like 3p-3s transition as for the capillary discharge laser discussed above, the plasma conditions in the gain zone are markedly different. Here the electron density is typically x100 times higher (N_e ~ 2-5×10^{20} cm^{-3}), while the ionic temperature is only twice as high (kT_i ~ 150 - 200 eV). As a result, in Ne-like Zn, both collisional and Doppler broadenings contribute at the same level, as will be shown below.

The interferometer was implemented along the 21.2 nm beam path, at a distance of ~ 5.5 meters from the source. Figure 2 shows a typical example of a single-shot interferogram, when the path-difference between the interfering beams was close to zero. The size of the overlapping region, where fringes are apparent, is ~650 μm. This is slightly larger than the spatial coherence of the beam at the interferometer position, so that the fringe visibility is relatively low, of the order of 30%. The distance from the source was increased by ~1.5 m in a second series of measurements, but the fringe visibility was not significantly improved. Another difficulty was the limited number of shots available in a data set, due to the low repetition rate of the laser (2 shots per hour). Two series of data, where the path difference was varied from -300μm to +300 μm, were

obtained for the two different distances from the source mentioned above. They led to slightly different, although consistent values for the coherence time of the 21.2 nm laser, namely τ_c = 1 ps and 0.7 ps for the 5.5 m and 7 m distance respectively. The corresponding spectral linewidth are 11.3 mÅ and 7.7 mÅ respectively.

The measured $\Delta\lambda$ values were compared to the predictions of numerical simulations, using the PPP lineshape code [22] to calculate the intrinsic broadening, and a 1D-radiative transfer code [23] that computes the amplified profile, taking into account saturation. The plasma conditions in the gain zone are not known precisely, but estimated as $N_e \sim 2\text{-}5\times10^{20}$ cm^{-3}, kT_e = 200-300 eV; kT_i = 150-200 eV. A small-signal gain coefficient of 7 cm^{-1} was considered. We find that within this parameter range, the amplified linewidth of the 21.2 nm laser varies between 7.4 and 10.6 mÅ, in good agreement with our measurements. The contribution of the collisional broadening to the intrinsic line profile ranges from 11 to 24 mÅ, whereas the Doppler one is of the order of 25 mÅ.

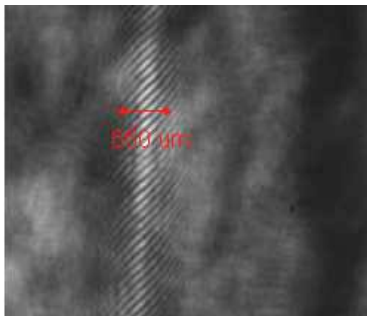

Figure 2: Portion of the interferogram detected with the Ne-like Zn laser at 21.2 nm.

Finally the measured τ_c values were used to estimate the corresponding Fourier-transform limit τ_{FL}, which is the shortest duration that could be reached if the 21.2 nm was fully temporally coherent. From the definition recalled in section 1, and considering a Gaussian shape, we find that τ_{FL} is below 1 ps for both measurements, namely 0.6 and 0.7 ps. This is the shortest value ever measured for a plasma-based SXRL and this confirms the high potential of the Zn quasi-steady state laser for the generation of femtosecond amplified pulses, through seeding with high-harmonic radiation.

4 Conclusion

We have measured the temporal coherence and spectral width of two Ne-like soft X-ray lasers pumped in the quasi-steady state regime with two distinct techniques, leading to different plasma conditions and spectral characteristics.

The Ne-like Ar, capillary-discharge pumped laser exhibits a spectral width that decreases slowly as the plasma length increases, as a result of gain narrowing. The small saturation rebroadening, predicted by numerical simulations, was not observed and could be beyond our experimental accuracy. The measured coherence time is ~ 2 ps, much shorter than the pulse duration of 1.2-1.8 ns. For the laser-pumped Ne-like Zn laser, the measured coherence time is shorter (0.7-1ps), leading for the first time to a Fourier-transform limit duration that lies below 1 ps.

In both cases, the inferred values for the spectral width of the laser line are in good quantitative agreement with the predictions of numerical simulations. Finally since the measured coherence times are in both cases much smaller than the duration of the SXRL pulse, picosecond (or potentially sub picosecond) durations could be reached through seeding with femtosecond high-order harmonic radiation.

References

1. Rus, B., et al.: 'Multimillijoule, highly coherent x-ray laser at 21 nm operating in deep saturation through double-pass amplification ', *Phys. Rev. A*., 66, 063806, 2002
2. Wang, Y., et al.: 'High-Brightness Injection-Seeded Soft-X-Ray-Laser Amplifier Using a Solid Target', *Phys. Rev. Lett.*, 97, 123901, 2006
3. Zeitoun,Ph., et al.: 'A high-intensity highly coherent soft X-ray femtosecond laser seeded by a high harmonic beam', *Nature*, 431,426, 2004
4. Rocca, J. J., et al.: 'Demonstration of a Discharge Pumped Table-Top Soft-X-Ray Laser ', *Phys. Rev. Lett.,* 73, 2192,1994
5. Koch, J. A., et al.: 'Experimental and theoretical investigation of neonlike selenium x-ray laser spectral linewidths and their variation with amplification', *Phys. Rev. A.,* 50, 1877, 1994
6. Pert, G. J.: 'Output characteristics of amplified-stimulated-emission lasers' *„J. Opt. Soc. Am. B,* 11, 1425, 1994
7. Tissandier, F., et al.: 'Observation of spectral gain narrowing in a high-order harmonic seeded soft-x-ray amplifier', *Phys. Rev. A.,* 81, 063833, 2010
8. Meng, L., et al.: 'Temporal coherence and spectral linewidth of an injection-seeded transient collisional soft x-ray laser', Opt. Express, 19, 12087, 2011
9. Benware, B., et al.: 'Demonstration of a High Average Power Tabletop Soft X-Ray Laser', *Phys. Rev. Lett.,* 81, 5804, 1998
10. Urbanski, L., et al.: 'Spectral linewidth of a Ne-like Ar capillary discharge soft-x-ray laser and its dependence on amplification beyond gain saturation', *Phys. Rev. A.,* 85, 033837, 2012
11. Guilbaud, O., et al.: 'Longitudinal coherence and spectral profile of a nickel-like silver transient soft X-ray laser', *Eur. Phys. J. D.,* 40, 125, 2006
12. Macchietto, C. D., et al.: 'Generation of millijoule-level soft-x-ray laser pulses at a 4-Hz repetition rate in a highly saturated tabletop capillary discharge amplifier ', *Opt. Lett.,* 24, 1115, 1999
13. Tomassetti, G. A., et al.: 'Toward a full optimization of a highly saturated soft-X-ray laser beam produced in extremely long capillary discharge amplifiers ', *Opt. Commun.,* 231, 403, 2004
14. Heinbuch, S., et al.: 'Demonstration of a desk-top size high repetition rate soft x-ray laser ', *Opt. Express.,* 13, 4050, 2005
15. Le Pape, S., et al.: 'Electromagnetic-Field Distribution Measurements in the Soft X-Ray Range: Full Characterization of a Soft X-Ray Laser Beam ', *Phys. Rev. Lett.,* 88, 183901, 2002
16. Marconi, M. C., et al.: 'Measurement of the Spatial Coherence Buildup in a Discharge Pumped Table-Top Soft X-Ray Laser', *Phys. Rev. Lett.,* 79, 2799, 1997
17. Liu,Y., et al.: 'Achievement of essentially full spatial coherence in a high-average-power soft-x-ray laser', *Phys. Rev. A.,* 63, 033802, 2001
18. Brewer, C. A., et al.: 'Single-shot extreme ultraviolet laser imaging of nanostructures with wavelength resolution', *Opt. Lett.,* 33, 518, 2008
19. Wachulak, P. W., et al.: 'Patterning of nano-scale arrays by table-top extreme ultraviolet laser interferometric lithography ', *Opt. Express.,* 15, 3465, 2007
20. Koch, J. A., et al.: 'Collisional redistribution effects on x‑ray laser saturation behavior', *AIP Conf. Proc.,* 332, 574–578, AIP, New York, 1994
21. Mocek,T., et al.: 'Plasma-based X-ray laser at 21 nm for multidisciplinary applications', *Eur. Phys. J. D.,* 54, 439–444, 2009
22. Calisti, A., et al.: 'Model for the line shapes of complex ions in hot and dense plasmas', *Phys. Rev. A.,* 42, 5433, 1990
23. Guilbaud, O., et al.: 'Fourier-limited seeded soft x-ray laser pulse', *Opt. Lett.,* 35, 1326, 2010

4.5 Temporal behaviour of GRIP transient XUV laser

4.5.1 Introduction

The experiment described in the scientific paper contained in this section was carried out at the LASERIX facility hosted at ENSTA-Palaiseau, in December 2010 and April 2011. It involved collaboration between our group and the groups of S. Bastiani at LULI (Palaiseau) and O. Guilbaud at LPGP/LASERIX. The Axis-Photonique X-ray Streak camera used for the study was provided by LULI.

A dedicated triggering beamline was implemented at LASERIX for the experiment. The schematic set-up is shown in Figure 4-5-1.

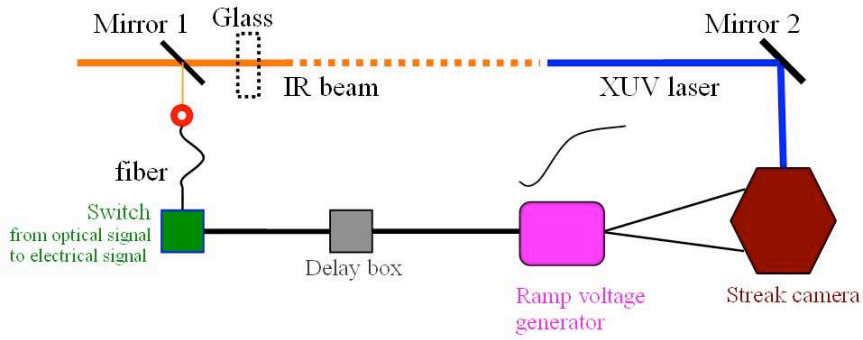

Figure 4-5-1. sketch of the streak camera triggering beamline

A small part of the infrared laser beam (E ~100μJ) is focused in an optical fiber and transmitted to the entrance of an optoelectronic integrator, the "switch Gonthier ". The (electric) output signal of the switch is then sent to the input of the Streak ramp voltage generator, which controls the sweeping of the photoelectrons produced at the photocathode by the photoelectrons. The synchronization was adjusted with a delay box.

The first experimental campaign in 2010 was devoted to a study of the temporal duration of the Ni-like Mo transient XUV laser over a wide range of pumping conditions. It is interesting to note that such a parameter-scan study, requiring hundreds of laser shots, was not possible when XUV lasers were generated with Nd:glass pump lasers, at a repetition rate of 1 or 2 shots per hour. On the other hand transient pumping is the only one among the different types of collisional excitation XUV lasers that offers possibilities to vary (to a certain extent) the output beam characteristics through the variation of the pumping parameters. This possibility could be interesting for certain applications. In the experiment presented in this section we have investigated the effect of two parameters on the XUV laser pulse duration: the duration of the short pump pulse, and the GRIP angle.

One of the main difficulty of using the ultrafast X-ray camera is to adjust the signal level incident on the photocathode within the small operating range, ie above the detection threshold and below the saturation, which leads to space-charge broadening effects. The dynamic range of the camera (ie the ratio between these two limits) is rather low: typically a factor 4. As explained in the following paper the signal level was carefully maintained below the saturation level by adjusting the focusing of the near-field image at the photocathode plane.

The fact that saturation was not affecting our measurements was also checked a posterior while analysing the data. For all shots, the measured pulse duration was plotted as a function of the peak intensity of the XUV laser pulse in the image, as shown in Figure 4-5-2. One can see that all the measured signal intensities lie within the dynamic range of 4 and that there is not systematic increase of the duration for larger intensity, which would happen if space-charge broadening was affecting the measurement.

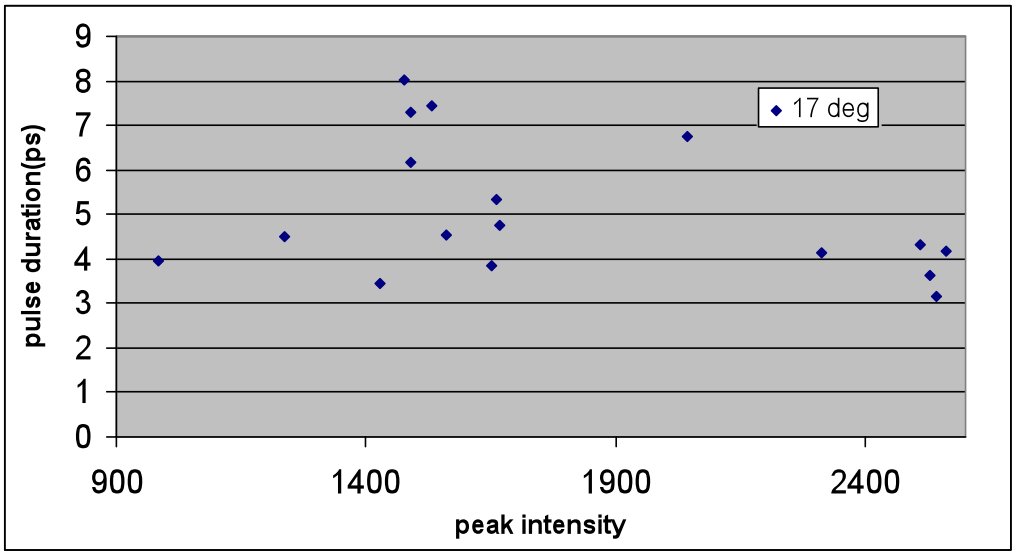

Figure 4-5-2. Compilation of measured pulse duration versus peak signal intensity

The second experimental campaign in 2011 was initially devoted to repeat the same measurements but while operating the streak camera in the accumulated mode, rather than single-shot mode. By allowing to operate the Streak camera at a low single-shot signal level, the accumulated mode leads an increased dynamical range. However due to several technical problems this experiment was not successful. As mentioned in chapter 3, we used this opportunity to carry out an accurate determination of the temporal resolution of the Streak camera using femtosecond high-order harmonic pulses, which were also available at

LASERIX. It was the first time that the resolution of the LULI Streak camera was directly measured in the XUV range. The measured temporal resolution of T_r of 2.0±0.18 ps is about 2 times larger than what was considered until now, following the specifications from the manufacturer.

4.5.2 Experimental results

APPLIED PHYSICS LETTERS **101**, 141125 (2012)

Temporal characterization of a picosecond extreme ultraviolet laser pumped in grazing incidence

L. Meng,[1] A.-C. Bourgaux,[2] S. Bastiani-Ceccotti,[2] O. Guilbaud,[3,4] M. Pittman,[3] S. Kazamias,[3,4] K. Cassou,[3,4] S. Daboussi,[3,4] D. Ros,[3,4] and A. Klisnick[1]
[1]*ISMO, Bât. 350, CNRS, Université Paris-Sud, 91405 Orsay, France*
[2]*LULI, École Polytechnique, CNRS, CEA, UPMC, 91128 Palaiseau Cedex, France*
[3]*LASERIX, Université Paris-Sud 11, 91405 Orsay, France*
[4]*LPGP, CNRS, Université Paris-Sud, 91405 Orsay, France*

(Received 5 July 2012; accepted 24 September 2012; published online 5 October 2012)

We report an experimental study of the temporal duration of a transient pumping extreme ultraviolet (XUV) laser emitted at 18.9 nm, using an ultrafast x-ray streak camera. We have investigated the shot-to-shot reproducibility of the pulse duration, as well as its behaviour as a function of several pumping parameters. Our results show that the pulse duration increases slowly with the pump pulse duration, in agreement with previous observations performed in a different geometry. The angle of the pump laser relative to the target surface also affects the XUV laser duration in a measurable way.
 [http://dx.doi.org/10.1063/1.4757878]

Scientific paper published in *Appl. Phys. Lett. 101, 141125 (2012)*

Temporal characterization of a picosecond extreme ultraviolet laser pumped in grazing incidence

L. Meng,[1] A.-C. Bourgaux,[2] S. Bastiani-Ceccotti,[2] O. Guilbaud,[3,4] M. Pittman,[3] S. Kazamias,[3,4] K. Cassou,[3,4] S. Daboussi,[3,4] D. Ros,[3,4] and A. Klisnick[1]
[1]*ISMO, Bât. 350, CNRS, Université Paris-Sud, 91405 Orsay, France*
[2]*LULI, École Polytechnique, CNRS, CEA, UPMC, 91128 Palaiseau Cedex, France*
[3]*LASERIX, Université Paris-Sud 11, 91405 Orsay, France*
[4]*LPGP, CNRS, Université Paris-Sud, 91405 Orsay, France*

(Received 5 July 2012; accepted 24 September 2012; published online 5 October 2012)

We report an experimental study of the temporal duration of a transient pumping extreme ultraviolet (XUV) laser emitted at 18.9 nm, using an ultrafast x-ray streak camera. We have investigated the shot-to-shot reproducibility of the pulse duration, as well as its behaviour as a function of several pumping parameters. Our results show that the pulse duration increases slowly with the pump pulse duration, in agreement with previous observations performed in a different geometry. The angle of the pump laser relative to the target surface also affects the XUV laser duration in a measurable way.
 [http://dx.doi.org/10.1063/1.4757878]

Plasma-based extreme ultraviolet (XUV) lasers, pumped in the transient collisional excitation (TCE) regime[1] by picosecond, chirped-pulse amplification (CPA) pump lasers, provide a useful tool for fundamental studies in many different areas. Recent demonstrations include interferometric diagnostics of dense plasmas,[2] single-shot holography of nanostructures,[3] high-resolution microscopy of masks for extreme ultraviolet lithography,[4] and XUV irradiation of clusters.[5] For most of these applications, an accurate knowledge of the XUV pulse duration is essential.

Several measurements of the pulse duration of TCE XUV lasers have been previously conducted by different groups. All these works used an ultra-fast x-ray streak camera to achieve picosecond temporal resolution.[6,7] The first demonstration of a picosecond XUV laser was reported for a Ni-like Ag laser[8,9] at 13.9 nm. A systematic study of the role of the duration of the pump laser was then carried out by Dunn[10] for a Ni-like Pd laser at 14.7 nm. In these works, pumping of the XUV laser was achieved by irradiating a preformed plasma with a CPA picosecond pulse at near-normal incidence. More recently, a significant improvement of the efficiency of TCE pumping has been obtained by irradiating the plasma under a grazing incidence angle of ~10°–20°, leading to a generation of so-called grazing incidence angle pumping (GRIP) XUV lasers.[11–14] The GRIP geometry, which was first described and demonstrated in,[11] allows to select the electron density at which the pump laser is absorbed and the gain zone is created. Ni-like Ag and Cd lasers pumped in the GRIP geometry were demonstrated by the Colorado State University (USA) group, and a pulse duration of typically 5 ps was measured for both elements, with a fixed GRIP angle of 23° and a pump duration of 6.7 ps.[15] Finally, a significantly shorter pulse duration of 1.13 ps was reported by the same group for a Ne-like Ti laser ($\lambda = 32.6$ nm) pumped under 23° GRIP angle, and injection-seeded with a high-order harmonic (HH) pulse. This is actually the shortest pulse demonstrated to date for a plasma-based XUV laser.

In this paper, we explore further the temporal behaviour of GRIP systems, by investigating the effect of the pump pulse duration, and of the grazing incidence angle on the measured pulse duration of the XUV laser. Both these parameters have a direct influence on the spatial temporal behaviour of the plasma in the gain region and hence can potentially provide a method to control or vary the duration of the XUV laser pulse. Our work focus on the transient Ni-like Mo XUV laser ($4d\ ^1S_0 \rightarrow 4p\ ^1P_1$ transition at = 18.9 nm), which was recently implemented at the LASERIX user facility (Palaiseau, France) and optimized for several applications.[16] Our works aims at characterizing the temporal duration of the delivered XUV pulse, as well as its shot-to-shot reproducibility and sensitivity to the experimental pumping conditions. We present the results of our measurements and we discuss them together with previously measured data available from the literature.

The Mo XUV laser was generated by irradiating a 4 mm long molybdenum slab target with a sequence of infrared (IR) laser pulses delivered by a Ti:Sa laser. First, a long (uncompressed) 500 ps pulse was focused onto the target at normal incidence by a combination of spherical and cylindrical lenses to form a 4 mm × 70 μm line focus, with typical intensity 5×10^{11} W/cm^2. After an optimized delay (590 ps in our experiment), a short (compressed) picosecond pulse was focused to a 4 mm × 50 μm line focus using an off-axis spherical mirror and irradiated the preformed plasma with intensities ranging from 0.6 to 12×10^{14} W/cm^2. The XUV laser beam amplified along the plasma column was reflected by a spherical multilayer mirror which formed the magnified (M = 6), time-integrated image of the output plane of the source (near-field image). Using a translatable flat multilayer mirror, this image could be formed either onto a CCD camera or onto the entrance slit of the streak camera (Axis Photonique) equipped with a KBr photocathode (Luxel).

A temporal resolution T_r of 2.0 ± 0.18 ps was determined *in-situ* by measuring the duration of a HH femtosecond pulse, while the sweep speed was calibrated by generating a double-pulse XUV laser.[17] Aluminium filters with variable thickness (0.3–2 μm) were used to attenuate the XUV laser signal. Finer adjustment of the signal level

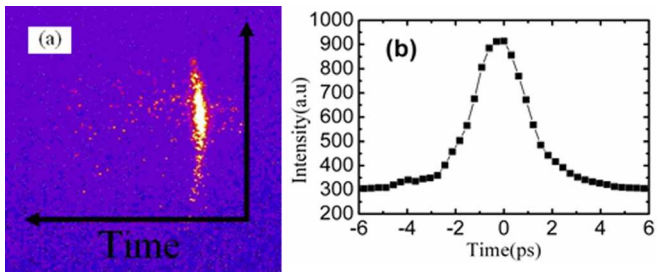

FIG. 1. Left: example of time-resolved XUV laser signal recorded by the Streak camera, Right: Lineout versus time, after correction from distortion and integration over the vertical size of the pulse.

was obtained by adjusting the size of the XUV laser beam spot at the photocathode slit with a slight translation of the imaging mirror. The size of the spot was increased until we observed that space charge broadening had no appreciable effect on the temporal measurements.

Figure 1 shows a typical example of time-resolved image. The curved shape of the signal, which is due to instrumental distortion,[18] was corrected before quantitative analysis of the pulse duration. The right part of Fig. 1 shows a lineout of the corrected image along the temporal axis. The FWHM duration T_m measured from such a plot was then deconvolved from the finite temporal resolution T_r to yield the actual duration T_{XUV} of the Ni-like Mo laser, assuming a quadratic relation: $T^2_{XUV} = T^2_m - T^2_r$.

The measurement of the Ni-like Mo laser pulse duration was carried out over a broad range of pumping conditions. The grazing angle of the short pump pulse relative to the target surface was varied from 17° to 23°, by adjusting the incidence angle at the focussing spherical mirror. This variation of the GRIP angle induced a variation of up to 40% in the length of the line focus (4.2 mm–6.3 mm) and a corresponding decrease of the pump intensity. The grazing angle also controls the speed of the travelling-wave irradiation.[14] In the explored range, however, the speed was always very close to the speed of light (1.06 to 1.09c). Finally, the duration of the short pump pulse beam was varied between 0.75 ps and 10 ps (FWHM) by adjusting the distance between the compressor gratings. Since the energy was kept constant, the increase of the pulse duration led to a corresponding decrease of the pump intensity. For each pumping condition, three to five successive measurements were performed to assess the shot-to-shot reproducibility of the XUV laser pulse. The results of this study are summarized in Figs. 2(a)–2(c), which show the measured XUV laser duration as a function of the pump laser duration for three different GRIP angles. Each data point corresponds to the average over individual measurements and the error bar stands for their standard deviation. One can see that for all pumping conditions the duration of the XUV laser pulse does not vary from shot-to-shot by more than ±0.8 ps.

Also shown in Figs. 2(a) and 2(c) are data measured by other authors for the same GRIP angle. At 17° (Fig. 2(a)), the duration of 1.7 ± 1 ps measured by Booth *et al.* in Ref. 19 in a Ni-like Mo laser pumped with a 0.25 ps pump pulse appears somewhat shorter than what could be extrapolated from our measurements. At 23° (Fig. 2(c)), our data agree well with the measurements reported by Larrotonda *et al.* in Ref. 15 in Ni-like Ag and Cd for the longest pump pulses, but they seem to disagree for the shortest pump pulses where we measure shorter durations (~3 ps in our case, instead of ~5 ps in Ref. 15).

For the three investigated GRIP angles, the XUV pulse durations measured in our experiment increase slowly with the duration of the short pump pulse. While the duration of short pump pulse is increased by 13 times, the duration of the XUV pulse increases only by a factor of 2–3. Such a behaviour was already observed by Dunn and collaborators in a similar study performed with a transient 14.7 nm Ni-like Pd XUV laser pumped in near-normal incidence geometry,[10] as can be seen in Figure 2(d). Their observation was found in good agreement with numerical simulations performed in the same group,[20] where the duration of the XUV laser pulse was found to follow closely the variation of the plasma electron temperature. In our experiment, the shortest duration, of

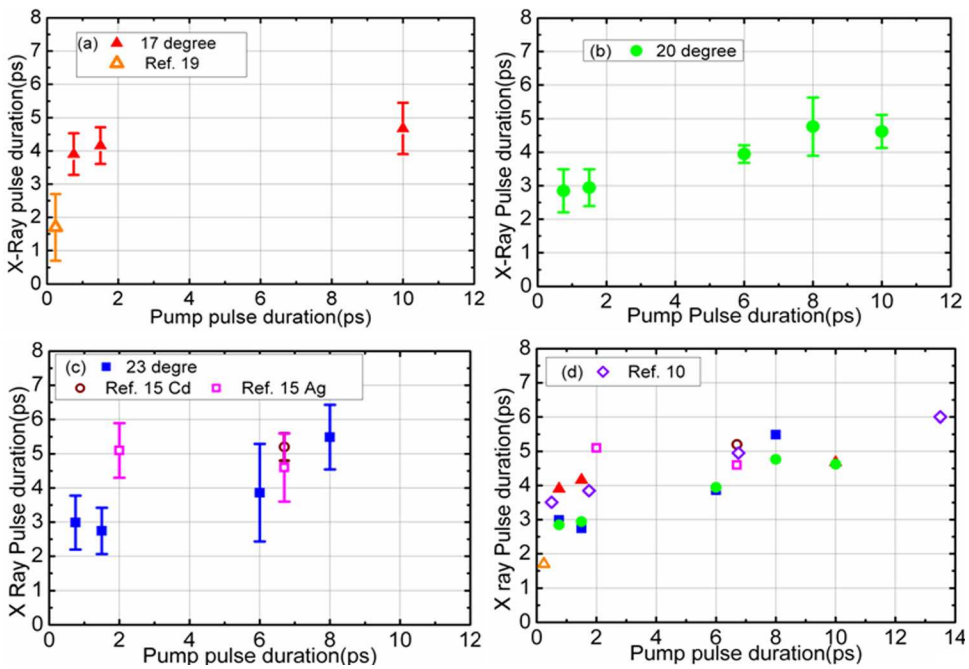

FIG. 2. Measured duration (FWHM) of the Ni-like Mo laser as a function of the short pump pulse duration, for different values of the GRIP angle: (a) 17°; (b) 20°; (c) 23°. Also shown are data measured by other authors, for a GRIP angle of 17° (Booth *et al.*[19]) and 23° (Larrotonda *et al.*[15]); (d) Compilation of the results of (a)–(c), together with measurements from Ref. 10 in a Pd laser pumped in near-normal incidence geometry. The data measured for different pumping angles exhibit a similar linear increasing trend with the pump pulse duration.

2.8 ± 0.6 ps, is obtained for a pump pulse duration of 750 fs and a GRIP angle of 20°.

By comparing the increasing trend of the XUV pulse duration versus the short pump pulse in Figs. 2(a)–2(c), it can be seen that the GRIP angle has also a small effect: the slope of growth appears to be steeper for the larger GRIP angle, and shorter durations are measured. This could be explained by a more effective thermal conduction cooling towards the colder overdense plasma when the GRIP angle, hence the electron density in the gain zone, are larger. However, this will require to be confirmed by dedicated numerical hydrosimulations that include the description grazing incidence irradiation, which is beyond the present work.

More generally, we note that the different measurement data compiled in Figure 2(d) are relatively more scattered when the duration of the pump laser is short, i.e., when the duration of the XUV laser is the shortest. Although the observed discrepancies might be real, they also could at least partially result from other spurious effects, like the saturation of the streak camera at high signal level, or the detuning of the travelling wave irradiation from the speed of light.[20] Both these effects would lead to an apparent broadening of the measured pulse, and they would proportionally affect more the shortest pulse durations.

In conclusion, we have investigated the effect of the duration and the GRIP angle of the short pump pulse on the duration of the Mo XUV lasers. Our results show that the XUV laser duration increase slowly with the pump pulse duration. For the shortest pump pulse, the duration of the XUV laser pulse reaches slightly shorter values when GRIP angle is larger, within the explored range.

This work was partially supported by the SFINX/LASERLAB project from the EC 7th Framework Programme under Grant Agreement No. 228334. The authors wish to gratefully acknowledge the technical support of J. Albrecht and E. Veuillot at LULI, J. Demailly at LASERIX, and C. Le Bris at ISMO.

[1]S. Kazamias, K. Cassou, D. Ros, F. Plé, G. Jamelot, A. Klisnick, O. Lundh, F. Lindau, A. Persson, C. G. Wahlström, S. de Rossi, D. Joyeux, B. Zielbauer, D. Ursescu, and T. Kühl, Phys. Rev. A. **77**, 033812 (2008).
[2]J. Filevich, J. J. Rocca, M. C. Marconi, R. F. Smith, J. Dunn, R. Keenan, J. R. Hunter, S. J. Moon, J. Nilsen, A. Ng, and V. N. Shlyaptsev, Appl. Opt. **43**, 3938 (2004).
[3]H. T. Kim, I. J. Kim, C. M. Kim, T. M. Jeong, T. J. Yu, S. K. Lee, J. H. Sung, J. W. Yoon, H. Yun, S. C. Jeon, I. W. Choi, and J. Lee, Appl. Phys. Lett. **98**, 121105 (2011).
[4]F. Brizuela, Y. Wang, C. A. Brewer, F. Pedaci, W. Chao, E. H. Anderson, Y. Liu, K. A. Goldberg, P. Naulleau, P. Wachulak, M. C. Marconi, D. T. Attwood, J. J. Rocca, and C. S. Menoni, Opt. Lett. **34**, 271 (2009).
[5]S. Namba, N. Hasegawa, M. Kishimoto, M. Nishikino, K. Takiyama, and T. Kawachi, Phys. Rev. A **84**, 053202 (2011).
[6]M. M. Murnane, H. C. Kapteyn, and R. W. Falcone, Appl. Phys. Lett. **56**, 1948 (1990).
[7]J. Feng, K. Engelhorn, B. I. Cho, H. J. Lee, M. Greaves, C. P. Weber, R. W. Falcone, H. A. Padmore, and P. A. Heimann, Appl. Phys. Lett. **96**, 134102 (2010).
[8]A. Klisnick, J. Kuba, D. Ros, R. Smith, G. Jamelot, C. Chenais-Popovics, R. Keenan, S. J. Topping, C. L. S. Lewis, F. Strati, G. J. Tallents, D. Neely, R. Clarke, J. Collier, A. G. MacPhee, F. Bortolotto, P. V. Nickles, and K. A. Janulewicz, Phys. Rev. A **65**, 033810 (2002).
[9]Y. Abou-Ali, G. J. Tallents, M. Edwards, R. E. King, G. J. Pert, S. J. Pestehe, F. Strati, R. Keenan, C. S. Lewis, S. Topping, O. Guilbaud, A. Klisnick, D. Ros, R. Clarke, D. Neely, M. Notley, and A. Demir, Opt. Commun. **215**, 397 (2003).
[10]J. Dunn, R. F. Smith, R. Shepherd, R. Booth, J. Nilsen, J. R. Hunter, and V. N. Shlyaptsev, Proc. SPIE **5197**, 51 (2003).
[11]R. Keenan, J. Dunn, P. K. Patel, D. F. Price, R. F. Smith, and V. N. Shlyaptsev, Phys. Rev. Lett. **94**, 103901 (2005).
[12]B. M. Luther, Y. Wang, M. A. Larotonda, D. Alessi, M. Berrill, M. C. Marconi, J. J. Rocca, and V. Shlyaptsev, Opt. Lett. **30**, 165 (2005).
[13]Y. Wang, M. A. Larotonda, B. M. Luther, D. Alessi, M. Berrill, J. J. Rocca, and V. N. Shlyaptsev, Phys. Rev. A **72**, 053807 (2005).
[14]J. J. Rocca, Y. Wang, M. A. Larotonda, B. M. Luther, M. Berrill, and D. Alessi, Opt. Lett. **30**, 2581 (2005).
[15]M. A. Larotonda, Y. Wang, M. Berrill, B. M. Luther, and J. J. Rocca, Opt. Lett. **31**, 3043 (2006).
[16]D. Ros, K. Cassou, B. Cros, S. Daboussi, J. Demailly, O. Guilbaud, S. Kazamias, J.-C. Lagron, G. Maynard, O. Neveu, M. Pittman, B. Zielbauer, D. Zimmer, T. Kuhl, S. Lacombe, E. Porcel, M.-A. du Penhoat, P. Zeitoun, and G. Mourou, Nucl. Instrum. Methods Phys. Res. A **653**, 76 (2011).
[17]L. Meng, A.-C. Bourgaux, S. Bastiani-Ceccotti, O. Guilbaud, M. Pittman, S. Kazamias, K. Cassou, S. Daboussi, D. Ros, and A. Klisnick, Proc. SPIE **8140**, 81401A (2011).
[18]C. Bonté, M. Harmand, F. Dorchiesa, S. Magnan, V. Pitre, J.-C. Kieffer, P. Audebert, and J.-P. Geindre, Rev. Sci. Instrum. **78**, 043503 (2007).
[19]N. Booth, M. H. Edwards, Z. Zhai, G. J. Tallents, T. Dzelzainis, C. L. S. Lewis, A. Behjat, Q. Dong, S. J. Wang, D. Neely, P. Foster, and M. Streeter, Eur. Phys. J. Spec. Top. **175**, 153 (2009).
[20]V. N. Shlyaptsev, J. Dunn, S. Moon, R. Smith, R. Keenan, J. Nilsen, K. B. Fournier, J. Kuba, A. L. Osterheld, J. J. G. Rocca, B. M. Luther, Y. Wang, and M. C. Marconi, Proc SPIE **5197**, 221 (2003).

4.5.3 Summary

Our experimental study shows that the pulse duration of a transient XUV laser varies slowly with the pump pulse duration, leading to a limited range of variation of ~3ps to 6 ps in the investigated domain. The pulse duration has a good shot-to-shot reproducibility.

The observed effect of the GRIP angle on the XUV laser pulse duration is less clear. Our measurements suggest that the increase of the pulse duration with the pump laser duration is slightly steeper when the GRIP angle is increased (see Fig 2 in the preceding paper). Larger GRIP angles are predicted to lead to a higher electron density in the gain zone, i.e. the gain zone is shifted towards the (cold) target surface. This could lead to a more efficient plasma cooling after the pump laser pulse and hence to a shortening of the gain lifetime. This effect would be proportionally more significant when the pulse duration is short and thus lead to the observed steepening of the slope. Further investigation, as well as numerical simulations would be required to confirm this trend.

4.6 Summary and conclusions of the experimental study

During my Ph.D thesis work, I have investigated three types of collisional XUV lasers: (1) transient Ni-like Mo XUV laser in seeded and ASE modes, (2) capillary-discharge Ne-like Ar XUV laser and (3) quasi-steady state Ne-like Zn XUV laser (ASE mode). The Optical Field Ionization (OFI) XUV laser is not discussed in the present work, but it is very interesting to include it in our comparison.

Table 4-6-1 summarizes the parameters of these different XUV lasers, including those investigated during my thesis. Among the four types of existing collisional XUV lasers, which are now operated at saturation in laboratories, we can summarize the following features concerning in particular their spectral properties:

(1) Transient and OFI pumping leads to short pulse XUV lasers in the few picosecond range. Both lasers were already operated in the seeded mode, using HHG radiation as a seed. In both cases the heating of plasma free electrons by the laser is too short to allow a significant transfer of kinetic energy to the heavy ions before lasing occurs. As a result the ionic temperature is significantly lower than the electron temperature. Because in OFI XUV lasers both ionic temperature and electron density are low, their spectral width is the smallest among the four types of collisional XUV lasers. As a result the Fourier-transform limit pulse duration is the largest, $\tau_{FL} \sim 5$ ps.

(2) Transient XUV lasers operate at higher N_e and T_i than OFI XUV lasers. As a result their linewidth is ~2 to 3 times larger. The Fourier-transform limit duration is found to be of ~2 ps. We note that compared to the other pumping regimes, the transient pumping offers a broad range of parameters that can be used to vary the plasma parameters in the gain zone. For example the GRIP angle could be used to vary the electron density and thus to enlarge the linewidth (i.e. reduce τ_{FL}). A first attempt to investigate this effect was carried out at LASERIX during my thesis but, due to technical problems on the stability of the XUV laser, the results were inconclusive and were not included in the present manuscript.

(3) At LASERIX we have investigated the duration of the transient Ni-like Mo XUV laser operated in ASE. The shortest duration measured is 2.8 ps, very close to the coherence time. We have shown that longer pulse duration can be obtained by increasing the duration of the main pump pulse. The relationship is linear but the slope is relatively small, of the order of 0.25.

(4) Quasi-steady state pumping leads to XUV lasers that operate on a longer timescale: ~150 ps for the Ne-like Zn laser and ~2 ns for the capillary-discharge laser. In both cases the ion temperature is closer or even equal to the electron temperature. As a result the Doppler broadening has a significant contribution to the intrinsic line profile. In particular the Doppler broadening dominates the profile of the capillary-discharge XUV laser, since the electron density is low and the collisional broadening is small. However saturation rebroadening remains weak and it could not be observed in our experiment. The Fourier-transform limit duration is similar to the transient pumping case, of the order of 2 ps. However this duration is much smaller than the duration of the ASE XUV laser, so that seeding of this type of laser would lead to a dramatic shortening of the output pulse.

(5) The QSS Ne-like Zn XUV laser operates at both high N_e and high T_i. As a result this laser exhibit the largest bandwidth among the existing collisional XUV lasers. Although our measurements should still be considered as preliminary, they indicate that duration significantly below 1 ps should be reached in the seeded mode.

(6) One can see in Table 4-6-1 that collisional XUV lasers are characterized by a remarkably large temporal coherence length, between 200 um and 1.6 mm. This feature is related to their extremely narrow bandwidth. Although this feature currently limits the duration to the picosecond range, it can be of interest for several applications requiring high temporal coherence, such as interferometric lithography, or coherent diffraction imaging.

Type of XUV laser	Optical-field ionization pumping, gas target [3, 9, 16-18]	Transient pumping, solid target [5, 19-21]	Quasi-steady state pumping, capillary discharge [23-26]	Quasi-steady state pumping, solid target [1, 14, 27]
Element	Ni-like Kr	Ni-like Mo	Ne-like Ar	Ne-like Zn
Wavelength (nm)	32.8	18.9	46.9	21.2
Plasma length	6 mm	4 mm	36 cm	3 cm * 2
Pumping configuration	CPA Ti:Sa laser 600mJ/35fs Krypton 30 mTorr	CPA Ti:Sa laser prepulses (normal incidence): 45 mJ/210 ps + 420 mJ/210ps (delay 1.5 ns) main pulse (GRIP 23°): 1 J/3.3 ps (delay 500 ps)	electrical pulse with a 10%–90% rise time of 44 ns, 21-kA peak amplitude Argon 440 mTorr	Iodine laser prepulse 2J/300ps + main pulse 420J/300ps (delay 10 ns) double-pass with half-cavity
Repetition rate	10 Hz	5 Hz	7 Hz	2 shots/hour
Output energy	0.7 uJ	1 μJ (ASE); ~75 nJ (seeded)	up to 1 mJ	up to10 mJ
N_e [cm^{-3}]	~ 10^{18}	~1-3*10^{20}	~2*10^{18}	2-5*10^{20}
T_e [eV]	450	250-500	~100	150-200
T_i [eV]	6	~ 50	~ 100	200-300
Calc. homogeneous $\Delta\lambda_H$ (mÅ)	5	9.5	4	11-24
Calc. inhomog.$\Delta\lambda_D$ (mÅ)	7	14.3	53.5	24-27
L_c (um)	1500-1650	240-300 (seeded); ~320 (ASE)*	~690	210-300
τ_c (ps)	5.1-5.5	0.8-1.0(seeded); ~1.1(ASE)*	~2.3	0.7-1
$\Delta\lambda$ (mÅ)	2.7-3.2	2.6-3.4 (seeded); 2.4(ASE)*	~16.6	7.7-11.2
$\Delta\nu$ (10^{11} Hz)	0.75-0.89	2.2-2.9 (seeded); 2(ASE)*	~2.3	5.1-7.5
$\Delta\lambda/\lambda$ (10^{-5})	0.82-0.98	1.4-1.8 (Seeded); 1.3(ASE)*	3-4	3.6-5.3
τ_{FL}(ps)	4.9-5.9	1.5-2.0 (seeded); 2.2(ASE)	~2	0.6-0.9
actual τ_{XUVL}(ps)	~5 ps	2.8 ps (ASE) [22]	1.2-1.8 ns	~150 ps

Table 4-6-1. Typical parameters of collisional excited XUV laser. The data (experiment and simulation) which were obtained during this thesis are indicated in blue. The value with "*" stands for the quadratic definition results.

References

1. B. Rus, T. Mocek, A. R. Prag, M. Kozlova, G. Jamelot, A. Carillon, D. Ros, D. Joyeux, and D. Phalippouet, "Multimillijoule, highly coherent x-ray laser at 21 nm operating in deep saturation through double-pass amplification", Phys. Rev. A., 66, 063806, (2002);

2. Y. Wang, E. Granados, M. A. Larotonda, M. Berrill, B. M. Luther, D. Patel, C. S. Menoni, and J. J. Rocca "High-Brightness Injection-Seeded Soft-X-Ray-Laser Amplifier Using a Solid Target" Phys. Rev. Lett., vol 97, p. 123901 (2006) ;

3. Ph. Zeitoun, G. Faivre, S. Sebban, T. Mocek, A. Hallou, M. Fajardo, D. Aubert, Ph. Balcou, F. Burgy, D. Douillet, S. Kazamias, G. De Lachèze-Murel, T. Lefrou, S. Le Pape, P. Mercère, H. Merdji, A.S. Morlens, J.P. Rousseau, C. Valentin, "A high-intensity highly coherent soft X-ray femtosecond laser seeded by a high harmonic beam", Nature, Vol 431, p. 426, (2004);

4. J.J. Rocca, V. Shlyaptsev, F.G. Tomasel, O. D. Cortazar, D. Hartshorn, and J. L. A. Chilla, "Demonstration of a Discharge Pumped Table-Top Soft-X-Ray Laser", Phys. Rev. Lett, Vol 73, p. 2192 (1994) ;

5. Y. Wang, E. Granados, F. Pedaci, D. Alessi, B. Luther, M. Berrill, and J.J. Rocca, "Phase-coherent, injection-seeded, table-top soft-X-ray lasers at 18.9 nm and 13.9 nm", Nature Photonics 2, 94 (2008);

6. Jeffrey A. Koch, Brian J. MacGowan, Luiz B.Da Silva, Dennis L. Matthews, James H. Underwood, Philip J. Batson, Richard W. Lee, Richard A. London, and Stan Mrowka, "Experimental and theoretical investigation of neonlike selenium x-ra3t laser spectral linewidths and their variation with amplification", Physical Review A 50, 1877 (1994);

7. Pert, G. J., "Output characteristics of amplified-stimulated-emission lasers",J. Opt. Soc. Am. B, 11, 1425, (1994);

8. A. Klisnick, O. Guilbaud, D. Ros, K. Cassou, S. Kazamias, G. Jamelot, J.-C. Lagron, D. Joyeux, D. Phalippou, Y. Lechantre, M. Edwards, P. Mistry, G.J. Tallents, "Experimental study of the temporal coherence and spectral profile of the 13.9 nm transient X-ray laser", J. Quant. Spectr. Rad. Trans. 99, 370 (2006);

9. F. Tissandier, S. Sebban, M. Ribiere, J. Gautier, Ph. Zeitoun, G. Lambert, A. Barszczak Sardinha, J.-Ph. Goddet, F. Burgy, T. Lefrou, C. Valentin, and A. Rousse, O. Guilbaud and A. Klisnick, J. Nejdl and T. Mocek, G. Maynard, "Observation of spectral gain narrowing

in a high-order harmonic seeded soft-x-ray amplifier", PHYSICAL REVIEW A 81, 063833 (2010);

10. J. Habib, A. Klisnick, O. Guilbaud, D. Joyeux, B. Zielbauer, S. Kazamias, D. Ros, F. de Dortan, M. Pittman et al., "Temporal Coherence and Spectral Line Shape of a GRIP Transient X-Ray Laser", X-Ray Lasers 2008, Springer Proceedings in Physics, Vol. 130, p. 115 (2009);

11. Meng LM, Alessi D, Guilbaud O, Wang Y, Berrill M, Luther BM, Domingue SR, Martz DH, Joyeux D, De Rossi S, Rocca JJ, Klisnick A, "Temporal coherence and spectral linewidth of an injection-seeded transient collisional soft x-ray laser", Opt. Expr. 19, 12087 (2011);

12. L. Urbanski ; L. M. Meng ; M. C. Marconi ; M. Berril ; O. Guilbaud ; A. Klisnick ;J. J. Rocca, " Line width measurement of a capillary discharge soft X-ray laser ", Proc. SPIE 8140, (2011) ;

13. http://www.laserlab-europe.eu/;

14. B. Rus, "Pompage collisionnel du zinc néonoïde: laser X à 21.2 nm; Saturation, Polarisation, Cohérence des lasers X-UV", Thèse de Doctorat, Orsay (1995);

15. Dunn, J., Smith, R. F., Shepherd, R., Booth, R., Nilsen, J., Hunter, J. R. and Shlyaptsev, V. N., "Temporal characterization of a picosecond-laser-pumped x-ray laser for applications," Proc. SPIE 5197, (2003);

16. S. Sebban, T. Mocek, D. Ros, L. Upcraft, Ph. Balcou, R. Haroutunian, G. Grillon, B. Rus, A. Klisnick, A. Carillon, G. Jamelot, C. Valentin, A. Rousse, J. P. Rousseau, L. Notebaert, M. Pittman, and D. Hulin, "Demonstration of a Ni-Like Kr Optical-Field-Ionization Collisional Soft X-Ray Laser at 32.8 nm", Phys. Rev. Lett., Vol 89, p. 253901 (2002) ;

17. J. P. Goddet, "Etude et développements des sources xuv par injection d'harmoniques", Thèse de doctorat de l'école Polytechnique (2009);

18. T. Mocek, S. Sebban, I. Bettaibi, L.M. Upcraft, P. Balcou, P. Breger, P. Zeitoun, S. Le pape, D. Ros, A. Klisnick, A. Carillon, G. Jamelot, B. Rus, J. F. Wyart, "Characterization of collisionally pumped optical-field-ionization soft X-ray lasers", Appl. Phys. B 78, 939–944 (2004);

19. J. Nilsen, Y.Li, J. Dunn, T.W. Barbee, Jr., and A.L. Osterheld. "Modeling and demonstration of a saturated Ni-like Mo X-ray laser", 7th international Conference on X-ray lasers, Saint-Malo, France, (2000) ;

20. R. Keenan, J. Dunn, V. N. Shlyaptsev, R. F. Smith, P. K. Patel, D. F. Price, "Efficient Pumping Schemes for High Average Brightness Collisional X-ray Lasers", SPIE, San Diego, (2003);

21. Y. ochi, T. Kawachi, N. hasegawa, A. sasaki, K. nagashima, K. sukegawa, M. kishimoto, M. tanaka, M. nishikino, M. kado, "Measurement of temporal durations of transient collisional excitation X-ray lasers", Appl. Phys. B 78, 961–963 (2004);

22. L. Meng, A.-C. Bourgaux, S. Bastiani-Ceccotti, O. Guilbaud, M. Pittman, S. Kazamias, K. Cassou, S. Daboussi, D. Ros, and A. Klisnick, "Temporal characterization of a picosecond extreme ultraviolet laser pumped in grazing incidence", APPLIED PHYSICS LETTERS 101, 141125 (2012);

23. L. Urbanski, M. C. Marconi, L. M. Meng, M. Berrill, O. Guilbaud, A. Klisnick, and J. J. Rocca, "Spectral linewidth of a Ne-like Ar capillary discharge soft-x-ray laser and its dependence on amplification beyond gain saturation", PHYSICAL REVIEW A 85, 033837 (2012);

24. B. R. Benware, C. D. Macchietto, C. H. Moreno, and J. J. Rocca, "Demonstration of a high average power tabletop soft X-ray laser", Phys. Rev. Lett., vol 81, p. 5804, (1998);

25. C. D. Macchietto, B. R. Benware, and J. J. Rocca, "Generation of millijoule-level soft-x-ray laser pulses at a 4-Hz repetition rate in a highly saturated tabletop capillary discharge amplifier", Opt. Lett. 24, 1115 (1999);

26. S. Heinbuch, M. Grisham, D. Martz, and J. J. Rocca, "Demonstration of a desk-top size high repetition rate soft x-ray laser ", Opt. Express 13, 4050 (2005);

27. T. Mocek, B. Rus, M. Kozlová, J. Polan, P. Homer, K. Jakubczak, M. Stupka, D. Snopek, J. Nejdl, M.H. Edwards, D.S. Whittaker, G.J. Tallents, P. Mistry, G.J. Pert, N. Booth, Z. Zhai, M. Fajardo, P. Zeitoun, J. Chalupský, V. Hájková, and L. Juha, "Plasma-based X-ray laser at 21 nm for multidisciplinary applications", Eur. Phys. J. D, 54, 439 – 444 (2009).

Conclusion

In this thesis we have investigated the spectral and temporal properties of three types of plasma-based XUV lasers pumped by collisional excitation in different regimes. Our goal was to characterize the temporal coherence and corresponding spectral width as well as to investigate the behaviour in the saturation regime. This behaviour is strongly related to the nature of the intrinsic line profile: homogeneous, inhomogeneous or a combination of both. The other motivation of our work was to compare the capabilities of the different XUV lasers in supporting amplification of femtosecond pulses, by enlarging the bandwidth. The shortest duration (Fourier-transform limit) that can be reached by the laser pulse is related to its spectral width.

In chapter 2 I have presented numerical simulations using a radiative transfer code to calculate the spectral profile and width of the amplified laser line. I have shown that the nature of the XUV laser line profile strongly depends on the values of the local plasma parameters in the gain zone, which are very different in the three types of XUV lasers that we have investigated. Saturation rebroadening is observed only when the inhomogeneous broadening dominates the intrinsic profile. Such conditions correspond to a low electron density ($\sim 10^{19}$ cm^{-3}) and a high ionic temperature (200 eV). Such conditions are similar to the ones encountered in capillary-discharge XUV lasers. However saturation rebroadening was not observed in our experiment described in chapter 4. Recent calculations performed by the PIIM group (A.Calisti et al.) suggest that ionic correlations could play a significant role in homogenizing the spectral profiles of XUV laser lines, thus preventing any saturation rebroadening to occur. The other important result obtained from our simulations is that, whatever the shape of the intrinsic profile (Lorentzian or Gaussian), the shape of the amplified profile is Gaussian.

In chapter 4 I have presented the results of my experimental work. Using the same wavefront-division interferometer we have measured the temporal coherence of three different collisional XUV lasers: transient pumping in Ni-like Mo in seeded and ASE modes, capillary discharge pumping in Ne-like Ar and quasi-steady state pumping in Ne-like Zn. These XUV lasers operate in different pumping regimes and differ by the plasma parameters in the gain zone. As expected they exhibit slightly different spectral properties, thereby

demonstrating the capability of our interferometer to reach very high spectral resolution, which would not be possible with existing spectrometers.

In all cases the coherence time is of the order of 1 picosecond, corresponding to a coherence length ranging between 200μm and 1.6 mm. Such a large temporal coherence length is interesting for several applications such as interferometric lithography, or coherent diffraction imaging. For the capillary-discharge XUV laser the coherence time is much shorter than the duration of gain (several nanoseconds). Hence seeding this XUV laser with a femtosecond HHG pulse would lead to a dramatic reduction of the output pulse.

Gain narrowing was observed for two of these XUV laser systems without any rebroadening when the amplification enters the saturation regime, even for the capillary discharge XUV laser. For this Doppler-dominated XUV laser, moderate saturation rebroadening was predicted by numerical simulations. This disagreement could be because our measurement is not sufficiently accurate to detect this effect, or saturation rebroadening is canceled by homogenization of the profile by plasma effects, such as ionic correlations.

For the transient pumping Mo XUV laser we have compared the temporal coherence of the pulse generated either in the ASE mode, or in the seeded mode. We have shown that the coherence time is barely changed in the seeding mode. However based on previous studies of the pulse duration we conclude that the temporal coherence of the seeded pulse is significantly enhanced.

The duration of the Mo XUV laser, operated in the ASE mode, was investigated at LASERIX using a high-resolution X-ray Streak camera. Our study shows that the duration of the XUV laser can be varied within a limited range by varying the duration of the main pump pulse. Further experiments and simulations should be made to clarify the effect of the incidence angle (GRIP) of the main pulse.

The largest spectral bandwidth, corresponding to the shortest Fourier-transform limit duration, was measured on the QSS-pumped Ne-like Zn laser generated at PALS. Our measurement indicates for the first time that durations below 1 ps could be reached by seeding this XUV laser with a femtosecond HHG pulse. An accurate measurement of the temporal coherence requires a large number of identical laser shots, which is more difficult to achieve at PALS (Prague Asterix Laser System), due to the low repetition rate of 2 shots/hour. A better control of the spatial coherence of the XUV laser beam, on a shot-to-shot and day-to-day basis, should be implemented in a future experiment.

Although the work presented in this thesis contributes to a better knowledge of the spectral characteristics of existing collisional XUV lasers, there are still several aspects that will require further investigation. We have shown in chapter 4 that the numerical simulations account reasonably well for the measured values of spectral width, as well as for the gain narrowing behaviour. However in our method the spectral width is not measured directly, but is inferred from a Fourier-transform of the measured visibility curve. This is done by fitting the experimental data with several usual analytical functions and by selecting the one with the best fitting coefficient. Although the two QSS-pumped lasers exhibit clear Gaussian visibility curves, the fitting curves for the transient-pumped XUV laser could not be defined with a very good reliability. And they did not exhibit a Gaussian shape. This result seems in contradiction with our simulation study discussed in chapter 2, where we have shown that the profile of the amplified pulse should always be Gaussian. We suspect that this discrepancy is related to the duration of the XUV laser pulse compared to the coherence time.

We found that the capillary discharge XUV laser and the Ne like Zn laser both have a long pulse duration compared to the coherence time. In this case the interferogram is integrated over a large number of coherence times; so it is statistically stable. In contrast the transient Ni-like Mo XUV laser has a pulse duration comparable to the coherence time. So the detected signal in the interferogram is integrated only over few (less than 5) coherence times; it is not statistically stable. This could lead to a visibility that is not Gaussian because the number of data is not large enough to give a statistical measurement. The way this will affect the measurement of the spectral profile and the width should be investigated in the near future, but beyond the frame of this thesis.